Correcting Aerosol Extinction Coefficient Vertical Structure Biases in GEOS-Chem via a Physics-Informed Transformer with Physical Mechanism Diagnosis

Jiajun Xiong[1], Yi Wang[1], Jun Wang[2,3], Yanyu Wang[4], Meng Zhou[5,6], Minghui Tao[1], Wenhui Dong[1], Jhoon Kim[7], Lunche Wang[1]

[1]Hubei Key Laboratory of Regional Ecology and Environmental Change, School of Geography and Information Engineering, China University of Geosciences, Wuhan, 430074, China

[2]Department of Chemical and Biochemical Engineering, The University of Iowa, Iowa City, IA 52242, USA

[3]Center for Global and Regional Environmental Research, The University of Iowa, Iowa City, IA 52242, USA

[4]State Environmental Protection Key Laboratory of Formation and Prevention of Urban Air Pollution Complex, Shanghai Academy of Environmental Sciences, Shanghai 200233, China

[5]Goddard Earth Sciences Technology and Research, University of Maryland, Baltimore County, MA 21250, USA

[6]NASA/Goddard Space Flight Center, Global Modeling and Assimilation Office, Greenbelt, MD 20771, USA

[7]Department of Atmospheric Sciences, Yonsei University, Seoul, 03722, South Korea

Correspondence to: Yi Wang (wangyi34@cug.edu.cn)

Abstract

Accurately characterizing aerosol vertical distributions is essential for evaluating radiative forcing and air quality. While Chemical Transport Models (CTMs) simulate spatially continuous Aerosol Extinction Coefficient (AEC, km^{-1}), they exhibit systematic AEC biases. Cloud-Aerosol Lidar with Orthogonal Polarization (CALIOP) observations provide precise AEC profiles but are constrained by sparse spatial sampling. To bridge this gap, we propose a physics-informed Transformer framework as a supervised bias-correction model to correct biases in the Aerosol Extinction Coefficient (AEC, km^{-1}) profiles simulated by GEOS-Chem. Unlike standard Transformer, our framework features a dual-stream architecture with explicit physical constraints. It employs Gated Feature Fusion to integrate vertical structures (combining GEOS-Chem priors with MERRA-2 profiles) by dynamically identifying height-dependent drivers, and leverages Cross-Attention to incorporate MERRA-2 surface environmental constraints for modulating AEC vertical rectification with synoptic contexts. This approach effectively predicts systematic biases relative to CALIOP satellite observations and resolves AEC profiles, surpassing methods retrieving only aerosol layer heights. "Leave-One-Year-Out" validation over East Asia during 2017–2019 demonstrates significant AEC precision improvements, increasing R from 0.49–0.53 in the GEOS-Chem simulations to 0.66–0.73 and reducing RMSE by approximately 25%. The model effectively mitigates over-diffusion, significantly reducing AEC simulation biases in the critical near-surface layer while capturing smoothed biomass burning and dust plumes. Additionally, it exhibits robust cross-continental transferability, reproducing bias patterns over the North American domain (R=0.70) without retraining, confirming the internalization of universal physicochemical relationships linking atmospheric states to simulation biases. Furthermore, interpretability analysis serves as a diagnostic tool to guide physical model improvement

设置了格式：字体颜色：文字 1

~~model improvement~~. The model identifies temperature and sensible heat flux as primary drivers to constrain boundary layer mixing, pointing to potential uncertainties in vertical eddy diffusion. Additionally, ~~and~~ it uses environmental proxies (e.g., vegetation indices and diffuse radiation) to diagnose potential deficiencies in dust threshold friction velocity~~uplift~~ and secondary organic aerosol yields~~formation~~. These insights provide a physical basis for refining parameterization schemes in CTMs~~chemical transport models~~.

Keywords: Aerosol extinction coefficient profiles, Deep learning, Chemical transport models, CALIOP, Model interpretability

1. Introduction

Atmospheric aerosols are key modulators of the Earth's climate radiative forcing (Kahn et al., 2005; Stier et al., 2007; Dong et al., 2023; Wang et al., 2023) ~~(Hayasaka et al., 2007; Stier et al., 2007; Koren et al., 2004; Liu et al., 2011; Wang et al., 2023; Kahn et al., 2005; Dong et al., 2023)~~ and environmental health (Chen et al., 2022b; Song et al., 2025). As Aerosol Optical Depth (AOD) serves as a fundamental column-integrated parameter (Kaufman et al., 2002), it fails to reveal critical vertical distribution information (Winker et al., 2010; Lu et al., 2025b; Zhu et al., 2024). In reality, the vertical structure of aerosols—characterized by Aerosol Extinction Coefficient (AEC) profiles (Xiong et al., 2025; Jiang et al., 2024; Zhen et al., 2024) and layer heights (Wang et al., 2013; Kim et al., 2025; Yorks et al., 2023; Fan et al., 2025) ~~(Fan et al., 2025; Kim et al., 2025; Wang et al., 2013; Christian et al., 2019; Yorks et al., 2023)~~ —is the core physical quantity determining their climatic and environmental effects. Specifically, the vertical distribution governs the atmospheric radiative energy budget and thermal structure; the altitude of absorbing aerosols determines heating rate profile (Lu et al., 2020; Xu et al., 2016) and atmospheric stability (Koch and Del Genio, 2010), and failure to resolve this vertical feature leads to significant radiative forcing estimate biases (Zarzycki and Bond, 2010; Myhre et al., 2013; Shi et al., 2021; Wang et al., 2014). Second, the vertical co-existence of aerosols and clouds is a prerequisite for aerosol-cloud interactions (Zarzycki and Bond, 2010; Ge et al., 2014), meaning that relying solely on column totals hinders the accurate quantification of aerosol impacts on cloud microphysics (Lu et al., 2025b; Wilcox, 2012; Christensen et al., 2020; Zhao et al., 2019). Finally, vertical stratification bridges regional pollution with global transport: aerosols uplifted into the free troposphere undergo intercontinental transport (Val Martin et al., 2013; Weinzierl et al., 2017; Choi et al., 2024), whereas those trapped within the Planetary Boundary Layer (PBL) directly determine surface $PM_{2.5}$ concentrations (Chen et al., 2022a; Handschuh et al., 2022) and health outcomes (Diner et al., 2018). Therefore, precisely characterizing AEC profiles is not only a vital

supplement to traditional AOD analysis (Lv et al., 2016; Wei et al., 2019) but also a cornerstone for reducing climate model uncertainties and understanding transboundary pollutant transport.

Despite the recognized importance of aerosol vertical distribution, acquiring high-precision, spatiotemporally continuous, and vertically resolved three-dimensional (3D) aerosol information globally remains a formidable challenge. Current characterization methods primarily follow two pathways: passive remote sensing retrieval and active remote sensing observation. With extensive swath widths, passive satellite sensors, such as the TROPOspheric Monitoring Instrument (TROPOMI) and Himawari-8, have made strides in retrieving Aerosol Layer Height (ALH) (Lu et al., 2025a; Nanda et al., 2020). Utilizing differential absorption in oxygen bands (O_2 A/B) (Ding et al., 2016; Nanda et al., 2018; Chen et al., 2025; Sanders et al., 2015) ~~(Xu et al., 2017; Sanders et al., 2015; Nanda et al., 2018; Kim et al., 2025; Xu et al., 2024; Xu et al., 2019; Ding et al., 2016; Chen et al., 2021b; Chen et al., 2021a; Chen et al., 2025)~~ or multi-angle stereoscopic techniques (Kahn et al., 2005; Dubovik et al., 2011), these algorithms estimate the effective ALH. However, the effective ALH merely represents the optical centroid or a vertically weighted average of the aerosol column, rather than a resolved vertical profile (Chimot et al., 2018; Lu et al., 2025b). While valuable for tracking plumes (Huang et al., 2024), it fails to resolve complex multi-layer structures (Winker et al., 2013) and cannot provide the vertical gradients of AEC necessary for calculating radiative heating rates (Samset et al., 2013). In contrast, spaceborne active lidars—specifically the Cloud-Aerosol Lidar with Orthogonal Polarization (CALIOP)—offer high-resolution Aerosol Extinction Profiles (AEPs) that resolve aerosol stratification (Liu et al., 2012; Huang et al., 2013; Wang et al., 2021a) ~~(Huang et al., 2013; Liu et al., 2012; Qu et al., 2016; Ma et al., 2013; Wang et al., 2021a)~~. Nevertheless, constrained by narrow nadir-viewing geometry (Winker et al., 2009; Hunt et al., 2009) and sparse sampling, active remote sensing suffers from substantial observational gaps, producing a "curtain-like" dataset rather than planar coverage (Koffi et al., 2012b; Colarco et al.,

2014). To bridge these gaps, Chemical Transport Models (CTMs, e.g., GEOS-Chem and WRF-Chem) are indispensable for simulating continuous 3D aerosol fields (Xiong et al., 2025; Jiang et al., 2024). However, these models are often hampered by uncertainties in emission inventories (Bond et al., 2013; Hoesly et al., 2018; Liang et al., 2023) and simplified physical parameterizations (e.g., wet scavenging, boundary layer turbulent mixing) (Xiong et al., 2025; Du et al., 2020; Zeng et al., 2020), leading to systematic biases and misalignment with lidar observations (Koffi et al., 2016; Koffi et al., 2012a; Kim et al., 2015).

To bridge the gap between sparse observations and biased simulations, traditional studies have employed Data Assimilation (DA) techniques, such as 3D-Var or Kalman Filtering (Henze et al., 2009; Sekiyama et al., 2010; Wang et al., 2020b; Henze et al., 2007; Wang et al., 2020a; Zhang et al., 2011). However, operational DA schemes often face prohibitive computational costs (Benedetti et al., 2018) and rely on Gaussian error assumptions that may not match the complex, non-linear characteristics of aerosol processes (Bocquet et al., 2010; Geer, 2021). Driven by the exponential growth of atmospheric big data, Deep Learning (DL) has emerged as a transformative alternative for bias correction and multi-source data fusion (Geer, 2021; Wang et al., 2022; Xing et al., 2022; Fan et al., 2025). Early studies successfully applied Random Forests or Deep Neural Networks to improve AOD retrieval (Sanders et al., 2015) or surface $PM_{2.5}$ estimation (Hu et al., 2014; Wei et al., 2019; Li et al., 2017). More recently, Convolutional Neural Networks (CNNs) have been utilized to estimate AEPs by extracting spatial texture features from passive satellite imagery (Zhen et al., 2024). However, these methods typically simplify profile estimation into a standard regression problem (Pashayi et al., 2025; Li et al., 2020) or rely heavily on two-dimensional (2D) spatial convolutions (Daoud et al., 2021). Consequently, they often neglect the inherent sequential correlation and physical coupling of the aerosol vertical structure. In reality, the aerosol state at a specific altitude is intimately linked to layers above and below through turbulent mixing and sedimentation (Zeng et al., 2020; Xiong et al., 2025; Du

et al., 2020). Standard CNNs or pixel-wise models struggle to capture this long-range dependency along the vertical axis (Wang et al., 2021b) and often overlook the structural priors provided by CTMs (Reichstein et al., 2019; Geer, 2021). To overcome these limitations, the Transformer architecture (Vaswani et al., 2017), originally designed for sequence modeling, offers a superior solution. Its self-attention mechanism dynamically weighs information from different altitude layers, effectively capturing global vertical dependencies within the atmospheric column. This capability makes it an effective~~ideal~~ tool for fusing the physical consistency of GEOS-Chem simulations with the vertical precision of CALIOP observations to derive~~reconstruct~~ high- precision~~fidelity~~ 3D AEC fields.

To address the spatiotemporal sparsity of spaceborne lidar observations and the inherent simulation biases of CTMs, this study proposes a physics-informed Transformer DL framework aimed at correcting systematic biases to yield~~reconstructing~~ high-precision, spatially continuous 3D AEC fields. Distinct from traditional DA systems that require concurrent observational inputs to iteratively update state variables, our framework operates as a supervised bias-correction model. It captures the intrinsic state-dependent mapping between CTM structural uncertainties and diverse environmental contexts. By conditioning the correction exclusively on the CTM's a priori state and meteorological drivers, the model effectively mitigates systematic biases without relying on CALIOP data during the inference phase. Furthermore, d~~D~~istinct from data-driven retrieval methods that rely solely on passive remote sensing imagery, our approach explicitly embeds the vertical structural priors provided by GEOS-Chem simulations and meteorological constraints from Modern-Era Retrospective analysis for Research and Applications, Version 2 (MERRA-2) reanalysis data. Leveraging the self-attention mechanism unique to the Transformer architecture, the model effectively captures and corrects the complex, non-linear bias patterns between simulated results and CALIOP observational benchmarks"~~ground truth~~". Focusing on East Asia (EA) from 2017 to 2019, we systematically evaluate the

framework's performance in bias correction~~3D AEC field reconstruction~~ and spatiotemporal generalization. Crucially, to overcome the ~~"~~black-box~~"~~ limitations of DL, we integrate SHapley Additive exPlanations (SHAP) (Lundberg and Lee, 2017) with attention weight analysis to quantitatively parse the contributions of meteorological factors and aerosol variables to the bias correction process~~AEP reconstruction~~. This process not only enables an interpretable diagnosis of CTM simulation biases—identifying the dominant drivers of bias within specific altitudes or regions—but also bridges data-driven correction with the targeted refinement of GEOS-Chem's physical parameterizations~~provides a solid physical basis for refining GEOS-Chem's physical parameterization schemes and emission inventories, thereby establishing a feedback loop from "data-driven correction" to "physical mechanism improvement."~~ The remainder of this paper is organized as follows. Section 2 introduces the multi-source datasets and model configurations. Section 3 details the physics-informed Transformer architecture and evaluation strategies. Section 4 evaluates the bias correction performance against observations and elucidates the physical drivers of simulation biases through interpretability analysis. Finally, Section 5 summarizes the conclusions.

2. Data and Model Configuration

2.1 Study Region

This study focuses primarily on EA (0°-60°N, 70°-150°E, Fig. 1), a domain characterized by complex aerosol sources and intense aerosol-meteorology interactions, serving as the core region for training and evaluating the bias-correction model. Within the EA domain, six Regions of Interest (ROIs) are selected to evaluate performance across distinct aerosol regimes (Fig. 1): the anthropogenic-dominated North China Plain (NCP) and Indo-Gangetic Plain (IGP), the dust-active Taklamakan Desert, the smoke-impacted Indochina Peninsula, and the cleaner Tibetan Plateau and Western Pacific. To investigate vertical characteristics in the lower troposphere extending from

the surface to 6 km Above Ground Level (AGL), we establish three spatial diagnostics: a 38°N transect (70°-150°E) capturing the zonal source-to-sink continuum driven by the Westerlies; a 40°N transect (120°-150°E) targeting the dispersion of continental outflow over marine surfaces; and a domain-wide zonal mean profile (0°-60°N) to reveal the macroscopic latitudinal dependence of aerosol loading and layer heights. To rigorously assess the model's spatial generalization capability, we additionally define an independent validation sub-region over North America (NA, 25°-55°N, 70°-130°W).

2.2 CALIOP

The CALIOP sensor onboard the Cloud-Aerosol Lidar and Infrared Pathfinder Satellite Observations (CALIPSO) satellite serves as the observational benchmark for characterizing aerosol vertical structure and quantifying simulation biases. We utilize the Level 2 Version 4.51 Aerosol Profile product, which provides vertical profiles of AEC at 532 nm and 1064 nm. The standard Level 2 product offers a uniform horizontal resolution of 5 km and a vertical resolution of 60 m throughout the troposphere (–0.5 km to 20 km). Given that aerosol loading is predominantly confined to the PBL and lower free troposphere (Xiong et al., 2025; Jiang et al., 2024), our analysis is restricted to the altitude range of 0–6 km AGL.

To ensure data reliability, we implement a rigorous, tiered Quality Control (QC) procedure to exclude profiles contaminated by clouds or compromised by retrieval artifacts (detailed~~s~~ in Sect. S1). This stringent assessment framework substantially enhances the precision~~fidelity~~ of the CALIOP dataset for model training (Hong and Di Girolamo, 2022; Jiang et al., 2024; Xiong et al., 2025; Mehta et al., 2023; Winker et al., 2013).

To ensure physical consistency between the GEOS-Chem and CALIOP satellite observations, we employ a strict spatiotemporal collocation strategy. Spatially, the high-resolution CALIOP Level 2 profiles are mapped onto the GEOS-Chem grid. All quality-controlled CALIOP profiles falling within a specific grid cell are spatially averaged to represent the observational mean state of that grid box. Temporally, we adopt a precise

nearest-hour collocation approach. The CALIOP overpass times are mathematically rounded to the nearest UTC hour and paired strictly with the GEOS-Chem 1-hourly instantaneous outputs. Aligning the instantaneous model output with the concurrent instantaneous observation minimizes temporal representativeness errors (typically constrained within ±30 minutes) (Ichoku et al., 2002). However, we acknowledge that this approach inherently introduces spatial representativeness errors. Averaging the narrow, "curtain-like" nadir view of CALIOP to represent a bulk 2°×2.5° grid box inevitably suffers from sub-grid heterogeneity, particularly in regions with complex terrain or localized intense emissions.

In our physics-informed data-driven framework, the collocated CALIOP AEPs are treated as the observational benchmarks~~"ground truth"~~. The training target for the Transformer model is explicitly defined as the simulation bias, calculated as the deviation of the GEOS-Chem simulated AEC from the corresponding CALIOP observations (detailed~~s~~ in ~~Section~~ Sect. 3.1). However, it is essential to acknowledge the intrinsic uncertainties associated with satellite retrievals. Validations against ground-based AERONET measurements indicate a mean relative bias in CALIOP AOD of approximately -5.1%~~–~~±~~–~~8.5% (Kim et al., 2018). Furthermore, the agreement between CALIOP 532 nm calibrated attenuated backscatter and airborne High Spectral Resolution Lidar (HSRL) measurements is typically within 1.0%~~–~~±~~–~~3.5% (Getzewich et al., 2018). These inherent observational uncertainties coupled with the spatial representativeness errors impose a theoretical upper limit on the precision of the bias correction method proposed herein.

2.3 AERONET

To independently evaluate the model's capability in capturing high-frequency temporal variations—bridging the observational gaps inherent to the sparse sampling of polar-orbiting satellites—we utilize AOD data from the AERONET (Holben et al., 1998). Specifically, the Version 3 Level 2.0 (cloud-screened and quality-assured) AOD data are employed (Giles et al., 2019). Since AERONET instruments do not directly

measure AOD at 532 nm, data are interpolated to this wavelength using the Ångström exponent derived from adjacent channels (details in Sect. S2). Two representative sites are selected for detailed case studies, targeting distinct aerosol regimes during high-loading episodes (Fig. 1): (1) Kanpur (26.5°N, 80.2°E): Located in the IGP, this site is characterized by a complex mixture of anthropogenic pollution and transported dust. We focus on a 7-day window centered on 30 April 2019, representing a typical pre-monsoon scenario driven by regional dust and haze activity (Misra et al., 2014; Singh et al., 2004; Chinnam et al., 2006); (2) Nong Khai (17.9°N, 102.7°E): Situated in the Indochina Peninsula, this site is dominated by carbonaceous aerosols resulting from intense agricultural biomass burning (Munroe et al., 2008; Nguyen et al., 2021). The analysis window is centered on 22 February 2019, coinciding with the peak of the regional active fire season (Tsay et al., 2013). Examining these high-loading cases allows us to assess the robustness of the model in reproducing the dynamic evolution of pollution accumulation and dissipation, providing a rigorous test of the temporal consistency of our bias correction approach.

2.4 GEOS-Chem and Meteorological Reanalysis

We employ the GEOS-Chem (Bey et al., 2001) global CTM (version 13.4.0) to simulate the 3D distribution of atmospheric composition, focusing on the EA domain defined in Section 2.1. The simulation spans from 1 January 2017 to 31 December 2019. The model is driven by the MERRA-2 assimilated meteorological fields provided by the NASA Global Modeling and Assimilation Office (GMAO) (Gelaro et al., 2017). To accommodate the spatially sparse sampling inherent to CALIOP's nadir-viewing geometry, the simulation is configured at a horizontal resolution of 2° × 2.5° (latitude × longitude) with 47 vertical hybrid sigma-pressure levels extending from the surface to 0.01 hPa. Anthropogenic emissions are prescribed by the Community Emissions Data System (CEDSv2) (Mcduffie et al., 2020). Biogenic emissions of Volatile Organic Compounds (BVOCs) are prescribed using the offline MEGAN inventory (Guenther et al., 2012). Biomass burning emissions are derived from the Global Fire Emissions

Database version 4 (GFED4) (Giglio et al., 2013). GEOS-Chem is operated in the "Standard Full Chemistry" mode, utilizing a fully coupled NO_x-O_x-hydrocarbon-aerosol mechanism. The aerosol simulation encompasses sulfate, nitrate, ammonium, carbonaceous aerosols, mineral dust, and sea salt. Both dry and wet deposition processes are explicitly treated to characterize aerosol sinks. Vertical transport is parameterized using a non-local PBL mixing scheme, which accounts for deep convective updrafts and turbulent diffusion (Lin and Mcelroy, 2010). To facilitate direct comparison with CALIOP observations, the model is configured to diagnose and archive 3D AEC directly at 532 nm with a 1-hour temporal resolution.

MERRA-2 reanalysis data serve a dual purpose in this study: acting as the driving meteorological field for the GEOS-Chem and constituting the key physical input features for the physics-informed Transformer model. Integrating these meteorological state variables into the DL framework aims to explicitly capture the non-linear dependence of simulation biases on synoptic and micro-meteorological conditions. Generated by the GEOS-5 atmospheric general circulation model combined with 3D variational DA, MERRA-2 provides globally consistent physical fields. To maintain consistency within our "physics-informed data-driven" framework, we extract meteorological variables that are strictly consistent with those driving GEOS-Chem. These variables are regridded to the 2° × 2.5° resolution to achieve strict spatial alignment with the aerosol simulation outputs, jointly constructing the "meteorological background" vector in the neural network's input layer.

3. Method

3.1 Input Feature Construction and Target Definition

We design a dual-stream input architecture to decouple local vertical atmospheric states from synoptic meteorological forcing. The detailed inventory of all input variables is provided in Section S3 in the supplement~~To physically decouple the local vertical structure that determines the instantaneous AEC magnitude from the~~

~~macroscopic meteorological background that controls pollutant accumulation and transport, we construct a comprehensive input feature space utilizing a dual-stream architecture: the Vertical Profile Stream and the Global Context Stream. A detailed inventory of all input variables, including physical descriptions, units, and data sources, is provided in Sect. S3~~.

The Vertical Profile Stream (VPS) resolves the atmospheric column through three sub-components~~The Vertical Profile Stream encapsulates the explicit vertical structure of the atmosphere. We integrate three sub-components to provide the necessary physicochemical and spatiotemporal context for each layer~~. (1) Physicochemical ~~State p~~Profiles: This includes GEOS-Chem simulated aerosol species and MERRA-2 meteorological profiles~~Core inputs include GEOS-Chem simulated aerosol component concentrations and MERRA-2 meteorological profiles~~. Beyond basic mass concentrations, we explicitly incorporate precursor gases~~introduce microphysical and precursor variables—such as hygroscopic growth factors, aerosol effective radii, and precursor gas concentrations~~ (SO_2, NO_x, NH_3) and microphysical variables (e.g., hygroscopic growth factors and effective radii) to physically constrain secondary aerosol formation and optical extinction~~—to physically constrain chemical transformations and optical extinction processes~~. (2) ~~V~~Height information ~~ertical Coordinate Encoding~~: To maintain vertical stratification within the attention mechanism, we embed explicit altitude information. This allows the model to correctly differentiate near-surface emission interactions from free-tropospheric long-range transport~~Since the self-attention mechanism is permutation-invariant (i.e., it treats the input sequence as a bag of vectors without inherent order), explicit height information is essential for resolving atmospheric stratification. Without this embedding, the model cannot distinguish between surface emissions and high-altitude transport layers, potentially confusing the distinct physical processes governing aerosols at different levels. We embed vertical coordinates into high-dimensional vectors and add them to the feature sequence, enabling the model to distinguish between surface interactions~~

~~and upper-level transport~~. (3) Spatiotemporal indices~~Spatiotemporal Embeddings~~: Geographical coordinates~~Although geographical~~ (latitude, longitude) and temporal indices (month, day, night) are projected into high-dimensional vectors to capture regional emission patterns and seasonal cycles~~scalars, they are critical for characterizing regional emission patterns and seasonal cycles. We project these scalars into high-dimensional vectors matching the vertical dimensions of the profile data, ensuring the model captures location-dependent and time-varying bias patterns~~.

The Synoptic Forcing Stream (SFS) incorporates 2D surface diagnostics to represent synoptic constraints on the atmospheric column. Variables such as Planetary Boundary Layer Height (PBLH) and friction velocity act as indicators for turbulent mixing. Surface fluxes and Leaf Area Index (LAI) parameterize deposition and biogenic emissions, while precipitation rates serve as proxies for wet scavenging. ~~The Global Context Stream incorporates 2D surface diagnostic variables to capture synoptic-scale constraints affecting the atmospheric column. We select the Planetary Boundary Layer Height (PBLH), surface pressure, and friction velocity to constrain vertical mixing and turbulence intensity. Surface fluxes (latent/sensible heat), soil moisture, and Leaf Area Index (LAI) are included to parameterize dry deposition velocities and biogenic emissions. Additionally, total precipitation and evaporation rates serve as proxies for wet scavenging efficiency. These variables aid the model in distinguishing between local pollution accumulation and large-scale ventilation conditions.~~

Furthermore, although our architecture does not employ explicit historical time-series modeling, it robustly captures diurnal variability. By rigorously matching the instantaneous MERRA-2 fields with the exact CALIOP overpass time, the model is directly conditioned on the concurrent thermodynamic and dynamic states. Combined with explicit day/night flags, this allows the framework to dynamically resolve meteorology-driven diurnal processes (e.g., boundary layer evolution and photochemistry) without relying on lagged predictors.

Finally, w~~W~~e define the learning target Δ_{AEC}^{target} as the systematic bias of GEOS-Chem simulated AEC (AEC_{GC}) evaluated against CALIOP observation (AEC_{CAL}):

$$\Delta_{AEC}^{target} = AEC_{GC} - AEC_{CAL} \quad (1)$$

Predicting the simulation bias~~By modeling the bias~~ Δ_{AEC}^{target}, rather than the absolute AEC magnitude, ensures the framework preserves the fundamental physical transport patterns resolved by the CTM, focusing solely on correcting systematic deviations caused by parameterization or emission uncertainties~~the framework preserves the physical patterns captured by the CTM while specifically correcting systematic biases arising from input uncertainties and simplified parameterizations~~. It is important to emphasize that while CALIOP observations provide the target during training, they are strictly excluded from the input feature space during inference. Consequently, the framework's corrective capacity is inherently bounded by the information content of the GEOS-Chem and MERRA-2 predictors. The model is designed to rectify state-dependent systematic biases rather than to artificially generate aerosol signals from completely unrepresented physical processes that lack corresponding perturbation signatures in the input fields.

It should be noted that using CALIOP retrievals as the baseline inherently propagates its systematic uncertainties (e.g., a mean relative bias of -5.1%, as discussed in Sect. 2.2) into the learning target. If CALIOP exhibits a systematic negative bias, the model may theoretically learn a tendency to slightly over-compensate the AEC. However, because GEOS-Chem's structural biases are typically an order of magnitude larger than these observational uncertainties, the data-driven correction remains highly beneficial. A detailed quantitative evaluation of the model's sensitivity to these observational uncertainties is presented in Section 4.1.5.

带格式的：缩进：首行缩进： 2 字符

3.2 Physically-Informed Transformer Architecture

~~The overall architecture of the proposed framework is illustrated in Figure 2. To effectively bridge the gap between GEOS-Chem simulations and CALIOP satellite~~

~~observations, the model is structured into five physically distinct modules: a dual-stream input layer for decoupling the Vertical Profile and Global Context Stream, a Feature Embedding layer equipped with a Gated Feature Fusion mechanism, Transformer encoder stack for capturing vertical dependencies, a Cross-Attention module for incorporating synoptic constraints and a residual output generation layer. Rather than treating all inputs uniformly, the model processes the two input streams using embedding strategies specifically tailored to their physical nature (as detailed in Sect. S4a, b), ensuring that the distinct structural characteristics of atmospheric vertical profiles and global environmental contexts are preserved in the high-dimensional feature representation.~~The overall architecture of our proposed framework (Figure 2) bridges GEOS-Chem simulations and CALIOP observations. To preserve the distinct structural characteristics of atmospheric profiles and synoptic environmental contexts, the framework processes these two streams through specialized embedding strategies (detailed in Sect. S4a, b). The model comprises an altitude-dependent gated feature fusion mechanism, a Transformer encoder for vertical dependencies, a cross-attention module for synoptic constraints, and an output layer.

3.2.1 Altitude-Dependent Gated Feature Fusion~~Dynamic Embedding and Gated Feature Fusion~~

Physical factors governing AEC vary significantly with altitude. Local emissions and chemical composition dominate near-surface AEC~~To explicitly capture the height-dependent variations in dominant physical drivers, we design a Gated Feature Fusion mechanism within the Vertical Profile Stream. This design is motivated by the physical consensus that the factors governing AEC vary significantly with altitude: near-surface AEC is predominantly driven by local emissions and chemical composition~~ (Xiong et al., 2025; Jiang et al., 2024), whereas long-range transport and regional backgrounds dictate the free troposphere~~whereas AEC in the free troposphere is often dictated by long-range transport pathways and regional background levels~~ (Uno et al., 2009; Val Martin et al., 2013). To reflect this stratification, we design a gated feature fusion

mechanism within the VPS. Instead of statically concatenating inputs, this module dynamically weights the contributions of physicochemical profiles, height information, and spatiotemporal indices for each altitude layer. This allows the model to autonomously prioritize the most relevant physical drivers at specific heights.

The SFS incorporates diverse meteorological parameters with distinct physical units. To prevent the network from treating these distinct physical quantities merely as dimensionless numbers, we implement a variable identity embedding (Eq. S4). This mechanism assigns a unique physical tag to each 2D variable, ensuring the model accurately distinguishes between different meteorological forcing factors when modulating the AEC simulation bias.

~~Instead of using a static concatenation which assumes fixed importance across the entire column, this mechanism dynamically weighs the contributions of four feature components: physicochemical profiles, vertical height information, spatial coordinates, and temporal indices. For each vertical layer z, the unified local embedding $E_{local}^{(z)}$ is computed as an adaptive weighted sum:~~

~~$$E_{local}^{(z)} = \sum_{k=1}^{4} \alpha_k^{(z)} \cdot Norm\left(h_k^{(z)}\right) \quad s.t. \quad \sum \alpha_k = 1 \qquad (2)$$~~

~~where $h_k^{(z)}$ represents the embedding of the k-th feature group. The attention weights $\alpha_k^{(z)}$ are generated by a learnable gating network, allowing the model to autonomously identify and prioritize the most physically relevant information source for each specific altitude layer.~~

~~For the Global Context Stream, we address the challenge of integrating diverse environmental variables that possess distinct physical natures. Since different physical variables may share similar numerical ranges but possess distinct physical meanings, simple numerical projection inevitably leads to semantic ambiguity. We implement a Variable Identity Embedding strategy (Eq. S4) to encode the unique "physical identity" of each variable into the latent space. This ensures that the model explicitly~~

~~distinguishes between different physical variables, preserving their distinct physical semantics during the cross-modal interaction.~~

3.2.2 Modeling Vertical Connectivity and Synoptic Modulation~~Transformer Encoder and Cross-Modal Interaction~~

Aerosol layers are inherently coupled through vertical exchange processes such as turbulent mixing, deep convection, and gravitational sedimentation. We employ a Transformer encoder stack to explicitly model this vertical connectivity. Its self-attention mechanism acts as a dynamic vertical covariance operator~~Following Gated Feature Fusion, the Vertical Profile Stream is processed by a Transformer Encoder stack to explicitly model the vertical connectivity of the atmosphere. Physically, aerosol layers are not isolated but are inherently coupled through vertical exchange processes such as turbulent mixing, deep convection, and gravitational sedimentation. Unlike CNNs which primarily focus on local spatial neighborhoods, the Multi-Head Self-Attention~~ (~~MSA,~~ detailed in Sect. S4c). It facilitates information flow between near-surface accumulation layers and high-altitude transport layers, ensuring the rectified AEC profile maintains physical continuity~~mechanism enables the model to capture global vertical dependencies. This facilitates the necessary information flow between near-surface accumulation layers and high-altitude transport layers, ensuring that the reconstructed profile maintains physical continuity along the vertical axis~~.

To constrain this vertical AEC bias correction with synoptic meteorology, we introduce a cross-attention layer. Functionally, this mechanism acts as a dynamic diagnostic process. It allows the aerosol state at each specific altitude to dynamically respond to the prevailing synoptic conditions (e.g., surface wind speed, PBLH), thereby extracting relevant environmental constraints for the local bias adjustment. This design mimics physical reality, where synoptic meteorological backgrounds continuously modulate local microphysical structures~~To physically constrain the vertical reconstruction using synoptic-scale conditions, we introduce a Cross-Attention module. In this configuration, the encoded vertical profiles serve as Queries (Q), while the~~

~~Global Context Stream embeddings act as both Keys (K) and Values (V). This mechanism enables the aerosol state at a specific layer (Q) actively scans the prevailing synoptic conditions (K)—such as surface wind speed or humidity—to retrieve the relevant environmental constraints (V) needed to correct its bias. This design effectively mimics the physical reality where local microphysical structures are conditioned by the macro-scale meteorological background, ensuring that the corrected AEC profiles are dynamically consistent with the large-scale weather patterns~~.

3.2.3 ~~Residual Output Generation~~Output Layer ~~with Long Skip Connection~~

To predict the final AEC bias, we employ a residual connection that adds the initial baseline state (from the VPS) directly to the output of the cross-attention module (which has already fused the encoded VPS with the SFS). Physically, this residual design serves as a critical prior constraint. It anchors the network to the fundamental atmospheric state provided by GEOS-Chem, ensuring the model computes a meteorology-driven perturbation rather than generating unphysical aerosol signals. Subsequently, the integrated features undergo a progressive dimension-reduction (represented as $D \rightarrow D/2 \rightarrow D/4$ in Fig. 2). This architecture functions as an information funnel, filtering redundant meteorological noise and distilling the non-linear interactions among diverse drivers to accurately quantify the true magnitude of the AEC biases. ~~To generate the final bias prediction, we introduce a Long Skip Connection, adding the initial projected physicochemical features ($H_{physchem}$) directly to the output of the Cross-Attention module (H_{cross}) before the final projection:~~

~~$$\Delta_{AEC}^{pred} = MLP\left(H_{cross} + H_{physchem}\right) \cdot s + b \quad (3)$$~~

~~Where Δ_{AEC}^{pred} denotes the predicted systematic bias of the AEC. The parameters s and b are learnable scaling and bias terms, respectively, introduced to adaptively map the normalized network outputs to the physical magnitude of extinction biases. This design explicitly preserves physicochemical state information, allowing the regressor to access the baseline atmospheric state while utilizing context-aware features (e.g., thermodynamic stability, turbulent mixing intensity, and surface emission~~

带格式的：缩进：首行缩进： 2 字符

~~conditions) to disentangle complex bias sources.~~

3.3 Magnitude-Weighted Loss Function ~~with False Alarm Penalty~~

To address the statistical imbalance between the predominant clean background signals and the physically critical pollution episodes, we propose a Magnitude-Weighted Loss (L_{MW}, detailed in Sect. S4g). This customized loss function dynamically rescales the correction weighting to enhance the model's sensitivity to large simulation AEC biases while strictly suppressing spurious aerosol artifacts in atmospheric regimes where the CTM already performs satisfactorily.

~~The distribution of simulation biases exhibits significant heterogeneity. Standard Mean Squared Error (MSE) loss is often dominated by the numerous samples with small biases, causing the model to under-correct large systematic biases. To address this, we propose a Magnitude-Weighted Loss (L_{MW}):~~

带格式的：缩进：首行缩进： 0 字符

~~$$L_{MW} = \frac{1}{N}\sum_{i=1}^{N}\left(\Delta_{AEC}^{pred} - \Delta_{AEC}^{target}\right)^2 \cdot \omega\left(\Delta_{AEC}^{target}\right) \quad (4)$$~~

~~$$\omega\left(\Delta_{AEC}^{target}\right) = \left|\Delta_{AEC}^{target}\right|^p + \lambda \cdot e^{-\beta\left|\Delta_{AEC}^{target}\right|} + \epsilon \quad (5)$$~~

~~where Δ_{AEC}^{target} is the target bias and Δ_{AEC}^{pred} is the predicted bias. The weight function $\omega\left(\Delta_{AEC}^{target}\right)$ incorporates three hyperparameters determined through empirical validation: (1) Large-Error Prioritization ($\left|\Delta_{AEC}^{target}\right|^p$): This term ($p$ is a constant term.) amplifies the penalty for samples with large simulation biases, forcing the model to focus on instances where GEOS-Chem fails significantly. (2) False Alarm Penalty ($\lambda \cdot e^{-\beta\left|\Delta_{AEC}^{target}\right|}$): This term imposes a penalty when the target bias is near zero but the model predicts a non-zero correction, effectively suppressing "false alarms" in layers where the CTM performance is already satisfactory. Both λ and β are constant terms. (3) Base Stability Term (ϵ): A small constant ensures numerical stability.~~

3.4 Model Evaluation Strategy

To comprehensively assess the robustness and generalization capability of the physics-informed Transformer model, we design a rigorous evaluation framework

covering fivcour dimensions.

(1) Spatial bBlock cCross-vValidation: To mitigate information leakage caused by spatial autocorrelation (Geer, 2021) , we implement a spatial block K-fold cross-validation strategy (Sect. S5). The study region is divided into non-overlapping 4° × 5° blocks (aggregating 2-×-2 model grids). In each iteration, the model is trained on four folds and evaluated on the remaining spatially independent fold. This "checkerboard" approach ensures performance metrics reflect the model's ability to extrapolate to unseen geographic locations.

(2) Temporal tTransferability: Given the interannual variability in emissions and meteorology (Xiong et al., 2025), we adopt a "Leave-One-Year-Out (LOYO)" cross-validation scheme comprising three independent experiments (Table 1). This tests whether the model learns generalizable physical rules rather than overfitting to specific temporal patterns.

(3) External sSpatial gGeneralization: To rigorously ~~stress~~ test the model's transferability beyond its training distribution, we perform an out-of-domain evaluation on the independent NA ~~sub-region~~ defined in Section 2.1. By directly applying the model trained on EA data to this unseen continent—which possesses distinct aerosol sources and meteorological backgrounds—we evaluate whether the learned bias-correction mechanism captures universal physical laws rather than region-specific correlations. Furthermore, to dissect the impact of varying aerosol composition regimes on model transferability, the NA validation results are further stratified using CALIOP aerosol subtype classifications.

(4) Independent gGround-based vValidation: We employ ground-based AERONET observations as an independent physical benchmark. Predicted AEPs are vertically integrated to derive column AODs, which are then compared with AERONET data to assess the reproduction of high-frequency temporal evolution.

(5) Methodological benchmarking: We evaluate the proposed Transformer against conventional machine learning baselines and conduct ablation studies to justify the

architectural complexity and isolate the sources of performance improvements.

To quantify the model performance across these dimensions, we employ a comprehensive set of statistical metrics including the Pearson correlation coefficient (R), Mean Absolute Error (MAE), Root Mean Square Error (RMSE), and Normalized Root Mean Square Error (NRMSE). Detailed mathematical definitions are provided in Sect. S6. NRMSE is specifically used to enable fair comparisons across vertical layers by normalizing biases against the exponentially decaying dynamic range of AEC.

3.5 Model Interpretability Framework

To elucidate the inference logic of the correction framework and ensure physical consistency, we establish a hierarchical diagnostic approach~~To elucidate the inference logic of the DL model and ensure physical consistency, we establish a comprehensive interpretability framework examining internal mechanisms and feature sensitivities to identify the physical drivers governing the bias correction~~. This framework addresses potential functional overlaps by characterizing model behavior across three scales: micro-scale local sensitivity, domain-wide feature ranking, and regional heterogeneity.

3.5.1 Micro-Scale Local Sensitivity ~~Dual-Mechanism Attribution~~

We employ distinct attribution methods tailored to~~for~~ the hybrid inputs to capture micro-scale responses. ~~First, F~~For the ~~Vertical Profile Stream~~VPS, we apply g~~G~~radient-based a~~A~~ttribution ~~(detailed in Sect. S7a)~~, utilizing the I~~I~~nput ~~×~~ ~~Gradient~~Gradient method (Shrikumar et al., 2017) to quantify the sensitivity of AEC bias correction to physicochemical profiles~~local variations in vertical structures~~. Simultaneously, Cross-Attention weights are extracted to map the interaction strength between the SFS and the VPS, revealing how synoptic forcing modulates vertical profile rectifications. Furthermore, to understand the model's internal decision-making, we analyze the learnable weights of the gated feature fusion mechanism (detailed in Sect. 3.2.1). This analysis visualizes the altitude-dependent prioritization among the four VPS components: physicochemical profiles, height information, spatial coordinates, and temporal indices. ~~This identifies which specific altitude layers and species dominate the~~

~~AEC simulation bias. Second, we conduct Attention-based Analysis (detailed in Sect. S7b) by extracting Cross-Attention weights to map the interaction strength between the Global Context Stream and the Vertical Profile Stream at specific vertical layers, revealing how macroscopic meteorology modulates vertical reconstruction biases.~~

3.5.2 Domain-wide Feature Ranking

To assess the model's reliance on the overarching input feature groups (the VPS and SFS), we perform permutation feature importance analysis (detailed in Sect. S7d). By measuring the percentage increase in Mean Squared Error (MSE) when specific groups are randomly shuffled, this method provides a domain-wide to identify the fundamental predictors essential for AEC bias correction.

~~**3.5.2 Gated Information Fusion Analysis**~~

~~We analyze the scalar weights learned by the gated fusion mechanism to understand information prioritization (detailed in Sect. S7c): ① Vertical Dependency visualizes how reliance on different information sources varies with altitude. ② Overall Contribution quantifies the holistic importance of each feature group (Profile, Global, Spatiotemporal, Height) to the final reconstruction.~~

3.5.3 Regional Heterogeneity ~~Feature Sensitivity and Regional Drivers~~

Considering the spatial heterogeneity of aerosol sources, ~~We assess robustness and diagnose drivers using two perturbation-based methods. ① Permutation Feature Importance: Measures global sensitivity by randomly shuffling feature groups. Importance is defined as the percentage increase in MSE relative to the baseline, identifying fundamental predictors for domain-wide AEC bias correction (detailed in Sect. S7d). ②~~ SHAP Analysis~~: SHAP~~ is used to dissect regional dependencies and feature interactions~~heterogeneity~~. We employ a K-means clustering strategy to construct a representative background dataset capturing diverse atmospheric states (detailed in Sect. S8). SHAP values are computed for the designated ROIs to reveal how dominant AEC bias drivers shift under different environmental regimes~~SHAP values are computed for specific regions to reveal how dominant AEC bias drivers shift~~

~~under different environmental regimes~~.

~~**3.5.2 Gated Information Fusion Analysis**~~

~~We analyze the scalar weights learned by the gated fusion mechanism to understand information prioritization (detailed in Sect. S7e): ① Vertical Dependency visualizes how reliance on different information sources varies with altitude. ② Overall Contribution quantifies the holistic importance of each feature group (Profile, Global, Spatiotemporal, Height) to the final reconstruction.~~

4. Results and Discussion

4.1 Evaluation of the Transformer Model

4.1.1 Overall Predictive Performance and Temporal Generalization

To quantitatively assess the model's robustness in capturing the non-linear mapping between GEOS-Chem simulation biases and atmospheric states, we execute a "LOYO~~Leave-One-Year-Out~~" cross-validation strategy comprising three independent experiments (Table 1). The Transformer achieves a high average R of 0.659 and a low MAE of 0.014 km^{-1} on the independent test years (Table 2). These metrics demonstrate robust predictive skill, confirming that the model has successfully learned to reproduce the systematic component of extinction biases from the input state variables. Notably, a comparison with the internal validation results (Table S2) reveals that the model's performance on the unseen test sets is comparable to—and in some metrics marginally superior to—that on the validation sets. This consistency suggests that the Transformer architecture has extracted time-invariant, physically meaningful representations of aerosol bias mechanisms rather than overfitting to specific temporal anomalies in the training data. The ability to generalize to years with distinct meteorological interactions underscores the model's potential for operational bias correction.

4.1.2 Seasonal Stability and Robustness

We further examine the temporal stability of the model by analyzing monthly variations in the predictive accuracy of the AEC simulation bias (Fig. 3). The model

exhibits a distinct seasonal pattern characterized by superior performance in winter and a moderate decline in summer. During the winter months (December–February), R consistently peaks above 0.7. This enhanced performance is attributed to the synergistic effect of favorable meteorology and observational quality. Specifically, the lower solar elevation angle in winter minimizes solar background noise, thereby enhancing the Signal-to-Noise Ratio (SNR) of the CALIOP retrievals compared to the strong background illumination present in summer (Zhen et al., 2024). Additionally, the stable boundary layer in winter confines aerosols to lower altitudes (Xiong et al., 2025), creating sharper vertical gradients that are physically more distinct for the network to capture. In contrast, a discernible decline in performance occurs during the summer (June–August) over EA. This reduction implies a compound mechanism driven by both data scarcity and observational uncertainty. First, the decline coincides with a sharp decrease in the effective sample size (Fig. 3a, gray bars). This is mechanically linked to the Asian Summer Monsoon, where frequent cloud cover necessitates the exclusion of a significant volume of cloud-contaminated CALIOP profiles (Winker et al., 2009; Winker et al., 2013; Vernier et al., 2011), thereby reducing the representativeness of training data for complex convective scenarios. Second, and more critically, the inherently lower SNR in summer observations imposes a theoretical ceiling on point-to-point correlation metrics. Since random noise in the validation target (CALIOP) cannot be physically predicted, it naturally degrades the R, even if the model correctly retrieves the underlying aerosol signal.

Crucially, despite the fluctuations in linear correlation driven by these external sampling and observational constraints, the model demonstrates remarkable stability in correcting systematic biases. Figure 3c illustrates that the monthly mean bias remains tightly constrained within ± 0.01 km^{-1} throughout the year, exhibiting negligible seasonal drift even during the challenging summer months. This decoupling of metrics implies that while random noise (reflected in lower R) increases in summer due to complex meteorology and reduced SNR, the model does not introduce systematic

artifacts. This conclusion is further supported by internal validation results (Fig. S2), which confirms that performance fluctuations are a response to data quality rather than intrinsic model instability. Moreover, detailed monthly density scatter plots (Figs. S3–S5) visually corroborate this robustness, revealing that the majority of predictions remain tightly clustered around the 1:1 identity line, independent of the season.

4.1.3 Vertical Profile Precision~~Fidelity~~ and Height-Dependent Performance

Given the critical importance of vertical stratification in radiative forcing calculations, we further scrutinize the model's performance as a function of altitude. A distinct advantage of this study, unlike traditional bias correction methods limited to column-integrated parameters, lies in its capability to finely resolve vertical aerosol structures. As evidenced by the vertical profiles of evaluation metrics (Fig. 4a), the model achieves peak performance within the bulk of the PBL (0.5–1.5 km), where R consistently exceeds 0.7. This altitude range corresponds to the region with the heaviest aerosol loading and the most complex chemical composition (Xiong et al., 2025; Jiang et al., 2024). This superior skill suggests that the Transformer's self-attention mechanism effectively captures the steep vertical gradients and pollutant accumulation patterns driven by boundary layer dynamics. Furthermore, the NRMSE (Fig. 4b) remains suppressed below 5% throughout the entire 0–6 km column. This low error magnitude indicates that the model maintains consistent relative predictive accuracy even in the cleaner free troposphere, avoiding the generation of spurious artifacts often seen in DL applications on sparse data. Finally, the vertical profile of mean bias (Fig. 4c) fluctuates narrowly around zero at all altitude levels. This confirms the model's low systematic bias in the vertical dimension, ensuring that the correction process mitigates existing simulation errors without introducing new artificial biases.

4.1.4 Spatial Generalization and Bias Reproduction

Beyond capturing vertical structures, the capacity to resolve the spatial heterogeneity of systematic biases is vital for correcting 3D aerosol fields. In the primary study domain (EA), the Transformer demonstrates high precision~~fidelity~~ in

reproducing the complex spatial bias modes of the original GEOS-Chem simulation (Fig. 5, columns 1–3). Specifically, the model accurately captures the systematic underestimation over major anthropogenic and biomass burning source regions, including the NCP, IGP, and Indochina Peninsula. Over regions like the IGP, this negative simulation bias is primarily driven by the underrepresentation of local biofuel and agricultural emissions in traditional inventories (Mcduffie et al., 2020), coupled with simplified aerosol mixing state assumptions that underestimate extinction enhancement under high humidity (Burgos et al., 2020; Zhai et al., 2021). Furthermore, the model's excessive numerical diffusion, a common limitation in CTMs, artificially dilutes the strong near-surface pollutant accumulation bounded by local topography (e.g., the Himalayas) (Eastham and Jacob, 2017). The GC-TF framework effectively identifies and mitigates these state-dependent underestimations. Additionally, it rectifies the biases over natural dust sources like the Taklamakan Desert. ~~— including the NCP, IGP, and Indochina Peninsula—as well as over natural dust sources like Taklamakan Desert.~~ Conversely, it correctly identifies regions of systematic overestimation, predominantly located over the remote Western Pacific Ocean, the high-altitude Tibetan Plateau, and high-latitude terrestrial regions (e.g., Siberia). These capabilities suggest that the model effectively differentiates between bias regimes associated with distinct environments: it mitigates the systematic overestimation in clean background regions while concurrently compensating for the underestimation of source intensities in high-loading regions.

However, a localized area of strong positive AEC simulation bias (GEOS-Chem overestimation) appears in Central China in the 2019 target map (Fig. 5c), which is not fully reproduced by the prediction (Fig. 5g). We attribute this discrepancy primarily to observational sparsity and the episodic nature of the bias. Specifically, this region corresponds to a significantly lower density of valid CALIOP samples compared to the surrounding domain (Fig. S6), likely resulting from retrieval limitations associated with complex terrain and frequent cloud cover. Furthermore, monthly decomposition reveals

that this elevated annual mean AEC simulation bias is predominantly driven by extreme values in January (Fig. S7), representing a transient winter episode specific to the 2019 test year. In such data-sparse regimes, the physics-informed Transformer model yields conservative predictions, suggesting that it prioritizes learning generalized physical laws over overfitting to localized outliers or specific interannual anomalies under-represented in the training distribution.

Crucially, the fourth column of Figure 5 (2018 NA) presents a rigorous "out-of-domain" generalization test, where the model trained exclusively on EA data is directly applied to NA. Despite distinct differences in emission inventories and meteorological backgrounds between the two continents, the model exhibits remarkable spatial transferability. It successfully predicts the systematic underestimation over the Eastern United States and the overestimation over coastal areas (e.g., the Gulf of Mexico and the Atlantic coast), mirroring the actual GEOS-Chem AEC bias patterns (Target). This successful spatial extrapolation strongly suggests that the physics-informed Transformer model has learned the universal physical mapping between comprehensive atmospheric state variables (detailed in Table S1) and CTM simulation biases, rather than merely overfitting to the geographical coordinates or specific emission patterns of the EA training domain.

4.1.5 Sensitivity to Observational Uncertainties

As discussed in Section 3.1, using satellite retrievals as the learning target inherently absorbs CALIOP's systematic uncertainties. To quantify how this observational limitation impacts the reliability of our framework, we conduct a perturbation-based sensitivity analysis (detailed in Sect. S13). We retrain the GC-TF model by artificially injecting a ±5% systematic perturbation into the CALIOP AEC learning target.

Table S3 and Figure S17 demonstrate that this systematic perturbation induces only a narrow envelope of variation in the corrected AEC profiles. The absolute shift in the Mean Bias fluctuates tightly between 0.001 and 0.004 km^{-1}, and the perturbed

设置了格式：上标

predictive RMSE (0.040 km^{-1}) consistently outperforms the original GEOS-Chem simulation (0.052 km^{-1}) by a large margin. This confirms that while observational uncertainties theoretically bound the absolute precision, the physics-informed Transformer does not uncontrollably amplify these errors, ensuring the robustness of the data-driven correction.

4.1.6 Methodological Benchmarking and Structural Necessity

To justify the architectural complexity and isolate the sources of performance gains, we conduct comprehensive benchmarking and ablation studies using the independent 2017 test dataset (Table S5). When trained with identical GEOS-Chem and MERRA-2 predictors, the proposed Transformer significantly outperforms conventional machine learning baselines. A standard Multilayer Perceptron (MLP) and a 1-Dimensional Convolutional Neural Network (1D-CNN) yielded substantially lower R (R=0.083 and 0.540, respectively) compared to the Transformer (R=0.666). This performance gap confirms that global sequence modeling via self-attention is critical for capturing the long-range vertical coupling of atmospheric aerosols—such as boundary layer-to-free troposphere exchange—which localized convolutions or point-wise networks fail to resolve.

Furthermore, ablation experiments confirm that the performance enhancements are intrinsically linked to our structural designs. Removing the Gated Feature Fusion or the Cross-Attention module noticeably degrades predictive accuracy (Table S5). More importantly, beyond statistical improvements, these modules are physically indispensable. They transition the framework from a black-box predictor into a diagnostic tool, providing the explicit attention weights necessary to quantify height-dependent physical drivers (Sect. 4.5.1) and surface environmental modulations (Sect. 4.5.3).

4.2 Evaluation of Corrected GEOS-Chem Simulations

4.2.1 Correction of Systematic Biases in AEC Magnitude

To quantify the efficacy of the GEOS-Chem corrected by Transformer (GC-TF)

model in correcting the magnitude of the AEC, we first compare the overall statistical relationship between simulated values and CALIOP observations across three independent test years from 2017 to 2019 (Fig. 6). The original GEOS-Chem simulation AEC exhibits a dispersed distribution around the 1:1 identity line, with R ranging only from 0.50 to 0.53 and RMSE remaining high at 0.052–0.055 km^{-1}. Notably, the low linear regression slopes (0.46–0.51) of the original simulation indicate a tendency to underestimate aerosol extinction intensity under high-loading conditions. In contrast, after correction by the GC-TF model, the AEC data points converge significantly toward the 1:1 line. The R for AEC improves to 0.66–0.73, the RMSE decreases by approximately 25% (to 0.039–0.042 km^{-1}), and the regression slope recovers to 0.55–0.60. These results demonstrate that the framework effectively reduces random biases and realigns the dynamic range of simulated extinction with observations.

Despite these substantial statistical improvements, visual scatter remains in the density plots. To rigorously quantify these discrepancies, an error envelope of ±0.15 km^{-1} is introduced in Figure 6(d–f). Statistical analysis indicates that outliers exceeding this threshold account for only 1.20% of the total dataset. Further diagnostic analysis (detailed in Sect. S10) reveals that these extreme deviations are not random noise but exhibit distinct spatial clustering over major emission hotspots (e.g., the IGP, the NCP, and the Indochina Peninsula), and are vertically confined within the PBL (<1.5 km AGL). These residuals are primarily driven by representativeness errors: CALIOP's narrow footprint captures transient, highly concentrated sub-grid aerosol plumes, which are inherently smoothed out during the spatial averaging process across the coarse 2°×2.5° grid of GEOS-Chem. Consequently, the GC-TF model captures the systematic, state-dependent biases of the grid mean, rather than fitting stochastic sub-grid extremes.

It is acknowledged that the high proportion of clean background samples (e.g., in the upper troposphere) contributes to the overall correlation metrics. To rigorously assess the model's capability in capturing effective aerosol signals—rather than merely

fitting the zero-value baseline—we conduct a threshold-based sensitivity analysis (Fig. S9~~8~~). As the extinction threshold increases from 0.00 to 0.20 km^{-1}, effectively filtering out background noise and isolating optically thick aerosol layers, the GC-TF model consistently outperforms the original GEOS-Chem simulation across all three independent test years. Although the R values naturally decline as the sample size shrinks to focus exclusively on extreme pollution events (indicated by the declining gray dashed line in Fig. S9~~8~~), the corrected results maintain a persistent performance advantage over the original simulation. This confirms that the framework effectively rectifies structural biases in high-AEC regimes and that its performance gains are not merely artifacts of correctly predicting clean background states.

Further analysis of the vertical structure reveals more complex characteristics of the model AEC bias. The annual mean vertical extinction profiles for the three test years (Fig. 7) reveal a phenomenon: although the low slope in the scatter plots implies an "underestimation" of strong signals, the annual mean profiles reveal that the original GEOS-Chem exhibits a systematic "overestimation" relative to CALIOP observations within the boundary layer (<2 km). This apparent contradiction between macroscopic statistical metrics and the vertical mean state actually exposes the typical "excessive diffusion" issue in CTM simulations: the model struggles to capture the peaks of extreme pollution events (leading to regression slopes<1) while systematically overestimating widespread background aerosol concentrations (resulting in higher intercepts and a systematic overestimation of the mean profile). The GC-TF model successfully addresses this by performing a bidirectional correction: mitigating the systemic overestimation in background regions while recovering the high-loading signals attenuated by model diffusion. In particular, the corrected results neither introduce spurious artifacts nor result in over-smoothing, accurately preserving vertical variation trends consistent with observations even in the free troposphere where aerosol loading is low.

It is important to note that while the absolute magnitude of the residual error (i.e.,

the remaining bias of the corrected AEC relative to observations) remains highest in the near-surface layer (0–1 km) due to the significantly higher aerosol base loading in the PBL (Fig. 7), the GC-TF model demonstrates its most critical contribution in this 0–1 km layer. It effectively bridges the gap between original simulations and observations, reducing the mean AEC simulation bias by 33%–95% across the independent test years (Fig. 7). Seasonal analysis (Fig. S10~~9~~) further confirms that the model robustly reduces simulation biases in the near-surface layer, regardless of the season. This substantial reduction in near-surface bias is particularly vital for accurately deriving surface $PM_{2.5}$ concentrations and assessing aerosol health impacts.

The model's capacity to capture spatial heterogeneity is further validated through regional analysis (Figs. S110–132) and explicit vertical bias profiles (Fig. S143). Rather than merely learning a globally uniform bias factor, the GC-TF model exhibits significant state-dependent adaptability. In the anthropogenic-dominated NCP and IGP, as well as the dust-dominated Taklamakan Desert, where the original model shows significant underestimation (Figs. S110–132a, b, c), the GC-TF model successfully enhances the AEC to match observations, effectively pulling the negative bias profiles back toward the zero-reference line (Fig. S143a–c). Additionally, in the Indochina Peninsula, GEOS-Chem exhibits a spurious extinction peak near 0.8 km (Fig. S110d) likely due to mischaracterized injection heights of biomass burning smoke. The GC-TF model significantly attenuates this spurious peak. Conversely, over the relatively clean Western Pacific, the model effectively reduces simulated values to address overestimation (Fig. S110f). This ability to adaptively adjust the correction direction—enhancing in polluted regions while suppressing in clean marine environments—confirms the model's sensitivity to diverse underlying surfaces and emission regimes.

4.2.2 Restoration of Zonal Mean and Longitudinal Vertical Structures

To further evaluate the model's precision~~fidelity~~ in resolving the macroscopic spatial-vertical structure of AEC, we analyze the zonal mean vertical distribution of AEC over EA (70°E–150°E) for the 2019 test year (Fig. 8). CALIOP observations (Fig.

8a) identify a prominent aerosol high-loading belt concentrated between 20°N and 30°N, corresponding to major anthropogenic sources in South and East Asia. This aerosol layer is predominantly confined to the lower troposphere below 2 km, with a high-extinction core concentrated within the lowest 1 km. In contrast, the original GEOS-Chem simulation (Fig. 8b) exhibits a characteristic "excessive diffusion" bias: the high-extinction layer is vertically over-extended (reaching above 3 km) and meridionally spread into the clean tropical regions south of 10°N, resulting in a southward displacement of the pollution center. The GC-TF model successfully rectifies these biases by re-centering the high-concentration core to the observed 25°N latitude and effectively constraining the vertical extent of the aerosol layer. By constraining the vertical extent of aerosols, the model reduces the spurious diffusion into the free troposphere and restores the peak extinction intensity suppressed by model smoothing.

Figure 9 further illustrates the annual mean longitudinal vertical cross-sections of AEC along two key latitudinal transects (38.0°N and 40.0°N). These transects capture the transition from continental dust sources and anthropogenic centers to downwind marine regions. (1) Along the 38.0°N transect: CALIOP data (Fig. 9a) reveal two distinct high-extinction cores: the Taklamakan Desert (75°E–85°E) and the NCP (115°E–120°E). The original GEOS-Chem model (Fig. 9c) almost completely fails to capture the intense near-surface dust accumulation in the Taklamakan region—likely due to uncertainties in dust emission schemes or terrain smoothing effects in the CTM—and severely underestimates the core intensity over the NCP. The GC-TF model (Fig. 9e) successfully recovers the missing dust signal and sharpens the anthropogenic core over the NCP, restoring high extinction values (>0.16 km^{-1}) within the 0–1 km layer to match observations. (2) Along the 40.0°N transect: This profile highlights model performance over Northeast Asia and the Sea of Japan. CALIOP detects a concentrated high-extinction core over the North Korea (~127°E). While the original model (Fig. 9d) significantly underestimates this peak, the GC-TF (Fig. 9f)

effectively~~accurately~~ capture~~reconstruct~~s this local anthropogenic hotspot. Notably, the original GEOS-Chem exhibits unphysical aerosol "blobs" over the Sea of Japan (135°E–138°E) and near 148°E, which are unsupported by observations. The GC-TF model effectively suppresses these model artifacts, ensuring that the extinction distribution in the downwind marine regions maintains physical consistency with CALIOP observations.

4.2.3 Correction of AOD and Assessment of Spatial Generalization

Figure 10 presents a comprehensive evaluation of the GC-TF model's performance in correcting column-integrated AOD biases over both the primary study domain (EA) and an independent generalization domain (NA). By comparing CALIOP observations, original GEOS-Chem simulations, and the GC-TF model results, we elucidate the model's efficacy in reproducing spatial heterogeneity and improving statistical consistency.

Within the EA training domain, although the original GEOS-Chem simulation (Figs. 10a2, b2, c2) captures the macroscopic features of aerosol distribution, it exhibits significant systematic biases. Specifically, it tends to underestimate AOD intensity over major anthropogenic source regions (the NCP and the IGP) and biomass burning hotspots (the Indochina Peninsula), while simultaneously introducing spurious background aerosols over the cleaner Tibetan Plateau and Western Pacific. In contrast, the GC-TF model (Figs. 10a3, b3, c3) significantly sharpens spatial gradients. The corrected AOD fields show high agreement with CALIOP observations (Figs. 10a1, b1, c1), effectively recovering high-value centers in polluted regions while suppressing false positives in clean areas. Statistical evaluation further confirms this improvement: while the original simulation shows dispersed scatter plots with low slopes (0.65–0.74), the GC-TF corrected data tightly converge onto the 1:1 identity line. The R improves from 0.80–0.84 to 0.91–0.93, the RMSE decreases by approximately 26%–40%, and the regression slope recovers to 0.82–0.99 (Figs. 10a5, b5, c5). The temporal consistency observed from 2017 to 2019 indicates that the model has learned stable

physical mapping relationships rather than overfitting to specific meteorological years.

Crucially, the evaluation over the NA domain (Fig. 10d) provides compelling evidence of the model's spatial generalization capability. Despite the significantly lower AOD magnitude and distinct emission characteristics compared to EA, the GC-TF model demonstrates robust transferability. The original GEOS-Chem simulation over NA (Figs. 10d2, d4) shows poor agreement with observations (R=0.31, slope=0.18), indicating severe deficiencies in capturing regional aerosol variability. Specifically, it underestimates anthropogenic pollution sources in the Eastern US (Fig. 10d1) and exhibits spurious high-AOD trails over the Gulf of Mexico and the East Coast, likely due to excessive transport or overestimated sea salt. Applying the GC-TF model—trained exclusively on EA data—to this unseen region (Figs. 10d3, d5) yields a substantial performance leap: R more than doubles to 0.70, and the slope improves to 0.45. Spatially, the model successfully recovers the smoothed pollution peaks in the Eastern US and corrects the oceanic regions to clean background levels, consistent with CALIOP. This bidirectional correction capability—enhancing underestimated terrestrial signals while suppressing overestimated oceanic backgrounds—strongly suggests that the physics-informed Transformer framework has captured the universal physical linkages between atmospheric states and simulation biases, rather than merely memorizing the geographical features of the EA training domain.

4.3 Mechanisms of Cross-Continental Transferability

The robust generalization capability demonstrated in the NA domain relies on the universality of atmospheric physical laws. While EA and NA differ vastly in emission intensities and aerosol regimes, core physicochemical processes governing aerosol lifecycles remain consistent. The GC-TF model recognizes familiar synoptic patterns and successfully transfers these learned physical constraints across continents. This capability is well evidenced by its bidirectional correction over distinct underlying surfaces. Over the Eastern United States, the model mitigates the Eulerian smearing effect~~The robust generalization capability demonstrated in the NA domain is~~

~~fundamentally underpinned by the universality of atmospheric physical laws. While EA and NA differ vastly in emission intensities and aerosol composition regimes, the fundamental physicochemical processes governing aerosol lifecycles (e.g., hygroscopic growth, turbulent mixing, and wet deposition) adhere to universal physical laws. The robust performance in the NA domain (R=0.70) indicates that the systematic biases in GEOS-Chem are predominantly state-dependent rather than location-dependent. Specifically, CTMs tend to exhibit consistent "error signatures" under specific meteorological conditions. When the GC-TF model encounters similar synoptic patterns in NA, the self-attention mechanism identifies these familiar meteorological contexts and applies the learned correction rules. In this sense, the meteorological background acts as a bridge, facilitating the transfer of bias-correction capabilities across continents.~~

~~The model's capability is further highlighted by its bidirectional correction performance over distinct underlying surfaces. Over the Eastern United States, the model successfully mitigates the "smearing effect" characteristic of Eulerian models~~ (Rastigejev et al., 2010; Eastham and Jacob, 2017). It restores sharp spatial gradients and high-intensity anthropogenic pollution cores. Over marine regions like the Gulf of Mexico, it effectively suppresses spurious background aerosols often driven by excessive transport or sea-salt overestimation. The model dynamically utilizes multidimensional atmospheric variables to physically constrain spatial distributions rather than applying a simple uniform correction factor.

Despite these capabilities, the overall correction performance in NA (R=0.70) remains statistically lower than in the EA training domain (R=0.93). We hypothesize that this performance gap originates from a fundamental domain shift in aerosol composition. The NA atmosphere features lower background concentrations and a significantly higher fraction of biogenic Secondary Organic Aerosols (SOA)~~, restoring the sharp spatial gradients and high-intensity cores of anthropogenic pollution that were overly smoothed in the original simulation. Conversely, over marine regions such as~~

~~the Gulf of Mexico and the Atlantic coast, the model effectively suppresses the spurious background aerosols often caused by excessive transport or sea-salt overestimation. This adaptive behavior—enhancing peaks over land while suppressing artifacts over oceans—confirms that the model utilizes multi-dimensional atmospheric variables to constrain the spatial distribution of aerosols physically, rather than applying a uniform bias correction factor. It is noteworthy, however, that the correction performance in NA (R=0.70) remains statistically lower than in the EA training domain (R=0.93). This performance gap is likely attributable to the "domain shift" in aerosol composition. The NA atmosphere is characterized by lower background concentrations and a higher fraction of biogenic secondary organic aerosols~~ (Goldstein et al., 2009)~~,~~ The optical properties and hygroscopicity of these organic species differ fundamentally from the sulfate-nitrate-dust mixtures dominating EA~~whose optical properties and hygroscopicity differ from the sulfate-nitrate-dust dominated mixtures in EA~~ (Crawford et al., 2021)~~. This suggests that while the physical laws of transport are universal, chemical-specific optical relationships may require broader representativeness in the training data for further refinement~~.

To quantitatively verify this impact, we further evaluate the model performance stratified by CALIOP aerosol subtypes over NA (Table S4). The results reveal a clear divergence in the model's corrective capability across distinct aerosol regimes. For dust-dominated regimes, the model effectively mitigates GEOS-Chem's systematic underestimation, enhancing the regression slope from 0.21 to 0.32 and increasing R from 0.41 to 0.50. This confirms that the physical constraints governing dust extinction and vertical transport learned in EA translate reliably to the NA domain. In contrast, the model yields negligible improvements for the SOA-dominated continental regime. Although total mass concentrations are provided as predictors, the specific thermodynamic-to-optical mapping learned in EA—typically dominated by the high hygroscopic growth of inorganic salts—is less applicable to the complex, weakly hygroscopic biogenic SOA prevalent in NA. The stagnant RMSE and R in the SOA

group suggest that without locally representative training samples to capture the unique mass extinction efficiencies and refractive indices of NA-specific organic species, the data-driven framework maintains a conservative correction. This ultimately limits the overall precision gain across the NA background.

4.4 Case Studies: Vertical Structure and Temporal Evolution During High Aerosol Loading Periods

To thoroughly evaluate the GC-TF model's capability in resolving complex vertical AEC stratification and capturing high-frequency pollution dynamics, we conduct a composite analysis of representative high-loading episodes identified by CALIOP over three distinct aerosol regimes (details in ~~Section~~ Sect. 2.3).

In the Taklimakan Desert (Fig. 11a), the original GEOS-Chem simulation exhibits a nearly vertical extinction profile with extremely low values, indicating that the CTM fails to simulate the significant aerosol extinction layer observed by CALIOP. In contrast, the GC-TF model effectively recovers~~reconstructs~~ the extinction signal in this region by leveraging multidimensional input atmospheric state variables (including meteorological fields and background chemical composition). Its profile shape shows superior agreement with satellite observations, largely retrieving the "missing signal" of the original simulation. In Kanpur, a region dominated by anthropogenic pollution (Fig. 11b), the original model fails to accurately capture the magnitude and vertical gradient of the pollution layer below 3.5 km. The GC-TF model, while correcting baseline errors, reshapes the vertical distribution pattern, yielding a vertical decrement trend that aligns closely with observational reality. Figure 11c reveals critical structural biases during a biomass burning event in the Indochina Peninsula. The original GEOS-Chem simulation presents an "inverted" vertical gradient, where the extinction peak appears at a height of 2.5 km rather than near the surface. This bias is likely associated with uncertainties in the parameterization of biomass burning Plume Injection Height in the CTM, suggesting the model erroneously transports surface smoke into the free troposphere (Paugam et al., 2016). The GC-TF model successfully identifies this

physical process bias; by significantly enhancing AEC below 2.0 km, it restores a near-surface high-loading pattern consistent with observations, while maintaining reasonable simulation magnitudes in the free troposphere.

In addition to the instantaneous vertical structure, verifying the temporal continuity of the correction results is equally crucial. Given the spatiotemporal sparsity of CALIOP observations, we utilize ground-based high-frequency AERONET AOD data to further evaluate model performance. A critical concern regarding DL models trained on polar-orbiting satellite data is the potential overfitting to the sensor's limited twice-daily sampling timing (e.g., ~01:30 and 13:30 local time for CALIOP). However, the continuous AOD time series output by the GC-TF model demonstrates superior trend consistency with the high-frequency AERONET observations throughout all daylight hours. Figure 11d-e show the corrected model successfully captures the dynamic diurnal evolution and phase fluctuations of aerosols. Specifically, Figure 11d shows that during the study period in Kanpur, the original GEOS-Chem simulation generally underestimates aerosol loading, and the curve exhibits overly smooth characteristics, lacking response to high-frequency fluctuations. In contrast, the GC-TF model closely tracks these dynamic variations.~~The AOD time series output by the GC-TF model demonstrates superior trend consistency with AERONET observations.~~ Notably, between May 1 and May 2, the original simulation shows significant overestimation, whereas the GC-TF model successfully adjusts the predicted values back to levels closer to observations. During the active fire period in Nong Khai (Fig. 11e), the original model severely underestimates the AOD magnitude. The GC-TF model significantly elevates the simulation baseline and captures the phase of diurnal variation trends well (e.g., the fluctuations around 07:00 UTC during February 22–24). This empirical evidence confirms that by conditioning the bias correction on meteorology-driven diurnal processes (as discussed in Sect. 3.1), the framework robustly generalizes across the entire diurnal cycle and avoids overfitting to specific CALIOP overpass times.

However, its predicted peak amplitudes remain significantly lower than the extreme values observed by AERONET. This dampening of extreme peaks likely stems from the spatial scale mismatch between the gridded model (2°×2.5°) and ground-based point observations, which causes local extreme emissions to be averaged out within the grid. Nonetheless, the GC-TF model demonstrates significant improvement over the original CTM in reproducing meteorology-driven pollution accumulation and dispersion processes.

4.5 Interpretability Analysis

To move beyond statistical performance and elucidate the underlying physical mappings learned by~~internal decision-making logic of the~~ the correction~~GC-TF~~ framework~~model~~, we employ a hierarchical diagnostic approach~~multi-perspective interpretability framework~~ to quantify feature contributions~~ and interaction mechanisms~~. This section and the subsequent analysis are based entirely on the independent test dataset, ensuring that the interpretations reflect the model's generalized physical representations on unseen data.

4.5.1 Domain-Wide Reliance and Altitude-Dependent Prioritization ~~Macro-Physical Logic: Physicochemical Baseline and Contextual Correction~~

To understand how the ~~DL~~ model resolves~~reconstructs~~ 3D aerosol fields, we first examine its overarching reliance on~~the macroscopic contribution of~~ different information streams~~sources~~. Domain-wide permutation feature importance~~Global sensitivity tests~~ (Fig. S154) unambiguously establishes the foundational role of physical priors: randomly permuting the physicochemical profile ~~features~~ induces a dramatic 196.1% increase~~surge~~ in MSE. This confirms that ~~while the Transformer architecture excels at extracting spatiotemporal patterns,~~ the physicochemical profiles~~state features~~ provided by the CTM remain the indispensable physical foundation, ~~essentially~~ determining the absolute~~"Base~~ Magnitude~~"~~ of the AEC. In contrast~~this framework~~, spatial, temporal, and height components~~height features~~ function as modulating variables~~"Correction Factors,"~~ refining this baseline ~~by~~ across diverse environmental

regimes.~~integrating multidimensional environmental contexts.~~

Further analysis of the gated feature fusion weights (Fig. 12) reveals that the model effectively ~~learns to~~ adapts its prioritization mechanism~~differentiate its correction strategy~~ based on atmospheric stratification.~~the dominant physical processes at different atmospheric stratifications: (1)~~ In the near-surface layer (<0.5 km), the model assigns the highest weight to physicochemical profiles~~profile features.~~. ~~This~~ align~~ings~~ with the physical reality that extinction near the surface is predominantly controlled by local emissions~~local instantaneous states~~ and immediate thermodynamic states~~—specifically emission intensities and hygroscopic growth~~ (Jiang et al., 2024; Xiong et al., 2025).~~The model accurately identifies that these physicochemical variables are the most critical determinants of extinction magnitude in the lowest layer. (2)~~ As height increases to the boundary layer transition zone (0.5–1.0 km), a strategic shift occurs. The reliance on physicochemical profiles~~raw simulation profiles~~ diminishes~~,~~ while the weight of spatial coordinates~~features~~ increases significantly. This region typically corresponds to the entrainment zone or the top of the ~~nocturnal boundary layer~~PBL, where CTMs are prone to vertical diffusion errors (Eastham and Jacob, 2017; Rastigejev et al., 2010; Lin and Mcelroy, 2010). The model ~~appears to~~ mitigate~~s~~ these uncertainties by leveraging spatial priors to constrain potential diffusion biases~~,~~ ~~effectively identifying "regions of uncertainty" in the simulation.~~ ~~(3)~~ In the mid-lower troposphere (1.0–3.5 km), the contribution of temporal indices~~features~~ exhibits distinct peaks~~, particularly~~ around 1.5 km and 2.8 km. The~~ peak near~~ 1.5 km peak corresponds to the typical maximum daytime PBLH in EA (Guo et al., 2016; Kim, 2022), while the ~~signal at~~ 2.8 km peak aligns with the active layer for long-range transport (Uno et al., 2009). This demonstrates~~suggests~~ the model's utilization of~~ utilizes~~ temporal cues to capture the diurnal evolution of the ~~boundary layer~~PBL and ~~the~~ seasonal~~seasonality of trans-regional~~ transport events. ~~(4) Finally, i~~In the free troposphere (>3.5 km), ~~the dependence on local profile features fades, and spatial features become the dominant driving factor. In this region,~~ aerosol variability is vertically decoupled from ~~local~~

surface processes and driven primarily by large-scale advection (Weinzierl et al., 2017; Val Martin et al., 2013; Uno et al., 2009). The model successfully captures this ~~mechanistic~~ decoupling, shifting its strategy to rely heavily on spatial coordinates to constrain background aerosol fields~~perform position-dependent background correction using geographical coordinates~~. ~~Throughout the entire column,~~ Eexplicit height encoding maintains a consistently high contribution throughout the entire column, serving as a critical vertical positioning anchor.

4.5.2 Vertical Attribution of Local State Variables ~~Micro-Drivers of Bias Correction: Vertical Attribution of State Variables~~

Following the domain-wide ranking~~macroscopic establishment of feature importance~~, we utilize gradient-based attribution~~Integrated Gradients analysis~~ (Fig. 13) to dissect the specific ~~physical~~ variables within the VPS driving ~~extinction~~ AEC bias correction across ~~different~~ altitudes. These drivers are organized into thermodynamic constraints, particulate compositions, and dynamic factors.~~The analysis reveals that the model has constructed a sophisticated decision-making logic that effectively decouples thermodynamic constraints from compositional variables.~~

First, thermodynamic variables serve as the primary constraints for rectifying the vertical AEC structure~~structural correction~~. Temperature (T) consistently acts as the dominant driver within the PBL, with attribution scores exceeding 0.20. This ~~heavy reliance~~ suggests that the model implicitly diagnoses atmospheric stability and ~~the~~ vertical lapse rate—~~key~~ factors often mischaracterized in CTMs—to rectify biases associated with turbulent mixing~~target biases associated with turbulent mixing intensities~~ (Lin and Mcelroy, 2010). Concurrently~~Acting in concert with temperature~~, Relative Humidity (RH) functions as a critical driver for aerosol optical properties~~optical modulator~~. ~~Although its absolute attribution score is lower than that of temperature, i~~Its contribution is coupled with explicit hygroscopic growth factors (e.g., AerHygroscopicGrowth_SO_4^{2-})~~. This,~~ enabling~~es~~ the ~~Transformer~~ model to fine-tune the ~~optical~~ AEC~~, effectively~~ and correct~~ing biases arising from~~ non-linear

hygroscopic parameterization errors under high-humidity conditions (Burgos et al., 2020; Zhai et al., 2021)~~, particularly under high-humidity conditions~~.

Second, particulate mass concentrations act as the fundamental determinants of aerosol loading~~fundamental anchors for pollution intensity~~. In the lower troposphere (<1.5 km), $PM_{2.5}$ and PM_{10} consistently rank among the top drivers~~, confirming their role in determining the baseline magnitude of AEC~~. The model also demonstrates a physically stratified recognition of aerosol types; for instance, the importance of sea salt aerosol (AerMassSAL) is confined strictly to the marine boundary layer (<1.5 km) and decays rapidly aloft, accurately reflecting the vertical distribution of coarse-mode marine aerosols (Bian et al., 2019; Murphy et al., 2019).

Finally, dynamic variables exhibit a persistent influence aloft~~distinct "long-tail effect" in the vertical dimension~~. Unlike precursor concentrations which decay sharply with height, the importance of wind components (U, V) remains relatively stable in the free troposphere (>2.0 km) This indicates that as height increases, the model shifts its focus from local accumulation to large-scale advection, utilizing wind fields to rectify background biases induced by long-range transport~~. This indicates that as height increases, the model shifts its focus from local accumulation to large-scale advection, utilizing wind fields to identify and correct background biases induced by long-range transport~~.

4.5.3 Synoptic Modulation via Surface Constraints~~Modulation by Environmental Context: Synoptic and Surface Constraints~~

While the VPS~~vertical profiles~~ determine the baseline extinction, the c~~C~~ross-a~~A~~ttention mechanism enables the model to utilize the SFS~~2D global variables as "Environmental Constraints"~~ to modulate the vertical ~~reconstruction~~ bias correction (Fig. 14). This process operates through ~~two~~ distinct physical pathways~~: dynamic ventilation and radiative surface forcing~~.

First, the model employs a robust dynamic representation~~sophisticated dynamic diagnosis mechanism~~ to constrain transport and mixing efficiency. The consistently

high attention weights of 10 m wind components (U10M, V10M) ~~throughout the column~~ reflect the ~~model's~~ use of near-surface wind speed as a proxy for synoptic flow patterns. ~~Notably, t~~The model identifies the dominance of meridional transport in the EA monsoon region, assigning slightly higher importance to meridional winds (V10M) to capture dominant pollutant exchange pathways (Ding et al., 2009; Choi et al., 2024; Uno et al., 2009). By identifying prevailing dynamic regimes, the model effectively addresses ~~common~~ CTM biases related to pollutant accumulation under stagnant conditions (Kim et al., 2024; An et al., 2019) and numerical diffusion under strong advection (Rastigejev et al., 2010; Eastham and Jacob, 2017). More critically, the cross-attention weights reveal a vertical partitioning~~deep decoupling~~ of ~~boundary layer~~ turbulence drivers~~processes~~. Thermodynamic drivers (HFLUX, LAI) peak at the surface and decay upward, ~~exhibit a "surface peak, upward decay" pattern, suggesting~~diagnosing ~~the model uses them to~~ surface buoyancy fluxes~~determine the initial buoyancy potential~~. In ~~sharp~~ contrast, mechanical drivers (USTAR, Z0M) increase and plateau with height~~display an "increase and plateau" trend with height~~. This distinction implies ~~that~~ the model successfully evaluates vertical entrainment potential, assessing whether mechanical shear is sufficient to transport pollutants across capping inversions~~diagnoses the "vertical permeability" of the atmosphere—assessing whether mechanical shear is sufficient to pump pollutants through capping inversions into the free troposphere~~.

Second, radiative and surface boundary conditions are leveraged to correct parameterization biases ~~in chemical formation and stability parameterization~~. The model senses solar input by ~~The high attention assigned to photosynthetically active radiation~~ distinguishing between direct (PARDR) and diffuse (PARDF) photosynthetically active radiation~~components~~, capturing variations in photochemistry and secondary aerosol formation ~~indicates the model's implicit capture of photochemical variation. By sensing solar input, the model dynamically compensates for biases related to secondary aerosol formation rates or biogenic emissions~~ (Guenther

et al., 2012). Furthermore, snow mass (SNOMAS) emerges as a key predictor in the lowest layers. The model identifies snow-covered surfaces as indicators of stronglya proxy for "suppressed diffusion states", characterizing stable boundary layer prone to temperature inversionsconditions prone to deep near-surface inversions. This allows for the targeted correction of the "over-dilution" biases often found in Eulerian modelsCTMs (Lin and Mcelroy, 2010; Holtslag et al., 2013), effectively restoring capturing high-concentration signals in stable boundary layers that are typically artificially smoothed out by minimal diffusion threshold constraints.

4.5.4 Regional Heterogeneity of Bias Drivers Regional Heterogeneity: Spatially Distinct Physical Fingerprints

To reveal the model's predictive behaviordecision-making logic under diverse environmental contexts, we conducted SHAPa "physical fingerprint" analysis (Fig. 15) to identify region-specific correction patterns adapted to distinct underlying surfaces and emissions based on SHAP importance rankings. The results demonstrate that the model autonomously establishes three distinct physical response modes adapted to regional underlying surfaces and emission characteristics.

In regions dominated by anthropogenic and biomass burning emissionsIn high-emission anthropogenic and biomass burning regions (NCP, IGP, and Indochina), the model primarily leverages radiative components to diagnose atmospheric turbidityfor optical identification. A striking commonality across these regions is the high ranking of diffuse photosynthetically active radiation (PARDF), often surpassing the direct component (PARDR). This reflects the model's capability to capture the physical phenomenon where high aerosol loading enhances scattering and increases the diffuse fraction of solar radiation (Mercado et al., 2009; Che et al., 2018), utilizing it as a robust proxy for optical turbidity. Furthermore, the model accurately differentiates surface energy partitioning regimes: in the humid, vegetated IGP and Indochina, it prioritizes latent heat flux (EFLUX) to gauge hygroscopic growth and wet removal potential; conversely, in the urbanized NCP, it relies more heavily on sensible heat flux (HFLUX),

consistent with the high Bowen ratio of urban surfaces (Miao et al., 2009) where thermal turbulence dominates vertical dispersion.

In the dust-dominated Taklamakan Desert, the model captures a coupled~~reconstructs a closed loop~~ mechanism driven by ~~"T~~thermodynamic instability~~Forcing~~ and d~~D~~ynamic u~~U~~plift.~~".~~ Incident shortwave flux (SWGDN) and direct radiation (PARDR) play a~~n overwhelmingly~~ dominant role, indicating that the model identifies clear-sky, high-solar-input conditions as ~~the~~ prerequisites for ~~thermodynamic background for inducing~~ thermal instability. Crucially, this ~~thermodynamic setup~~ is coupled with dynamic ~~and surface~~ descriptors: ~~the model~~ combining~~es~~ low vegetation indices (GRN, identifying erodible bare soil), high 10m wind speeds (providing surface shear stress) (Shao et al., 2011), and a preference for coarse-mode PM_{10} over $PM_{2.5}$. This ~~combination~~ confirms ~~that~~ the ~~Transformer~~ model has ~~successfully~~ learned the physical prerequisites~~process~~ for~~of~~ wind-driven dust emission in arid ~~source~~ regions.

Finally, over the marine environment of the Western Pacific, the model shifts to a l~~"L~~atent h~~H~~eat-d~~D~~riven~~"~~ mode. Latent heat flux (EFLUX) ~~contributes nearly half of the total feature importance,~~ defining the moisture supply at the air-sea interface ~~that~~, controlling~~s~~ marine aerosol hygroscopicity. Additionally, the model captures ~~the mechanics of~~ sea spray generation ~~–~~by linking near-surface wind speeds (V10M) with land-sea masking indicators (GRN)~~. This suggests the model~~, recognizing~~es~~ that ~~under high-wind conditions over water,~~ mechanically generated sea salt aerosols (Grythe et al., 2014) ~~—~~and their subsequent hygroscopic evolution ~~—~~are the primary drivers of AEC variability over open water.

4.6 Diagnostic Insights for Refining GEOS-Chem Parameterizations~~Feedback from Data-Driven Correction to Physical Model Improvement~~

The interpretability analysis in Section 4.5 demonstrates that the GC-TF model captures physically meaningful relationships rather than merely fitting statistical noise. While directly translating data-driven feature sensitivities into concrete code

modifications remains challenging without further sensitivity simulations, this transparency allows the framework to serve as a valuable hypothesis-generation tool. It highlights potential structural uncertainties in CTMs and points toward targeted refinements in physical parameterizations~~The interpretability analysis in Section 4.5 demonstrates that the GC-TF model does not merely fit statistical biases but successfully reconstructs a closed-loop physical logic governing aerosol vertical structure. This "physics-informed" transparency offers a unique opportunity to diagnose the root causes of CTM biases and establish a feedback loop for model improvement~~.

4.6.1 Diagnosing Thermodynamic Parameterization Deficiencies

The model heavily relies on temperature and HFLUX to correct AEC profiles (Sect. 4.5.2, 4.5.4), which suggests potential uncertainties in diagnosing PBLH and turbulent mixing intensity within the GEOS-Chem non-local boundary layer scheme. Given that HFLUX drives surface buoyancy and directly modulates the vertical eddy diffusion coefficient, the widespread excessive diffusion biases observed in the lower troposphere indicate that the model may overestimate thermal turbulence under certain stability conditions. In highly urbanized regions like the NCP, the acute sensitivity to HFLUX implies that current surface energy balance calculations struggle to resolve the distinct thermodynamic properties of urban canopies. Future model development could benefit from constraining stability functions within the vertical diffusion module, or alternatively, coupling a dedicated urban canopy model to better represent sensible heat partitioning~~The model's dominant reliance on temperature and sensible heat flux (Sections 4.5.2, 4.5.4) to correct vertical profiles strongly implies that the original GEOS-Chem simulation suffers from structural deficiencies in diagnosing PBLH and mixing intensity. Specifically, the "excessive diffusion" biases observed in the lower troposphere suggest that the CTM may misinterpret thermodynamic stability over complex underlying surfaces. In highly urbanized regions like the NCP, the model's high sensitivity to sensible heat flux indicates that the current scheme may not fully resolve the distinct energy budget of urban canopies. This suggests that future~~

~~improvements should prioritize refining stability-dependent diffusion coefficients or implementing more explicit parameterizations for urban surface energy balance to better constrain vertical mixing~~.

4.6.2 Refining Emission and Formation Schemes via Environmental Proxies

The cross-attention weights, which reveal how synoptic forcing modulates vertical aerosol profiles (Sect. 4.5.3, 4.5.4), highlight potentially inadequately parameterized mechanisms in current emission and chemical modules. Over the Taklamakan Desert, the model explicitly pairs greenness fraction with surface wind speed to capture dust extinction. This suggests that the GEOS-Chem dust emission scheme might struggle to accurately parameterize threshold friction velocity over complex bare soils, indicating that the non-linear response of wind-blown dust to surface shear stress and soil erodibility likely requires recalibration. Similarly, high sensitivity to diffuse radiation in the biomass burning region of Indochina points to potentially under-represented SOA formation. Given that high aerosol loading enhances diffuse radiation and alters photolysis rates, the data-driven model likely leverages diffuse radiation as a proxy for accelerated photochemical aging. This highlights a need to optimize SOA yield parameterizations and refine biomass burning plume injection heights to capture rapid aerosol evolution in dense smoke~~The "context-aware" behavior of the Transformer reveals missing process-level links in the current CTM emission and formation modules. In the Taklamakan Desert, the model explicitly combines GRN (identifying bare soil) and Wind Speed to reconstruct dust extinction. The fact that the DL model requires these specific inputs to correct the simulation implies that the original dust emission scheme likely fails to accurately capture the non-linear threshold between wind shear and erodible surfaces, potentially miscalculating the threshold friction velocity or wind-erosion efficiency. Similarly, in Indochina, the high sensitivity to diffuse radiation (PARDF) suggests that secondary organic aerosol formation associated with biomass burning plumes is under-represented. The model compensates for this by using radiation as a proxy for photochemical aging rates, pointing to a need for optimizing~~

~~secondary organic aerosol formation mechanisms and injection height parameterizations in the CTM~~.

4.6.3 Bridging Data-Driven Interpretation with CTM Development~~The Role of Machine Learning in Earth System Modeling~~

Beyond statistical bias correction, this study highlights the utility of physics-informed DL for model diagnosis. By decoupling the contributions of meteorology and aerosol composition, the framework verifies that CTMs provide a robust physicochemical baseline, yet exhibit uncertainties in representing the complex, non-linear interactions between aerosols and meteorology. The correction strategies derived from the data-driven model offer valuable diagnostic clues. Identifying specific environmental proxies that govern simulation biases bridges the gap between data-driven retrieval and deterministic modeling, ultimately guiding the targeted integration of neglected physical constraints into future parameterization schemes~~Beyond bias correction, this study exemplifies a paradigm shift from "black-box" prediction to "glass-box" diagnosis. By decoupling the contributions of meteorology and composition, the physics-informed Transformer serves as a diagnostic tool. It verifies that while CTMs provide a solid physicochemical baseline, they struggle with the non-linear modulation of local environmental contexts. The correction strategies learned by the model—such as using GRN as a dynamic land mask or SNOMAS as a stability indicator—provide traceable scientific evidence for incorporating these neglected environmental constraints into future deterministic parameterization schemes~~.

4.7 Model Limitations and Scope of Application

As a supervised bias-correction framework, the model relies on state-dependent mapping, meaning its performance is fundamentally constrained by the predictive signals available in the input features. The framework excels at correcting systematic, parameterization-driven bias. For instance, it successfully restores the underestimated dust plumes in the Taklamakan Desert by leveraging wind speed, clear-sky radiation, and vegetation indices as physical proxies for actual dust emission conditions (Sect.

4.5.4).

However, the model possesses limited capacity to compensate for entirely missing physical processes. If a highly localized or stochastic event is completely absent from the prescribed emission inventory and produces no corresponding anomalies in the input meteorological or chemical precursor fields, the model lacks the necessary physical constraints to capture the resulting aerosol plume. In such scenarios, the correction remains strictly bounded by the prior information provided by the GEOS-Chem and MERRA2.

带格式的：缩进：首行缩进： 2 字符

5. Conclusions

This study proposes a physics-informed Transformer DL framework that generates ~~reconstructs~~ high-precision 3D AEC fields by bridging the gap between CTM simulations and CALIOP satellite observations. Functioning as a supervised bias-correction model rather than a DA system, this framework learns a state-dependent mapping to rectify systematic simulation AEC bias. Distinct from traditional bias correction methods that rely solely on passive remote sensing imagery or treat the model as a "black box," this framework explicitly integrates physicochemical vertical structural priors (e.g., AEPs and species concentrations) from GEOS-Chem and meteorological constraints from MERRA-2. By constructing a dual-stream architecture featuring Gated Feature Fusion and Cross-Attention mechanisms, the model effectively captures the complex, non-linear dependencies between atmospheric states and AEC simulation biases. The primary conclusions are as follows:

First, the framework significantly improves the precision~~fidelity~~ of AEC vertical profiles, systematically correcting the systematic biases inherent in Eulerian CTMs. Extensive "LOYO~~Leave-One-Year-Out~~" cross-validation over EA (2017–2019) demonstrates that the R for AEC evaluated against CALIOP observations increases from 0.49–0.53 in the original GEOS-Chem simulation to 0.66–0.73, while the RMSE is reduced by approximately 25%. Vertically, the model achieves optimal performance

within the PBL (0.5–1.5 km), with R consistently exceeding 0.7 and NRMSE remaining below 5%. The framework effectively mitigates the "excessive diffusion" issue common in CTMs, rectifying the spurious southward displacement of pollution centers, restoring smoothed high-intensity extinction signals in anthropogenic and dust source regions, and suppressing spurious overestimations in the clean free troposphere and over marine regions. Crucially, threshold-based sensitivity analysis confirms that these performance gains are robust even when focusing exclusively on optically thick aerosol layers. Consequently, this vertical rectification leads to a substantial improvement in column-integrated AOD, with the R relative to CALIOP increasing from 0.80–0.84 to 0.91–0.93 across the EA domain, ensuring consistency between resolved AEC vertical structures and the total aerosol load. Moreover, validation against high-frequency ground-based AERONET measurements confirms the framework's superiority over the original GEOS-Chem simulation in capturing the dynamic temporal evolution of pollution episodes, bridging the observational gaps inherent to the sparse sampling of polar-orbiting satellites.

Second, the model exhibits robust cross-continental transferability, indicating that it has internalized universal physical laws rather than overfitting to regional training characteristics. When applied directly to the NA domain—a region with distinct emission structures and lower aerosol loading—without any retraining, the model successfully reproduces the spatial AEC simulation bias patterns of GEOS-Chem. The R for column-integrated AOD compared with CALIOP retrievals in this region improves significantly from 0.31 (original) to 0.70 (corrected), further verifying the physical consistency and transferability of the established mapping between atmospheric states and AEC simulation biases.

Third, by integrating interpretable DL techniques, this study advances beyond standard bias correction to serve as a diagnostic framework for physical mechanisms.~~establishes a closed-loop feedback pathway from "data-driven correction" to "physical mechanism diagnosis."~~ Attribution analysis reveals that the model

~~autonomously~~ identifies AEC simulation bias drivers with clear physical significance: (1) In the PBL, the heavy reliance~~model relies primarily~~ on temperature and HFLUX~~sensible heat flux~~ highlights potential uncertainties~~to correct vertical mixing biases, pointing to deficiencies~~ in~~–~~ vertical eddy diffusion coefficients within stability-dependent ~~diffusion~~ mixing schemes~~ within the CTM~~; (2) Over dust source regions, the paired use of~~The synergistic diagnosis of dust emission thresholds using~~ vegetation indices and wind speed suggests the need to recalibrate~~potential biases in~~ threshold friction velocity and soil erodibility~~the non-linear response of existing dust parameterizations to wind erosion mechanisms~~; (3) In biomass burning regions, the sensitivity to diffuse radiation points to under-represented~~reveals missing links in secondary organic aerosol~~SOA yields~~formation processes~~ and photochemical aging processes~~or plume injection height parameterizations~~; (4) In marine regions, the utilization of~~the model utilizes~~ latent heat flux and surface wind implies uncertainties in sea-salt generation functions and hygroscopic growth ~~patterns to target and correct potential overestimation biases in sea salt aerosol generation functions or hygroscopic growth parameterizations~~.

In summary, this study not only confirms the effectiveness of the physics-informed Transformer in deriving~~reconstructing~~ high-precision~~fidelity~~ 3D aerosol fields to support radiative forcing assessments but also highlights its potential as a diagnostic tool for ~~Earth system modeling~~CTMs. The interpretability analysis provides developers with actionable physical insights, highlighting a shift in the integration of ~~deep learning~~DL with physical modeling. Rather than serving solely as a post-processing tool for bias correction, the framework functions as a diagnostic mechanism to identify structural model deficiencies and guide the refinement of parameterization schemes in ~~Earth system models~~CTMs.

Code and Data availability. The GEOS-Chem model is available at http://www.geos-chem.org. The CALIOP satellite data can be accessed via

https://subset.larc.nasa.gov/calipso. The MERRA-2 data are available from the NASA Goddard Earth Sciences Data and Information Services Center (https://disc.gsfc.nasa.gov/). AERONET data can be obtained from https://aeronet.gsfc.nasa.gov/. The source code of the physics-informed Transformer model proposed in this study and the trained weights are available upon request from the corresponding author.

Author contribution. JX designed the research, developed the model methodology, conducted the simulations, performed the data analysis, and prepared the original draft. YW supervised the study, provided the computing resources, and revised the manuscript. JW revised the manuscript. YYW, MZ, MT, WD, JK, and LW provided technical support and reviewed the manuscript. All authors contributed to the interpretation of the results and the improvement of the paper.

Competing Interests. The contact author has declared that none of the authors has any competing interests.

Acknowledgements. This research was funded by the National Natural Science Foundation of China (Grant No. 42571377). Jun Wang's participation is made possible via the in-kind support (Lichtenberger Family Chair in Chemical Engineering) from the University of Iowa.

References

An, Z., Huang, R. J., Zhang, R., Tie, X., Li, G., Cao, J., Zhou, W., Shi, Z., Han, Y., Gu, Z., and Ji, Y.: Severe haze in northern China: A synergy of anthropogenic emissions and atmospheric processes, Proc. Natl. Acad. Sci. U.S.A., 116, 8657-8666, 10.1073/pnas.1900125116, 2019.

Benedetti, A., Reid, J. S., Knippertz, P., Marsham, J. H., Di Giuseppe, F., Rémy, S.,

1453 Basart, S., Boucher, O., Brooks, I. M., Menut, L., Mona, L., Laj, P., Pappalardo,
1454 G., Wiedensohler, A., Baklanov, A., Brooks, M., Colarco, P. R., Cuevas, E., da
1455 Silva, A., Escribano, J., Flemming, J., Huneeus, N., Jorba, O., Kazadzis, S., Kinne,
1456 S., Popp, T., Quinn, P. K., Sekiyama, T. T., Tanaka, T., and Terradellas, E.: Status
1457 and future of numerical atmospheric aerosol prediction with a focus on data
1458 requirements, Atmos. Chem. Phys., 18, 10615-10643, 10.5194/acp-18-10615-
1459 2018, 2018.
1460 Bey, I., Jacob, D. J., Yantosca, R. M., Logan, J. A., Field, B. D., Fiore, A. M., Li, Q. B.,
1461 Liu, H. G. Y., Mickley, L. J., and Schultz, M. G.: Global modeling of tropospheric
1462 chemistry with assimilated meteorology: Model description and evaluation, J.
1463 Geophys. Res.:Atmos., 106, 23073-23095, 10.1029/2001jd000807, 2001.
1464 Bian, H. S., Froyd, K., Murphy, D. M., Dibb, J., Darmenov, A., Chin, M., Colarco, P.
1465 R., da Silva, A., Kucsera, T. L., Schill, G., Yu, H. B., Bui, P., Dollner, M., Weinzierl,
1466 B., and Smirnov, A.: Observationally constrained analysis of sea salt aerosol in the
1467 marine atmosphere, Atmos. Chem. Phys., 19, 10773-10785, 10.5194/acp-19-
1468 10773-2019, 2019.
1469 Bocquet, M., Pires, C. A., and Wu, L.: Beyond Gaussian Statistical Modeling in
1470 Geophysical Data Assimilation, Mon. Wea. Rev., 138, 2997-3023,
1471 10.1175/2010mwr3164.1, 2010.
1472 Bond, T. C., Doherty, S. J., Fahey, D. W., Forster, P. M., Berntsen, T., DeAngelo, B. J.,
1473 Flanner, M. G., Ghan, S., Kärcher, B., Koch, D., Kinne, S., Kondo, Y., Quinn, P.
1474 K., Sarofim, M. C., Schultz, M. G., Schulz, M., Venkataraman, C., Zhang, H.,
1475 Zhang, S., Bellouin, N., Guttikunda, S. K., Hopke, P. K., Jacobson, M. Z., Kaiser,
1476 J. W., Klimont, Z., Lohmann, U., Schwarz, J. P., Shindell, D., Storelvmo, T.,
1477 Warren, S. G., and Zender, C. S.: Bounding the role of black carbon in the climate
1478 system: A scientific assessment, J. Geophys. Res.:Atmos., 118, 5380-5552,
1479 10.1002/jgrd.50171, 2013.
1480 Burgos, M. A., Andrews, E., Titos, G., Benedetti, A., Bian, H. S., Buchard, V., Curci,

G., Kipling, Z., Kirkevåg, A., Kokkola, H., Laakso, A., Letertre-Danczak, J., Lund, M. T., Matsui, H., Myhre, G., Randles, C., Schulz, M., van Noije, T., Zhang, K., Alados-Arboledas, L., Baltensperger, U., Jefferson, A., Sherman, J., Sun, J. Y., Weingartner, E., and Zieger, P.: A global model-measurement evaluation of particle light scattering coefficients at elevated relative humidity, Atmos. Chem. Phys., 20, 10231-10258, 10.5194/acp-20-10231-2020, 2020.

Che, H. Z., Qi, B., Zhao, H. J., Xia, X. G., Eck, T. F., Goloub, P., Dubovik, O., Estelles, V., Cuevas-Agulló, E., Blarel, L., Wu, Y. F., Zhu, J., Du, R. G., Wang, Y. Q., Wang, H., Gui, K., Yu, J., Zheng, Y., Sun, T. Z., Chen, Q. L., Shi, G. Y., and Zhang, X. Y.: Aerosol optical properties and direct radiative forcing based on measurements from the China Aerosol Remote Sensing Network (CARSNET) in eastern China, Atmos. Chem. Phys., 18, 405-425, 10.5194/acp-18-405-2018, 2018.

Chen, B., Song, Z., Pan, F., and Huang, Y.: Obtaining vertical distribution of PM2.5 from CALIOP data and machine learning algorithms, Sci. Total Environ., 805, 150338, 10.1016/j.scitotenv.2021.150338, 2022a.

Chen, J., Jiang, Z., Li, R., Liao, C., Miyazaki, K., and Jones, D. B. A.: Large discrepancy between observed and modeled wintertime tropospheric NO2 variabilities due to COVID-19 controls in China, Environ. Res. Lett., 17, 10.1088/1748-9326/ac4ec0, 2022b.

Chen, X., Wang, J., Xu, X. G., and Zhou, M.: Dust Aerosol Optical Centroid Height (AOCH) Over Bright Surface: First Retrieval From TROPOMI Oxygen A and B Absorption Bands, IEEE Geosci. Remote Sensing Lett., 22, 10.1109/lgrs.2025.3601046, 2025.

Chimot, J., Veefkind, J. P., Vlemmix, T., and Levelt, P. F.: Spatial distribution analysis of the OMI aerosol layer height: a pixel-by-pixel comparison to CALIOP observations, Atmos. Meas. Tech., 11, 2257-2277, 10.5194/amt-11-2257-2018, 2018.

Chinnam, N., Dey, S., Tripathi, S. N., and Sharma, M.: Dust events in Kanpur, northern

India: Chemical evidence for source and implications to radiative forcing, Geophys. Res. Lett., 33, 10.1029/2005gl025278, 2006.

Choi, M., Park, J., Sung, M., and Ying, Q.: Long-Range Transport of Secondary Inorganic Aerosol from China to South Korea, Environ. Sci. Technol. Lett., 11, 1233-1238, 10.1021/acs.estlett.4c00852, 2024.

Christensen, M. W., Jones, W. K., and Stier, P.: Aerosols enhance cloud lifetime and brightness along the stratus-to-cumulus transition, Proc. Natl. Acad. Sci. U.S.A., 117, 17591-17598, 10.1073/pnas.1921231117, 2020.

Colarco, P. R., Kahn, R. A., Remer, L. A., and Levy, R. C.: Impact of satellite viewing-swath width on global and regional aerosol optical thickness statistics and trends, Atmos. Meas. Tech., 7, 2313-2335, 10.5194/amt-7-2313-2014, 2014.

Crawford, J. H., Ahn, J. Y., Al-Saadi, J., Chang, L., Emmons, L. K., Kim, J., Lee, G., Park, J. H., Park, R. J., Woo, J. H., Song, C. K., Hong, J. H., Hong, Y. D., Lefer, B. L., Lee, M., Lee, T., Kim, S., Min, K. E., Yum, S. S., Shin, H. J., Kim, Y. W., Choi, J. S., Park, J. S., Szykman, J. J., Long, R. W., Jordan, C. E., Simpson, I. J., Fried, A., Dibb, J. E., Cho, S., and Kim, Y. P.: The Korea-United States Air Quality (KORUS-AQ) field study, Elem. Sci. Anth., 9, 10.1525/elementa.2020.00163, 2021.

Daoud, N., Eltahan, M., and Elhennawi, A.: Aerosol Optical Depth Forecast over Global Dust Belt Based on LSTM, CNN-LSTM, CONV-LSTM and FFT Algorithms, 19th International Conference on Smart Technologies (IEEE EUROCON), Lviv, UKRAINE, Jul 06-08 2021, WOS:000728121700034, 186-191, 10.1109/eurocon52738.2021.9535571, 2021.

Diner, D. J., Boland, S. W., Brauer, M., Bruegge, C., Burke, K. A., Chipman, R., Di Girolamo, L., Garay, M. J., Hasheminassab, S., Hyer, E., Jerrett, M., Jovanovic, V., Kalashnikova, O. V., Liu, Y., Lyapustin, A. I., Martin, R. V., Nastan, A., Ostro, B. D., Ritz, B., Schwartz, J., Wang, J., and Xu, F.: Advances in multiangle satellite remote sensing of speciated airborne particulate matter and association with

adverse health effects: from MISR to MAIA, J. Appl. Remote Sens, 12, 10.1117/1.Jrs.12.042603, 2018.

Ding, A. J., Wang, T., Xue, L. K., Gao, J., Stohl, A., Lei, H. C., Jin, D. Z., Ren, Y., Wang, X. Z., Wei, X. L., Qi, Y. B., Liu, J., and Zhang, X. Q.: Transport of north China air pollution by midlatitude cyclones: Case study of aircraft measurements in summer 2007 (vol 114, D08304, 2007), J. Geophys. Res.:Atmos., 114, 10.1029/2009jd012339, 2009.

Ding, S. G., Wang, J., and Xu, X. G.: Polarimetric remote sensing in oxygen A and B bands: sensitivity study and information content analysis for vertical profile of aerosols, Atmos. Meas. Tech., 9, 2077-2092, 10.5194/amt-9-2077-2016, 2016.

Dong, W., Tao, M., Xu, X., Wang, J., Wang, Y., Wang, L., Song, Y., Fan, M., and Chen, L.: Satellite Aerosol Retrieval From Multiangle Polarimetric Measurements: Information Content and Uncertainty Analysis, IEEE Trans. Geosci. Remote Sensing, 61, 1-13, 10.1109/tgrs.2023.3264554, 2023.

Du, Q., Zhao, C., Zhang, M., Dong, X., Chen, Y., Liu, Z., Hu, Z., Zhang, Q., Li, Y., Yuan, R., and Miao, S.: Modeling diurnal variation of surface PM2.5 concentrations over East China with WRF-Chem: impacts from boundary-layer mixing and anthropogenic emission, Atmos. Chem. Phys., 20, 2839-2863, 10.5194/acp-20-2839-2020, 2020.

Dubovik, O., Herman, M., Holdak, A., Lapyonok, T., Tanré, D., Deuzé, J. L., Ducos, F., Sinyuk, A., and Lopatin, A.: Statistically optimized inversion algorithm for enhanced retrieval of aerosol properties from spectral multi-angle polarimetric satellite observations, Atmos. Meas. Tech., 4, 975-1018, 10.5194/amt-4-975-2011, 2011.

Eastham, S. D. and Jacob, D. J.: Limits on the ability of global Eulerian models to resolve intercontinental transport of chemical plumes, Atmos. Chem. Phys., 17, 2543-2553, 10.5194/acp-17-2543-2017, 2017.

Fan, Y., Sun, L., Wang, Z., Pang, S., and Wei, J.: Unveiling diurnal aerosol layer height

variability from space using deep learning, ISPRS. J. Photogramm. Remote. Sens., 229, 211-222, 10.1016/j.isprsjprs.2025.08.021, 2025.

Ge, C., Wang, J., and Reid, J. S.: Mesoscale modeling of smoke transport over the Southeast Asian Maritime Continent: coupling of smoke direct radiative effect below and above the low-level clouds, Atmos. Chem. Phys., 14, 159-174, 10.5194/acp-14-159-2014, 2014.

Geer, A. J.: Learning earth system models from observations: machine learning or data assimilation?, Philos. Trans. R. Soc. A Math. Phys. Eng., 379, 10.1098/rsta.2020.0089, 2021.

Gelaro, R., McCarty, W., Suárez, M. J., Todling, R., Molod, A., Takacs, L., Randles, C. A., Darmenov, A., Bosilovich, M. G., Reichle, R., Wargan, K., Coy, L., Cullather, R., Draper, C., Akella, S., Buchard, V., Conaty, A., da Silva, A. M., Gu, W., Kim, G. K., Koster, R., Lucchesi, R., Merkova, D., Nielsen, J. E., Partyka, G., Pawson, S., Putman, W., Rienecker, M., Schubert, S. D., Sienkiewicz, M., and Zhao, B.: The Modern-Era Retrospective Analysis for Research and Applications, Version 2 (MERRA-2), J. Climate, 30, 5419-5454, 10.1175/jcli-d-16-0758.1, 2017.

Getzewich, B. J., Vaughan, M. A., Hunt, W. H., Avery, M. A., Powell, K. A., Tackett, J. L., Winker, D. M., Kar, J., Lee, K. P., and Toth, T. D.: CALIPSO lidar calibration at 532 nm: version 4 daytime algorithm, Atmos. Meas. Tech., 11, 6309-6326, 10.5194/amt-11-6309-2018, 2018.

Giglio, L., Randerson, J. T., and van der Werf, G. R.: Analysis of daily, monthly, and annual burned area using the fourth-generation global fire emissions database (GFED4), J. Geophys. Res. Biogeosci., 118, 317-328, 10.1002/jgrg.20042, 2013.

Giles, D. M., Sinyuk, A., Sorokin, M. G., Schafer, J. S., Smirnov, A., Slutsker, I., Eck, T. F., Holben, B. N., Lewis, J. R., Campbell, J. R., Welton, E. J., Korkin, S. V., and Lyapustin, A. I.: Advancements in the Aerosol Robotic Network (AERONET) Version 3 database - automated near-real-time quality control algorithm with improved cloud screening for Sun photometer aerosol optical depth (AOD)

measurements, Atmos. Meas. Tech., 12, 169-209, 10.5194/amt-12-169-2019, 2019.

Goldstein, A. H., Koven, C. D., Heald, C. L., and Fung, I. Y.: Biogenic carbon and anthropogenic pollutants combine to form a cooling haze over the southeastern United States, Proc. Natl. Acad. Sci. U.S.A., 106, 8835-8840, 10.1073/pnas.0904128106, 2009.

Grythe, H., Ström, J., Krejci, R., Quinn, P., and Stohl, A.: A review of sea-spray aerosol source functions using a large global set of sea salt aerosol concentration measurements, Atmos. Chem. Phys., 14, 1277-1297, 10.5194/acp-14-1277-2014, 2014.

Guenther, A. B., Jiang, X., Heald, C. L., Sakulyanontvittaya, T., Duhl, T., Emmons, L. K., and Wang, X.: The Model of Emissions of Gases and Aerosols from Nature version 2.1 (MEGAN2.1): an extended and updated framework for modeling biogenic emissions, Geosci. Model Dev., 5, 1471-1492, 10.5194/gmd-5-1471-2012, 2012.

Guo, J., He, J., Liu, H., Miao, Y., Liu, H., and Zhai, P.: Impact of various emission control schemes on air quality using WRF-Chem during APEC China 2014, Atmos. Environ., 140, 311-319, 10.1016/j.atmosenv.2016.05.046, 2016.

Handschuh, J., Erbertseder, T., Schaap, M., and Baier, F.: Estimating PM2.5 surface concentrations from AOD: A combination of SLSTR and MODIS, Remote. Sens. Appl., 26, 10.1016/j.rsase.2022.100716, 2022.

Henze, D. K., Hakami, A., and Seinfeld, J. H.: Development of the adjoint of GEOS-Chem, Atmos. Chem. Phys., 7, 2413-2433, 10.5194/acp-7-2413-2007, 2007.

Henze, D. K., Seinfeld, J. H., and Shindell, D. T.: Inverse modeling and mapping US air quality influences of inorganic PM2.5 precursor emissions using the adjoint of GEOS-Chem, Atmos. Chem. Phys., 9, 5877-5903, 10.5194/acp-9-5877-2009, 2009.

Hoesly, R. M., Smith, S. J., Feng, L., Klimont, Z., Janssens-Maenhout, G., Pitkanen, T., Seibert, J. J., Vu, L., Andres, R. J., Bolt, R. M., Bond, T. C., Dawidowski, L.,

Kholod, N., Kurokawa, J.-i., Li, M., Liu, L., Lu, Z., Moura, M. C. P., O'Rourke, P. R., and Zhang, Q.: Historical (1750–2014) anthropogenic emissions of reactive gases and aerosols from the Community Emissions Data System (CEDS), Geosci. Model Dev., 11, 369-408, 10.5194/gmd-11-369-2018, 2018.

Holben, B. N., Eck, T. F., Slutsker, I., Tanre, D., Buis, J. P., Setzer, A., Vermote, E., Reagan, J. A., Kaufman, Y. J., Nakajima, T., Lavenu, F., Jankowiak, I., and Smirnov, A.: AERONET - A federated instrument network and data archive for aerosol characterization, Remote Sens. Environ., 66, 1-16, 10.1016/s0034-4257(98)00031-5, 1998.

Holtslag, A. A. M., Svensson, G., Baas, P., Basu, S., Beare, B., Beljaars, A. C. M., Bosveld, F. C., Cuxart, J., Lindvall, J., Steeneveld, G. J., Tjernström, M., and Van De Wiel, B. J. H.: Stable Atmospheric Boundary Layers and Diurnal Cycles: Challenges for Weather and Climate Models, Bull. Am. Meteorol. Soc., 94, 1691-1706, 10.1175/bams-d-11-00187.1, 2013.

Hong, Y. and Di Girolamo, L.: An Overview of Aerosol Properties in Clear and Cloudy Sky Based on CALIPSO Observations, Earth Space Sci., 9, 10.1029/2022ea002287, 2022.

Hu, X. F., Waller, L. A., Lyapustin, A., Wang, Y. J., Al-Hamdan, M. Z., Crosson, W. L., Estes, M. G., Estes, S. M., Quattrochi, D. A., Puttaswamy, S. J., and Liu, Y.: Estimating ground-level PM2.5 concentrations in the Southeastern United States using MAIAC AOD retrievals and a two-stage model, Remote Sens. Environ., 140, 220-232, 10.1016/j.rse.2013.08.032, 2014.

Huang, J. T., Loría-Salazar, S., Deng, M., Lee, J., and Holmes, H. A.: Assessment of smoke plume height products derived from multisource satellite observations using lidar-derived height metrics for wildfires in the western US, Atmos. Chem. Phys., 24, 3673-3698, 10.5194/acp-24-3673-2024, 2024.

Huang, L., Jiang, J. H., Tackett, J. L., Su, H., and Fu, R.: Seasonal and diurnal variations of aerosol extinction profile and type distribution from CALIPSO 5‐year

observations, J. Geophys. Res.:Atmos., 118, 4572-4596, 10.1002/jgrd.50407, 2013.

Hunt, W. H., Winker, D. M., Vaughan, M. A., Powell, K. A., Lucker, P. L., and Weimer, C.: CALIPSO Lidar Description and Performance Assessment, J. Atmos. Oceanic Technol., 26, 1214-1228, 10.1175/2009jtecha1223.1, 2009.

Ichoku, C., Chu, D. A., Mattoo, S., Kaufman, Y. J., Remer, L. A., Tanré, D., Slutsker, I., and Holben, B. N.: A spatio-temporal approach for global validation and analysis of MODIS aerosol products, Geophys. Res. Lett., 29, 10.1029/2001gl013206, 2002.

Jiang, X., Wang, Y., Wang, L., Tao, M., Wang, J., Zhou, M., Bai, X., and Gui, L.: Characteristics of Daytime‐And‐Nighttime AOD Differences Over China: A Perspective From CALIOP Satellite Observations and GEOS‐Chem Model Simulations, J. Geophys. Res.:Atmos., 129, 10.1029/2023jd039158, 2024.

Kahn, R. A., Gaitley, B. J., Martonchik, J. V., Diner, D. J., Crean, K. A., and Holben, B.: Multiangle Imaging Spectroradiometer (MISR) global aerosol optical depth validation based on 2 years of coincident Aerosol Robotic Network (AERONET) observations - art. no. D10S04, J. Geophys. Res.:Atmos., 110, 10.1029/2004jd004706, 2005.

Kaufman, Y. J., Tanré, D., and Boucher, O.: A satellite view of aerosols in the climate system, Nature, 419, 215-223, 10.1038/nature01091, 2002.

Kim, H., Chen, X., Wang, J., Lu, Z. D., Zhou, M., Carmichael, G. R., Park, S. S., and Kim, J.: Aerosol layer height (ALH) retrievals from oxygen absorption bands: intercomparison and validation among different satellite platforms, GEMS, EPIC, and TROPOMI, Atmos. Meas. Tech., 18, 327-349, 10.5194/amt-18-327-2025, 2025.

Kim, H., Park, R. J., Hong, S. Y., Park, D. H., Kim, S. W., Oak, Y. J., Feng, X., Lin, H., and Fu, T. M.: A mixed layer height parameterization in a 3-D chemical transport model: Implications for gas and aerosol simulations, Sci. Total Environ., 955,

176838, 10.1016/j.scitotenv.2024.176838, 2024.

Kim, K.-Y.: Diurnal and seasonal variation of planetary boundary layer height over East Asia and its climatic change as seen in the ERA-5 reanalysis data, SN Appl. Sci., 4, 10.1007/s42452-021-04918-5, 2022.

Kim, M.-H., Omar, A. H., Tackett, J. L., Vaughan, M. A., Winker, D. M., Trepte, C. R., Hu, Y., Liu, Z., Poole, L. R., Pitts, M. C., Kar, J., and Magill, B. E.: The CALIPSO version 4 automated aerosol classification and lidar ratio selection algorithm, Atmos. Meas. Tech., 11, 6107-6135, 10.5194/amt-11-6107-2018, 2018.

Kim, P. S., Jacob, D. J., Fisher, J. A., Travis, K., Yu, K., Zhu, L., Yantosca, R. M., Sulprizio, M. P., Jimenez, J. L., Campuzano-Jost, P., Froyd, K. D., Liao, J., Hair, J. W., Fenn, M. A., Butler, C. F., Wagner, N. L., Gordon, T. D., Welti, A., Wennberg, P. O., Crounse, J. D., St. Clair, J. M., Teng, A. P., Millet, D. B., Schwarz, J. P., Markovic, M. Z., and Perring, A. E.: Sources, seasonality, and trends of southeast US aerosol: an integrated analysis of surface, aircraft, and satellite observations with the GEOS-Chem chemical transport model, Atmos. Chem. Phys., 15, 10411-10433, 10.5194/acp-15-10411-2015, 2015.

Koch, D. and Del Genio, A. D.: Black carbon semi-direct effects on cloud cover: review and synthesis, Atmos. Chem. Phys., 10, 7685-7696, 10.5194/acp-10-7685-2010, 2010.

Koffi, B., Schulz, M., Bréon, F. M., Griesfeller, J., Winker, D., Balkanski, Y., Bauer, S., Berntsen, T., Chin, M., Collins, W. D., Dentener, F., Diehl, T., Easter, R., Ghan, S., Ginoux, P., Gong, S., Horowitz, L. W., Iversen, T., Kirkevåg, A., Koch, D., Krol, M., Myhre, G., Stier, P., and Takemura, T.: Application of the CALIOP layer product to evaluate the vertical distribution of aerosols estimated by global models: AeroCom phase I results, J. Geophys. Res.:Atmos., 117, 10.1029/2011jd016858, 2012a.

Koffi, B., Schulz, M., Bréon, F. M., Griesfeller, J., Winker, D., Balkanski, Y., Bauer, S., Berntsen, T., Chin, M. A., Collins, W. D., Dentener, F., Diehl, T., Easter, R., Ghan,

S., Ginoux, P., Gong, S. L., Horowitz, L. W., Iversen, T., Kirkevåg, A., Koch, D., Krol, M., Myhre, G., Stier, P., and Takemura, T.: Application of the CALIOP layer product to evaluate the vertical distribution of aerosols estimated by global models: AeroCom phase I results, J. Geophys. Res.:Atmos., 117, 10.1029/2011jd016858, 2012b.

Koffi, B., Schulz, M., Breon, F. M., Dentener, F., Steensen, B. M., Griesfeller, J., Winker, D., Balkanski, Y., Bauer, S. E., Bellouin, N., Berntsen, T., Bian, H., Chin, M., Diehl, T., Easter, R., Ghan, S., Hauglustaine, D. A., Iversen, T., Kirkevag, A., Liu, X., Lohmann, U., Myhre, G., Rasch, P., Seland, O., Skeie, R. B., Steenrod, S. D., Stier, P., Tackett, J., Takemura, T., Tsigaridis, K., Vuolo, M. R., Yoon, J., and Zhang, K.: Evaluation of the aerosol vertical distribution in global aerosol models through comparison against CALIOP measurements: AeroCom phase II results, J. Geophys. Res.:Atmos., 121, 7254-7283, 10.1002/2015JD024639, 2016.

Li, T. W., Shen, H. F., Yuan, Q. Q., Zhang, X. C., and Zhang, L. P.: Estimating Ground-Level PM2.5 by Fusing Satellite and Station Observations: A Geo-Intelligent Deep Learning Approach, Geophys. Res. Lett., 44, 11985-11993, 10.1002/2017gl075710, 2017.

Li, X. N., Cheng, X., Wu, W. J., Wang, Q. H., Tong, Z. Y., Zhang, X. Q., Deng, D. H., and Li, Y. H.: Forecasting of bioaerosol concentration by a Back Propagation neural network model, Sci. Total Environ., 698, 10.1016/j.scitotenv.2019.134315, 2020.

Liang, M., Han, Z., Li, J., Sun, Y., Liang, L., and Li, Y.: Radiative effects and feedbacks of anthropogenic aerosols on boundary layer meteorology and fine particulate matter during the COVID-19 lockdown over China, Sci. Total Environ., 862, 160767, 10.1016/j.scitotenv.2022.160767, 2023.

Lin, J. T. and McElroy, M. B.: Impacts of boundary layer mixing on pollutant vertical profiles in the lower troposphere: Implications to satellite remote sensing, Atmos. Environ., 44, 1726-1739, 10.1016/j.atmosenv.2010.02.009, 2010.

Liu, J., Zheng, Y., Li, Z., Flynn, C., and Cribb, M.: Seasonal variations of aerosol optical properties, vertical distribution and associated radiative effects in the Yangtze Delta region of China, J. Geophys. Res.:Atmos., 117, 10.1029/2011jd016490, 2012.

Lu, Q., Liu, C., Zhao, D. L., Zeng, C., Li, J., Lu, C. S., Wang, J. D., and Zhu, B.: Atmospheric heating rate due to black carbon aerosols: Uncertainties and impact factors, Atmos. Res., 240, 10.1016/j.atmosres.2020.104891, 2020.

Lu, Z., Wang, J., Chen, X., Xu, X., Zhou, M., Fu, D., and Jiang, J. H.: First Retrieval of Aerosol Vertical Profile With Passive Remote Sensing: Part 1. Development of Algorithm Theoretical Basis, J. Geophys. Res.:Atmos., 130, 10.1029/2025jd044332, 2025a.

Lu, Z. D., Wang, J., Chen, X., Xu, X. G., Zhou, M., Fu, D. J., and Jiang, J. H.: First Retrieval of Aerosol Vertical Profile With Passive Remote Sensing: Part 1. Development of Algorithm Theoretical Basis, J. Geophys. Res.:Atmos., 130, 10.1029/2025jd044332, 2025b.

Lundberg, S. M. and Lee, S. I.: A Unified Approach to Interpreting Model Predictions, 31st Annual Conference on Neural Information Processing Systems (NIPS), Long Beach, CA, Dec 04-09 2017, WOS:000452649404081, 2017.

Lv, B., Hu, Y., Chang, H. H., Russell, A. G., and Bai, Y.: Improving the Accuracy of Daily PM2.5 Distributions Derived from the Fusion of Ground-Level Measurements with Aerosol Optical Depth Observations, a Case Study in North China, Environ. Sci. Technol., 50, 4752-4759, 10.1021/acs.est.5b05940, 2016.

McDuffie, E. E., Smith, S. J., O'Rourke, P., Tibrewal, K., Venkataraman, C., Marais, E. A., Zheng, B., Crippa, M., Brauer, M., and Martin, R. V.: A global anthropogenic emission inventory of atmospheric pollutants from sector- and fuel-specific sources (1970–2017): an application of the Community Emissions Data System (CEDS), Earth Syst. Sci. Data, 12, 3413-3442, 10.5194/essd-12-3413-2020, 2020.

Mehta, S. K., Ananthavel, A., Velu, V., Prabhakaran, T., Pandithurai, G., and Rao, D.

1761 N.: Characteristics of elevated aerosol layer over the Indian east coast,
1762 Kattankulathur (12.82°N, 80.04°E): A northeast monsoon region, Sci. Total
1763 Environ., 886, 10.1016/j.scitotenv.2023.163917, 2023.
1764 Mercado, L. M., Bellouin, N., Sitch, S., Boucher, O., Huntingford, C., Wild, M., and
1765 Cox, P. M.: Impact of changes in diffuse radiation on the global land carbon sink,
1766 Nature, 458, 1014-U1087, 10.1038/nature07949, 2009.
1767 Miao, S. G., Chen, F., Lemone, M. A., Tewari, M., Li, Q. C., and Wang, Y. C.: An
1768 Observational and Modeling Study of Characteristics of Urban Heat Island and
1769 Boundary Layer Structures in Beijing, J. Appl. Meteorol. Climatol., 48, 484-501,
1770 10.1175/2008jamc1909.1, 2009.
1771 Misra, A., Gaur, A., Bhattu, D., Ghosh, S., Dwivedi, A. K., Dalai, R., Paul, D., Gupta,
1772 T., Tare, V., Mishra, S. K., Singh, S., and Tripathi, S. N.: An overview of the
1773 physico-chemical characteristics of dust at Kanpur in the central Indo-Gangetic
1774 basin, Atmos. Environ., 97, 386-396, 10.1016/j.atmosenv.2014.08.043, 2014.
1775 Munroe, D. K., Wolfinbarger, S. R., Calder, C. A., Shi, T., Xiao, N., Lam, C. Q., and Li,
1776 D.: The relationships between biomass burning, land-cover/-use change, and the
1777 distribution of carbonaceous aerosols in mainland Southeast Asia: a review and
1778 synthesis, J. Land Use Sci., 3, 161-183, 10.1080/17474230802332241, 2008.
1779 Murphy, D. M., Froyd, K. D., Bian, H. S., Brock, C. A., Dibb, J. E., DiGangi, J. P.,
1780 Diskin, G., Dollner, M., Kupc, A., Scheuer, E. M., Schill, G. P., Weinzierf, B.,
1781 Williamson, C. J., and Yu, P. F.: The distribution of sea-salt aerosol in the global
1782 troposphere, Atmos. Chem. Phys., 19, 4093-4104, 10.5194/acp-19-4093-2019,
1783 2019.
1784 Myhre, G., Samset, B. H., Schulz, M., Balkanski, Y., Bauer, S., Berntsen, T. K., Bian,
1785 H., Bellouin, N., Chin, M., Diehl, T., Easter, R. C., Feichter, J., Ghan, S. J.,
1786 Hauglustaine, D., Iversen, T., Kinne, S., Kirkevåg, A., Lamarque, J. F., Lin, G.,
1787 Liu, X., Lund, M. T., Luo, G., Ma, X., van Noije, T., Penner, J. E., Rasch, P. J.,
1788 Ruiz, A., Seland, O., Skeie, R. B., Stier, P., Takemura, T., Tsigaridis, K., Wang, P.,

1789 Wang, Z., Xu, L., Yu, H., Yu, F., Yoon, J. H., Zhang, K., Zhang, H., and Zhou, C.:
1790 Radiative forcing of the direct aerosol effect from AeroCom Phase II simulations,
1791 Atmos. Chem. Phys., 13, 1853-1877, 10.5194/acp-13-1853-2013, 2013.
1792 Nanda, S., de Graaf, M., Veefkind, J. P., Sneep, M., ter Linden, M., Sun, J. Y. T., and
1793 Levelt, P. F.: A first comparison of TROPOMI aerosol layer height (ALH) to
1794 CALIOP data, Atmos. Meas. Tech., 13, 3043-3059, 10.5194/amt-13-3043-2020,
1795 2020.
1796 Nanda, S., Veefkind, J. P., de Graaf, M., Sneep, M., Stammes, P., de Haan, J. F., Sanders,
1797 A. F. J., Apituley, A., Tuinder, O., and Levelt, P. F.: A weighted least squares
1798 approach to retrieve aerosol layer height over bright surfaces applied to GOME-2
1799 measurements of the oxygen A band for forest fire cases over Europe, Atmos.
1800 Meas. Tech., 11, 3263-3280, 10.5194/amt-11-3263-2018, 2018.
1801 Nguyen, D.-L., Czech, H., Pieber, S. M., Schnelle-Kreis, J., Steinbacher, M., Orasche,
1802 J., Henne, S., Popovicheva, O. B., Abbaszade, G., Engling, G., Bukowiecki, N.,
1803 Nguyen, N.-A., Nguyen, X.-A., and Zimmermann, R.: Carbonaceous aerosol
1804 composition in air masses influenced by large-scale biomass burning: a case study
1805 in northwestern Vietnam, Atmos. Chem. Phys., 21, 8293-8312, 10.5194/acp-21-
1806 8293-2021, 2021.
1807 Pashayi, M., Satari, M., and Shahraki, M. M.: Multi-layer retrieval of aerosol optical
1808 depth in the troposphere using SEVIRI data: a case study of the European
1809 continent, Atmos. Meas. Tech., 18, 1415-1439, 10.5194/amt-18-1415-2025, 2025.
1810 Paugam, R., Wooster, M., Freitas, S., and Martin, M. V.: A review of approaches to
1811 estimate wildfire plume injection height within large-scale atmospheric chemical
1812 transport models, Atmos. Chem. Phys., 16, 907-925, 10.5194/acp-16-907-2016,
1813 2016.
1814 Rastigejev, Y., Park, R., Brenner, M. P., and Jacob, D. J.: Resolving intercontinental
1815 pollution plumes in global models of atmospheric transport, J. Geophys.
1816 Res.:Atmos., 115, 10.1029/2009jd012568, 2010.

1817 Reichstein, M., Camps-Valls, G., Stevens, B., Jung, M., Denzler, J., Carvalhais, N., and
1818 Prabhat: Deep learning and process understanding for data-driven Earth system
1819 science, Nature, 566, 195-204, 10.1038/s41586-019-0912-1, 2019.
1820 Samset, B. H., Myhre, G., Schulz, M., Balkanski, Y., Bauer, S., Berntsen, T. K., Bian,
1821 H., Bellouin, N., Diehl, T., Easter, R. C., Ghan, S. J., Iversen, T., Kinne, S.,
1822 Kirkevåg, A., Lamarque, J. F., Lin, G., Liu, X., Penner, J. E., Seland, O., Skeie, R.
1823 B., Stier, P., Takemura, T., Tsigaridis, K., and Zhang, K.: Black carbon vertical
1824 profiles strongly affect its radiative forcing uncertainty, Atmos. Chem. Phys., 13,
1825 2423-2434, 10.5194/acp-13-2423-2013, 2013.
1826 Sanders, A. F. J., de Haan, J. F., Sneep, M., Apituley, A., Stammes, P., Vieitez, M. O.,
1827 Tilstra, L. G., Tuinder, O. N. E., Koning, C. E., and Veefkind, J. P.: Evaluation of
1828 the operational Aerosol Layer Height retrieval algorithm for Sentinel-5 Precursor:
1829 application to O2 A band observations from GOME-2A, Atmos. Meas. Tech., 8,
1830 4947-4977, 10.5194/amt-8-4947-2015, 2015.
1831 Sekiyama, T. T., Tanaka, T. Y., Shimizu, A., and Miyoshi, T.: Data assimilation of
1832 CALIPSO aerosol observations, Atmos. Chem. Phys., 10, 39-49, 10.5194/acp-10-
1833 39-2010, 2010.
1834 Shao, Y. P., Wyrwoll, K. H., Chappell, A., Huang, J. P., Lin, Z. H., McTainsh, G. H.,
1835 Mikami, M., Tanaka, T. Y., Wang, X. L., and Yoon, S.: Dust cycle: An emerging
1836 core theme in Earth system science, Aeolian Res., 2, 181-204,
1837 10.1016/j.aeolia.2011.02.001, 2011.
1838 Shi, S. S., Zhu, B., Lu, W., Yan, S. Q., Fang, C. W., Liu, X. H., Liu, D. Y., and Liu, C.:
1839 Estimation of radiative forcing and heating rate based on vertical observation of
1840 black carbon in Nanjing, China, Sci. Total Environ., 756,
1841 10.1016/j.scitotenv.2020.144135, 2021.
1842 Shrikumar, A., Greenside, P., and Kundaje, A.: Learning Important Features Through
1843 Propagating Activation Differences, 34th International Conference on Machine
1844 Learning, Sydney, AUSTRALIA, Aug 06-11 2017, WOS:000683309503025,

2017.

Singh, R. P., Dey, S., Tripathi, S. N., Tare, V., and Holben, B.: Variability of aerosol parameters over Kanpur, northern India, J. Geophys. Res.:Atmos., 109, 10.1029/2004jd004966, 2004.

Song, X. W., Wu, D., Jin, L. N., Xu, Y. Y., Chen, X., and Li, Q.: Aerosol Toxicokinetics: A Framework for Unraveling Toxicological Dynamics from Air to the Body, Environ. Sci. Technol., 59, 6379-6386, 10.1021/acs.est.5c00751, 2025.

Stier, P., Seinfeld, J. H., Kinne, S., and Boucher, O.: Aerosol absorption and radiative forcing, Atmos. Chem. Phys., 7, 5237-5261, 10.5194/acp-7-5237-2007, 2007.

Tsay, S.-C., Hsu, N. C., Lau, W. K. M., Li, C., Gabriel, P. M., Ji, Q., Holben, B. N., Judd Welton, E., Nguyen, A. X., Janjai, S., Lin, N.-H., Reid, J. S., Boonjawat, J., Howell, S. G., Huebert, B. J., Fu, J. S., Hansell, R. A., Sayer, A. M., Gautam, R., Wang, S.-H., Goodloe, C. S., Miko, L. R., Shu, P. K., Loftus, A. M., Huang, J., Kim, J. Y., Jeong, M.-J., and Pantina, P.: From BASE-ASIA toward 7-SEAS: A satellite-surface perspective of boreal spring biomass-burning aerosols and clouds in Southeast Asia, Atmos. Environ., 78, 20-34, 10.1016/j.atmosenv.2012.12.013, 2013.

Uno, I., Eguchi, K., Yumimoto, K., Takemura, T., Shimizu, A., Uematsu, M., Liu, Z. Y., Wang, Z. F., Hara, Y., and Sugimoto, N.: Asian dust transported one full circuit around the globe, Nat. Geosci., 2, 557-560, 10.1038/ngeo583, 2009.

Val Martin, M., Heald, C. L., Ford, B., Prenni, A. J., and Wiedinmyer, C.: A decadal satellite analysis of the origins and impacts of smoke in Colorado, Atmos. Chem. Phys., 13, 7429-7439, 10.5194/acp-13-7429-2013, 2013.

Vaswani, A., Shazeer, N., Parmar, N., Uszkoreit, J., Jones, L., Gomez, A. N., Kaiser, L., and Polosukhin, I.: Attention Is All You Need, 31st Annual Conference on Neural Information Processing Systems (NIPS), Long Beach, CA, Dec 04-09 2017, WOS:000452649406008, 2017.

Vernier, J. P., Thomason, L. W., Pommereau, J. P., Bourassa, A., Pelon, J., Garnier, A.,

Hauchecorne, A., Blanot, L., Trepte, C., Degenstein, D., and Vargas, F.: Major influence of tropical volcanic eruptions on the stratospheric aerosol layer during the last decade, Geophys. Res. Lett., 38, n/a-n/a, 10.1029/2011gl047563, 2011.

Wang, J., Park, S., Zeng, J., Ge, C., Yang, K., Carn, S., Krotkov, N., and Omar, A. H.: Modeling of 2008 Kasatochi volcanic sulfate direct radiative forcing: assimilation of OMI SO2 plume height data and comparison with MODIS and CALIOP observations, Atmos. Chem. Phys., 13, 1895-1912, 10.5194/acp-13-1895-2013, 2013.

Wang, L., Lyu, B., and Bai, Y.: Global aerosol vertical structure analysis by clustering gridded CALIOP aerosol profiles with fuzzy k-means, Sci. Total Environ., 761, 144076, 10.1016/j.scitotenv.2020.144076, 2021a.

Wang, Q., Zhou, C., Zhuge, X. Y., Liu, C., Weng, F. Z., and Wang, M. H.: Retrieval of cloud properties from thermal infrared radiometry using convolutional neural network, Remote Sens. Environ., 278, 10.1016/j.rse.2022.113079, 2022.

Wang, Q. Q., Jacob, D. J., Spackman, J. R., Perring, A. E., Schwarz, J. P., Moteki, N., Marais, E. A., Ge, C., Wang, J., and Barrett, S. R. H.: Global budget and radiative forcing of black carbon aerosol: Constraints from pole-to-pole (HIPPO) observations across the Pacific, J. Geophys. Res.:Atmos., 119, 195-206, 10.1002/2013jd020824, 2014.

Wang, Y., Wang, J., Xu, X. G., Henze, D. K., Qu, Z., and Yang, K.: Inverse modeling of SO2 and NOx emissions over China using multisensor satellite data - Part 1: Formulation and sensitivity analysis, Atmos. Chem. Phys., 20, 6631-6650, 10.5194/acp-20-6631-2020, 2020a.

Wang, Y., Wang, J., Zhou, M., Henze, D. K., Ge, C., and Wang, W.: Inverse modeling of SO2 and NOx emissions over China using multisensor satellite data - Part 2: Downscaling techniques for air quality analysis and forecasts, Atmos. Chem. Phys., 20, 6651-6670, 10.5194/acp-20-6651-2020, 2020b.

Wang, Y., Bagya Ramesh, C., Giangrande, S. E., Fast, J., Gong, X., Zhang, J., Tolga

Odabasi, A., Oliveira, M. V. B., Matthews, A., Mei, F., Shilling, J. E., Tomlinson, J., Wang, D., and Wang, J.: Examining the vertical heterogeneity of aerosols over the Southern Great Plains, Atmos. Chem. Phys., 23, 15671-15691, 10.5194/acp-23-15671-2023, 2023.

Wang, Y. L., Huang, R., Song, S. J., Huang, Z. Y., and Huang, G.: Not All Images are Worth 16x16 Words: Dynamic Transformers for Efficient Image Recognition, 35th Annual Conference on Neural Information Processing Systems (NeurIPS), null, ELECTR NETWORK, Dec 06-14 2021, WOS:000922928400032, 2021.

Wei, J., Li, Z., Guo, J., Sun, L., Huang, W., Xue, W., Fan, T., and Cribb, M.: Satellite-Derived 1-km-Resolution PM1 Concentrations from 2014 to 2018 across China, Environ. Sci. Technol., 53, 13265-13274, 10.1021/acs.est.9b03258, 2019.

Weinzierl, B., Ansmann, A., Prospero, J. M., Althausen, D., Benker, N., Chouza, F., Dollner, M., Farrell, D., Fomba, W. K., Freudenthaler, V., Gasteiger, J., Gross, S., Haarig, M., Heinold, B., Kandler, K., Kristensen, T. B., Mayol-Bracero, O. L., Müller, T., Reitebuch, O., Sauer, D., Schäfler, A., Schepanski, K., Spanu, A., Tegen, I., Toledano, C., and Walser, A.: The Saharan Aerosol Long-Range Transport and Aerosol–Cloud-Interaction Experiment: Overview and Selected Highlights, Bull. Am. Meteorol. Soc., 98, 1427-1451, 10.1175/bams-d-15-00142.1, 2017.

Wilcox, E. M.: Direct and semi-direct radiative forcing of smoke aerosols over clouds, Atmos. Chem. Phys., 12, 139-149, 10.5194/acp-12-139-2012, 2012.

Winker, D. M., Tackett, J. L., Getzewich, B. J., Liu, Z., Vaughan, M. A., and Rogers, R. R.: The global 3-D distribution of tropospheric aerosols as characterized by CALIOP, Atmos. Chem. Phys., 13, 3345-3361, 10.5194/acp-13-3345-2013, 2013.

Winker, D. M., Vaughan, M. A., Omar, A., Hu, Y. X., Powell, K. A., Liu, Z. Y., Hunt, W. H., and Young, S. A.: Overview of the CALIPSO Mission and CALIOP Data Processing Algorithms, J. Atmos. Oceanic Technol., 26, 2310-2323, 10.1175/2009jtecha1281.1, 2009.

Winker, D. M., Pelon, J., Coakley, J. A., Ackerman, S. A., Charlson, R. J., Colarco, P.

R., Flamant, P., Fu, Q., Hoff, R. M., Kittaka, C., Kubar, T. L., Le Treut, H., McCormick, M. P., Mégie, G., Poole, L., Powell, K., Trepte, C., Vaughan, M. A., and Wielicki, B. A.: The CALIPSO Mission: A Global 3D View of Aerosols and Clouds, Bull. Am. Meteorol. Soc., 91, 1211-1229, 10.1175/2010bams3009.1, 2010.

Xing, J., Zheng, S. X., Li, S. W., Huang, L., Wang, X. C., Wang, S. X., Liu, C., Jang, C., Zhu, Y., Zhang, J., Bian, J., Liu, T. Y., Hao, J. M., and Kelly, J. T.: Mimicking atmospheric photochemical modeling with a deep neural network, Atmos. Res., 265, 10.1016/j.atmosres.2021.105919, 2022.

Xiong, J., Wang, Y., Tao, M., Dong, W., Zhou, L., and Wang, L.: Vertical structure of the aerosols in the troposphere over the North China Plain: An analysis based on observations and simulations from 2007 to 2022, Atmos. Res., 10.1016/j.atmosres.2025.108348, 2025.

Xu, Y., Ramanathan, V., and Washington, W. M.: Observed high-altitude warming and snow cover retreat over Tibet and the Himalayas enhanced by black carbon aerosols, Atmos. Chem. Phys., 16, 1303-1315, 10.5194/acp-16-1303-2016, 2016.

Yorks, J. E., Wang, J., McGill, M. J., Follette-Cook, M., Nowottnick, E. P., Reid, J. S., Colarco, P. R., Zhang, J., Kalashnikova, O., Yu, H., Marenco, F., Santanello, J. A., Weckwerth, T. M., Li, Z., Campbell, J. R., Yang, P., Diao, M., Noel, V., Meyer, K. G., Carr, J. L., Garay, M., Christian, K., Bennedetti, A., Ring, A. M., Crawford, A., Pavolonis, M. J., Aquila, V., Kim, J., and Kondragunta, S.: A SmallSat Concept to Resolve Diurnal and Vertical Variations of Aerosols, Clouds, and Boundary Layer Height, Bull. Am. Meteorol. Soc., 104, E815-E836, 10.1175/bams-d-21-0179.1, 2023.

Zarzycki, C. M. and Bond, T. C.: How much can the vertical distribution of black carbon affect its global direct radiative forcing?, Geophys. Res. Lett., 37, 10.1029/2010gl044555, 2010.

Zeng, Y., Wang, M., Zhao, C., Chen, S., Liu, Z., Huang, X., and Gao, Y.: WRF-Chem v3.9 simulations of the East Asian dust storm in May 2017: modeling sensitivities

to dust emission and dry deposition schemes, Geosci. Model Dev.s, 13, 2125-2147, 10.5194/gmd-13-2125-2020, 2020.

Zhai, S. X., Jacob, D. J., Brewer, J. F., Li, K., Moch, J. M., Kim, J., Lee, S., Lim, H., Lee, H. C., Kuk, S. K., Park, R. J., Jeong, J., Wang, X., Liu, P. F., Luo, G., Yu, F. Q., Meng, J., Martin, R., Travis, K. R., Hair, J. W., Anderson, B. E., Dibb, J. E., Jimenez, J. L., Campuzano-Jost, P., Nault, B. A., Woo, J. H., Kim, Y., Zhang, Q., and Liao, H.: Relating geostationary satellite measurements of aerosol optical depth (AOD) over East Asia to fine particulate matter (PM2.5): insights from the KORUS-AQ aircraft campaign and GEOS-Chem model simulations, Atmos. Chem. Phys., 21, 16775-16791, 10.5194/acp-21-16775-2021, 2021.

Zhang, J. L., Campbell, J. R., Reid, J. S., Westphal, D. L., Baker, N. L., Campbell, W. F., and Hyer, E. J.: Evaluating the impact of assimilating CALIOP-derived aerosol extinction profiles on a global mass transport model, Geophys. Res. Lett., 38, 10.1029/2011gl047737, 2011.

Zhao, B., Wang, Y., Gu, Y., Liou, K.-N., Jiang, J. H., Fan, J., Liu, X., Huang, L., and Yung, Y. L.: Ice nucleation by aerosols from anthropogenic pollution, Nat. Geosci., 12, 602-607, 10.1038/s41561-019-0389-4, 2019.

Zhen, Y., Yang, X., Tang, H., Shi, H., and Liu, Z.: CALIPSO-based aerosol extinction profile estimation from MODIS and MERRA-2 data using a hybrid model of Transformer and CNN, Sci. Total Environ., 954, 10.1016/j.scitotenv.2024.176423, 2024.

Zhu, H. H., Martin, R. V., van Donkelaar, A., Hammer, M. S., Li, C., Meng, J., Oxford, C. R., Liu, X., Li, Y. S., Zhang, D. D., Singh, I., and Lyapustin, A.: Importance of aerosol composition and aerosol vertical profiles in global spatial variation in the relationship between PM2.5 and aerosol optical depth, Atmos. Chem. Phys., 24, 11565-11584, 10.5194/acp-24-11565-2024, 2024.

1983 Table 1. Experimental design based on the Leave-One-Year-Out cross-validation
1984 strategy.

Experiment ID	Training & Validation Data	Test Data	Evaluation Objective
Exp-2017	Years 2018, 2019	Year 2017	Hindcasting
Exp-2018	Years 2017, 2019	Year 2018	Temporal Interpolation
Exp-2019	Years 2017, 2018	Year 2019	Forecasting

1985

Table 2. Quantitative evaluation of the physics-informed Transformer model's predictive performance for AEC simulation biases over EA across independent test years based on the Leave-One-Year-Out strategy.

Experiment ID	R (Test)	MAE (Test)	RMSE (Test)
Exp-2017	0.666	0.014	0.039
Exp-2018	0.659	0.014	0.039
Exp-2019	0.651	0.015	0.041
Average	0.659	0.014	0.040

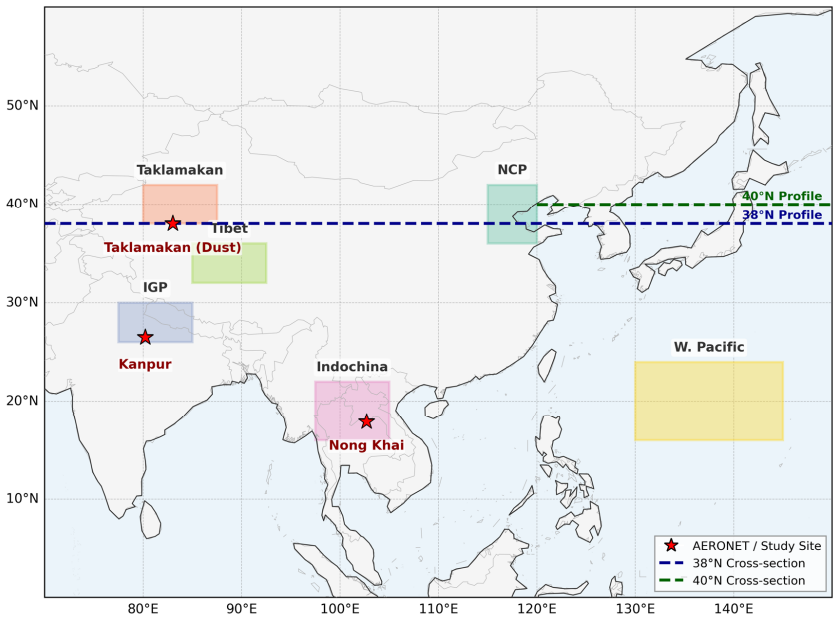

Figure 1. Map of the study domain covering East and South Asia (0°-60°N, 70°-150°E). The colored rectangles delimitate the six regions of interest selected for regional analysis. The dashed lines represent the latitudinal transects at 38°N (blue) and 40°N (green) used for vertical profile cross-section analysis. Red stars indicate the specific study sites selected to represent distinct aerosol regimes: the Kanpur and Nong Khai sites are AERONET ground-based stations selected to represent regions dominated by anthropogenic pollution and biomass burning, respectively; the Taklamakan site marks a reference location selected to investigate the characteristics of natural mineral dust.

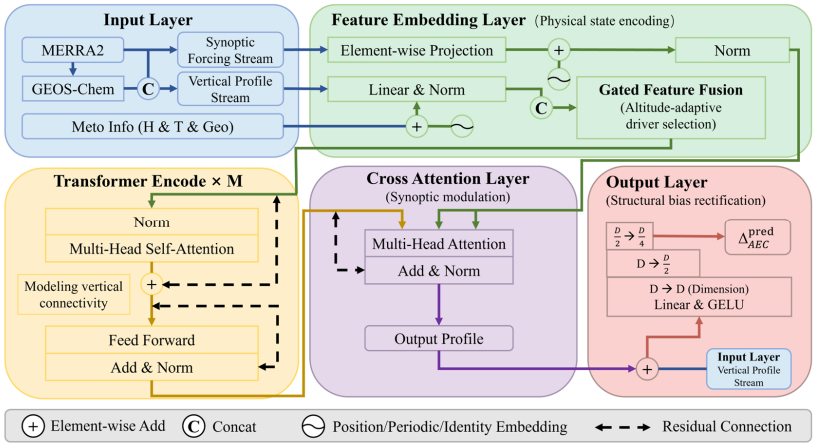

Figure 2. Architecture of the physics-informed Transformer framework. The Feature Embedding Layer integrates the VPS and SFS into unified, high-dimensional physical states. Gated Feature Fusion resolves atmospheric stratification by dynamically prioritizing altitude-dependent drivers. The Transformer Encoder stack models vertical connectivity, simulating exchange processes like turbulent mixing to ensure profile coherence. The Cross-Attention Layer retrieval synoptic constraints to modulate AEC corrections based on the meteorological background. The Output Layer performs residual bias rectification, anchoring the prediction to the initial physicochemical profiles to accurately quantify systematic simulation biases while filtering redundant noise.~~The overall architecture of the physics-informed Transformer model. The network leverages Gated Feature Fusion and Cross-Attention mechanisms within a residual learning framework to correct AEPs.~~

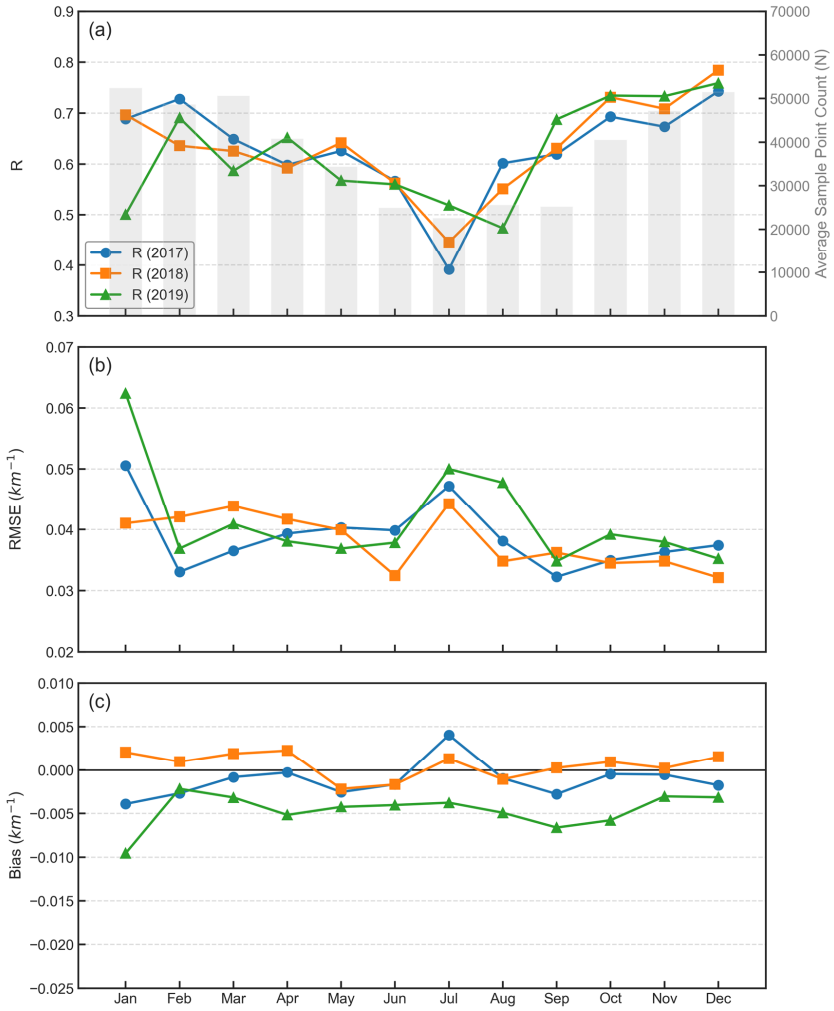

Figure 3. Monthly variations of statistical metrics evaluating the physics-informed Transformer model's predictive performance ~~for the AEC simulation bias~~ over EA across the three test years (2017, 2018, and 2019). The panels display the time series of R between the AEC bias predicted by the model and that simulated by GEOS-Chem (a)~~-~~, along with the multi-year average monthly sample size (N, gray bars), RMSE (b), and mean bias (c).

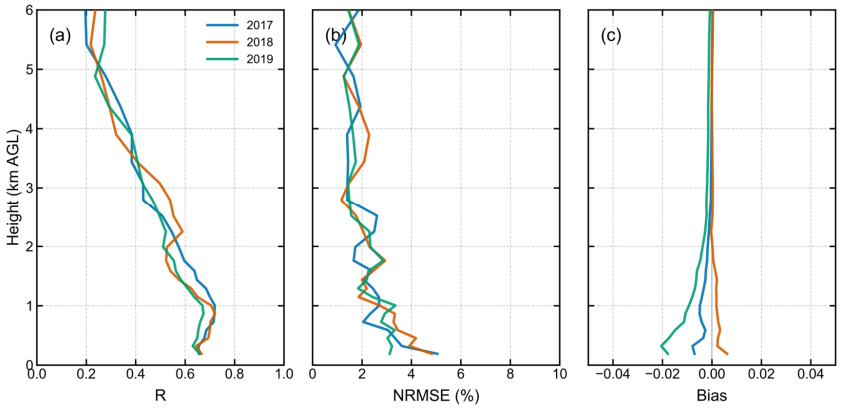

Figure 4. Vertical profiles of the physics-informed Transformer model's predictive performance for AEC simulation bias over EA across three independent test years (2017, 2018, and 2019). The panels show the height-resolved R (a), NRMSE (b), and mean bias (c). The performance is evaluated against CALIOP observations from the surface up to 6 km AGL.

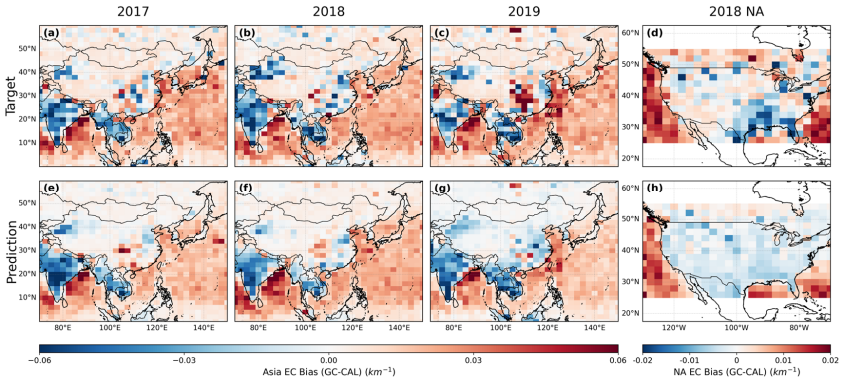

Figure 5. Spatial comparison of the vertically averaged (0–6 km AGL) AEC simulation bias over EA and NA. The top row (a–d) represents the Target systematic bias. The bottom row (e–h) displays the corresponding bias Predicted by the physics-informed Transformer model. Columns 1–3 show results for the independent test years (2017, 2018, 2019) over the primary EA domain (a–c, e–g). Column 4 presents the generalization test over the NA domain for 2018 (d, h), where the model trained on EA data is directly applied to predict biases in an unseen continent.

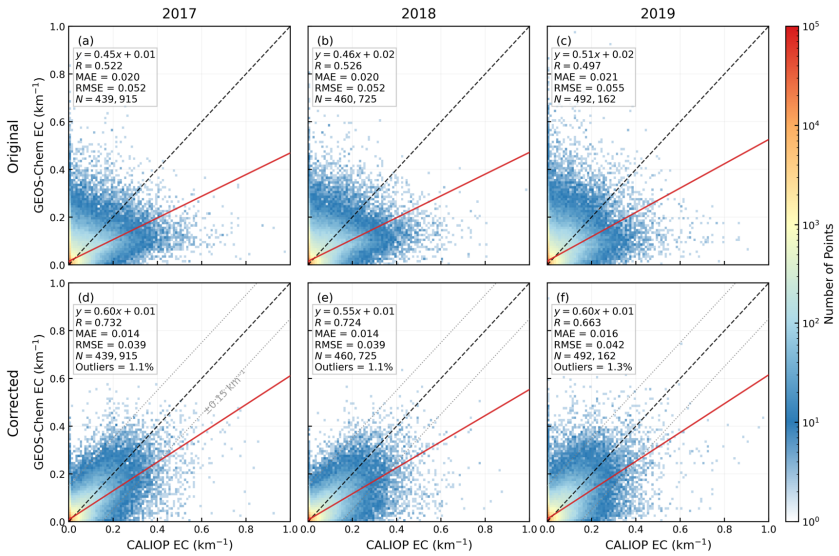

Figure 6. Density scatter plots comparing the simulated AEC against CALIOP observations over EA for the three test years: 2017 (a, d), 2018 (b, e), and 2019 (c, f). The top row (a, b, c) displays the validation results for the original GEOS-Chem simulation, while the bottom row (d, e, f) shows the results after correction by the physics-informed Transformer model. The dashed gray lines in the bottom panels (d–f) delineate the $\pm 0.15\ km^{-1}$ error envelope, with the corresponding percentage of outliers (points falling outside this envelope) indicated in the statistical boxes.

设置了格式：上标

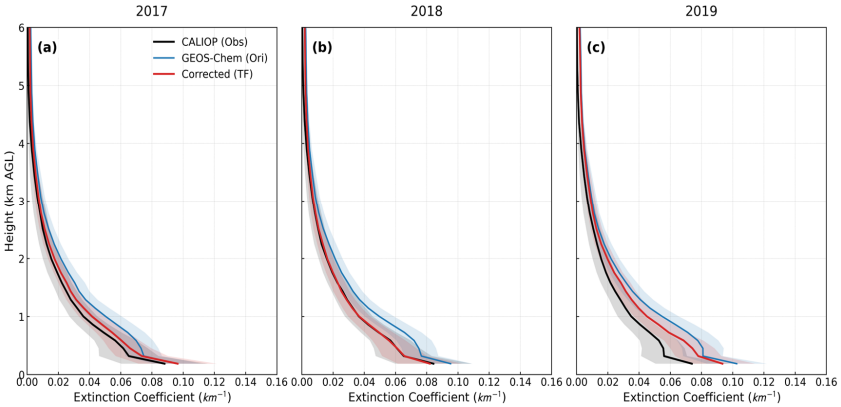

Figure 7. Annual mean vertical profiles of AEC for the three test years (2017–2019). The profiles are averaged over the entire study domain (EA). The shaded areas indicate the standard deviation ($\pm 0.5\sigma$) of the vertical distribution, representing the spatial and temporal variability.

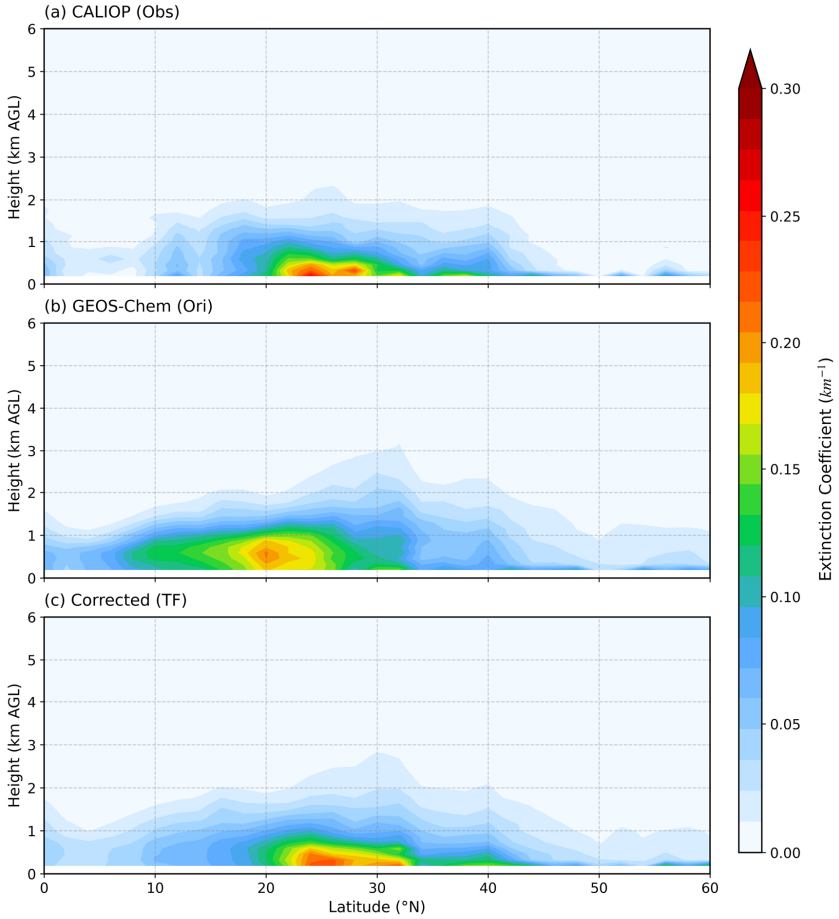

Figure 8. Zonal mean vertical distributions of AEC averaged over the longitude range (70°E–150°E) for the test year 2019. The panels display the latitude-altitude cross-sections for CALIOP observations (a), original GEOS-Chem simulations (b), and the corrected GC-TF results (c).

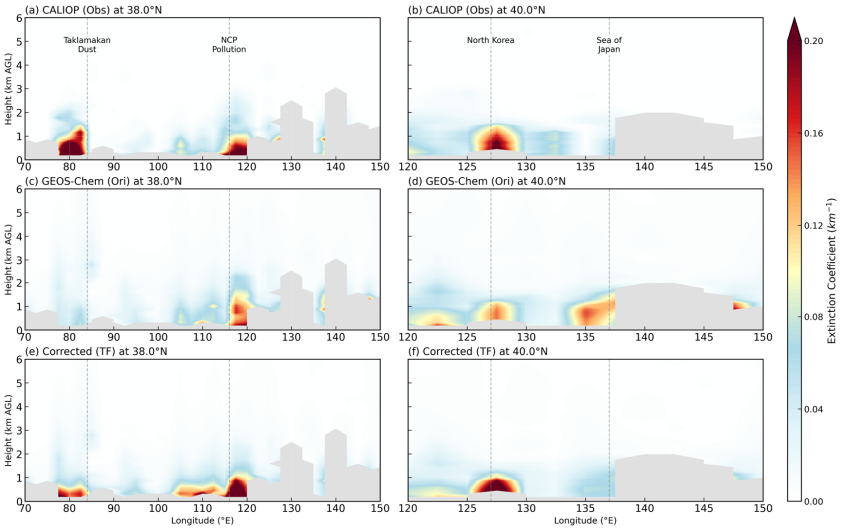

Figure 9. Longitudinal vertical cross-sections of annual mean AEC along two selected latitudes for the test year 2019. The left column displays the profiles at 38.0°N, highlighting the Taklamakan Desert and the NCP. The right column displays the profiles at 40.0°N, capturing the aerosol transport over the Korean Peninsula and the Sea of Japan. Panels show CALIOP observations (a, b), original GEOS-Chem simulations (c, d), and the corrected GC-TF results (e, f). The vertical dashed lines mark the approximate locations of key geographical features. Gray areas indicate missing data.

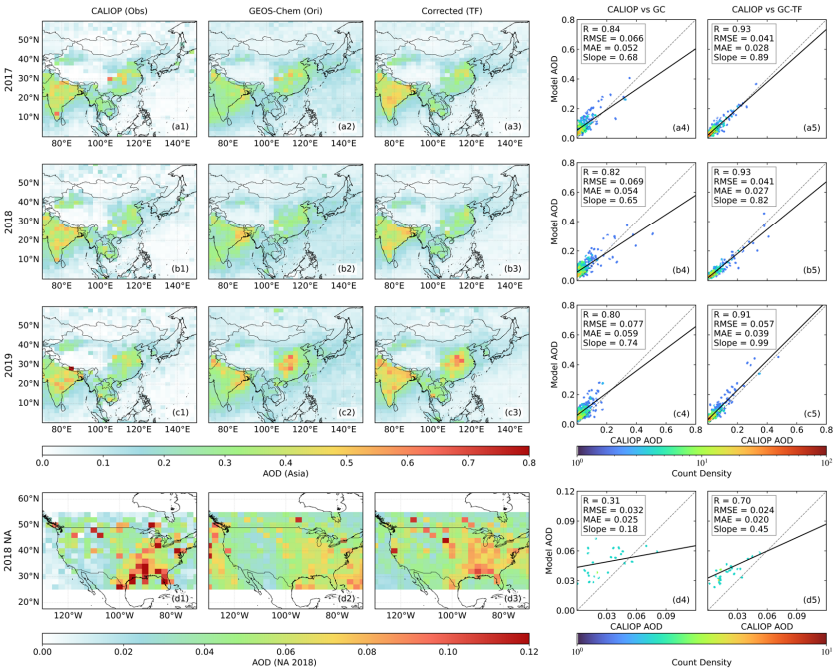

Figure 10. Spatial distributions and statistical evaluations of the annual mean AOD derived from CALIOP observations, GEOS-Chem simulations, and the GC-TF model corrections. Results for the EA domain during the test years 2017 (a), 2018 (b), and 2019 (c), respectively. Columns 1–3 display the spatial patterns of AOD from CALIOP, the original GEOS-Chem (Ori), and the corrected GC-TF results (TF). Columns 4–5 show the corresponding density scatter plots comparing the model predictions (y-axis) against CALIOP observations (x-axis). Generalization test over the NA domain for the year 2018 (d).

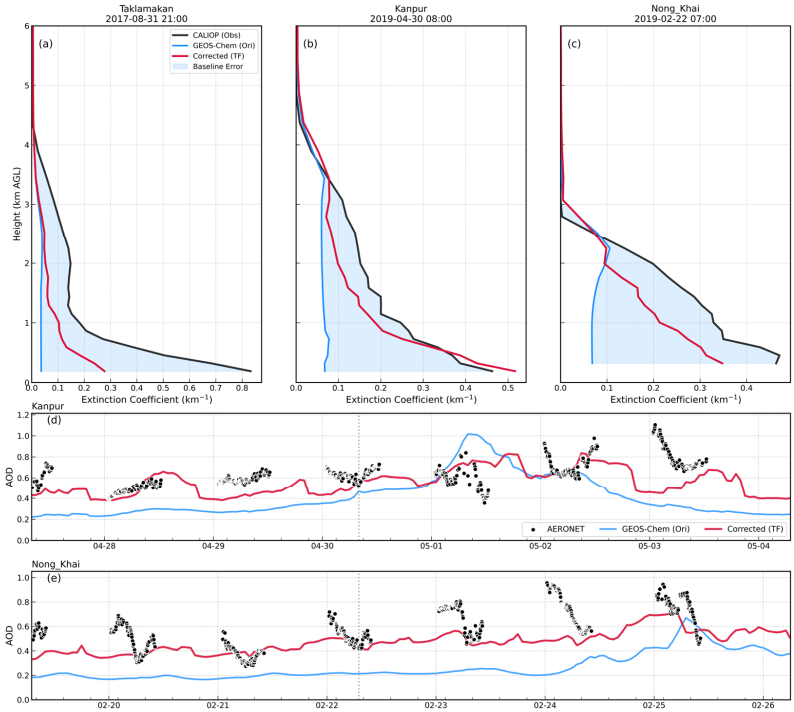

Figure 11. Composite analysis of aerosol vertical structures and temporal evolution during selected pollution episodes. Vertical profiles of AEC at three representative sites: Taklamakan (Dust, a), Kanpur (Anthropogenic Pollution, b), and Nong Khai (Biomass Burning, c). Time series of AOD at the Kanpur (d) and Nong Khai (e) AERONET sites during the corresponding pollution events. The vertical dotted lines mark the CALIOP overpass times (UTC) shown in the top panels.

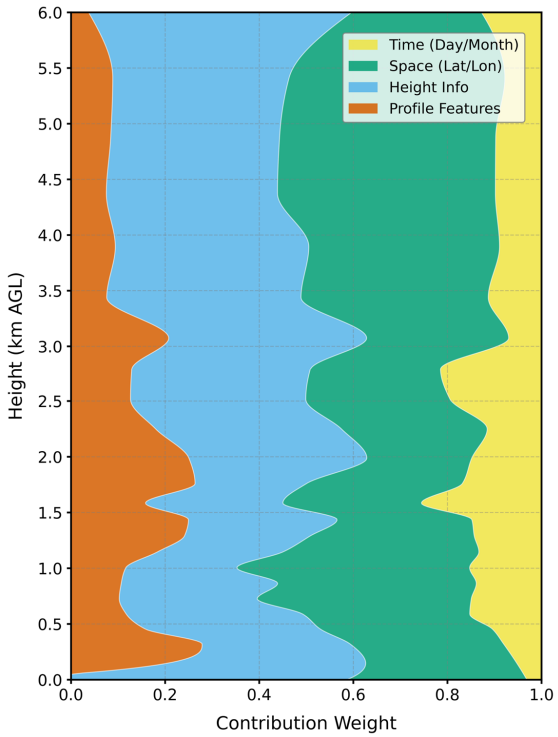

Figure 12. Altitude-dependent prioritization of information within the VPS. The stacked plot displays the learnable contribution weights for the four VPS sub-components—baseline physicochemical profiles, height information, spatial coordinates, and temporal indices—as determined by the gated feature fusion mechanism. This analysis visualizes how the model's internal decision-making adapts to different atmospheric stratifications~~Vertically resolved feature importance analysis. The stacked plot displays the altitude-dependent contribution weights of the four input feature groups (Profile Features, Height Info, Space, and Time) learned by the model's Gated Fusion mechanism~~.

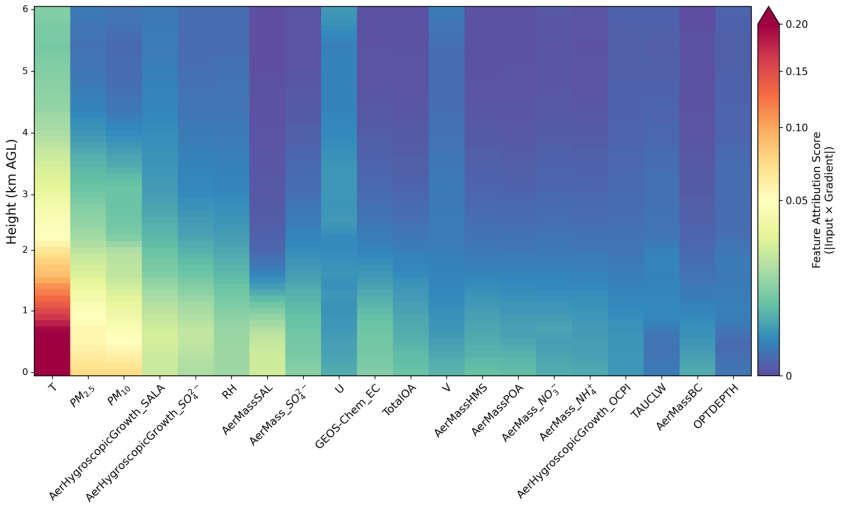

Figure 13. Vertical distribution of cross-attention weights for synoptic forcing variables. The heatmap characterizes the interaction strength between the SFS and the VPS. It reveals how specific variables within the SFS (sorted by total contribution from left to right) modulate AEC bias corrections at different altitude levels~~Vertical distribution of feature attribution scores for the top-20 profile variables, calculated using the Integrated Gradients method. The heatmap displays the contribution strength of each variable to the model's prediction at different altitude levels. The variables are sorted by their total contribution~~.

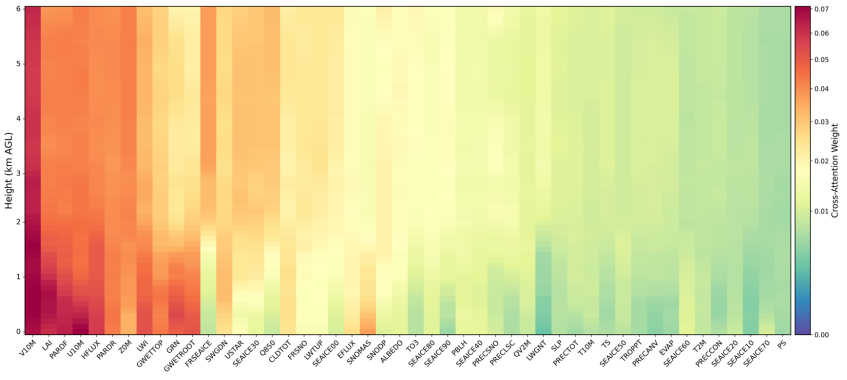

Figure 14. Vertical distribution of the attention weights for global variables learned by the Cross-Attention module. The heatmap displays the interaction strength between the ~~Vertical Profile Stream~~VPS and the ~~Global Context Stream~~SFS. The variables are sorted by their total contribution from left to right.

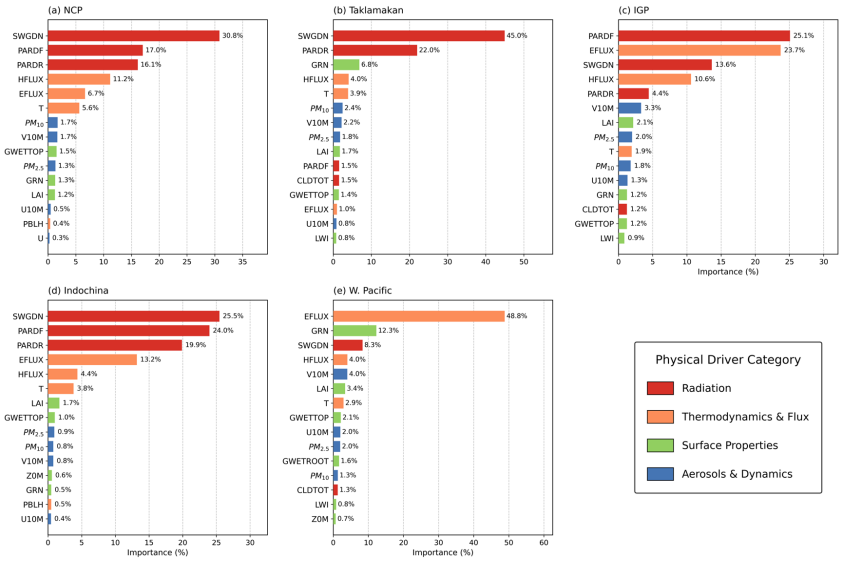

Figure 15. Regional variability in feature importance drivers identified by SHAP analysis for the test year 2019. The panels display the top 15 most influential features for predicting AEC simulation biases in five representative regions: NCP (a), Taklamakan Desert (b), IGP (c), Indochina (d), and Western Pacific (e).

Supporting Information for Correcting Aerosol Extinction Coefficient Vertical Structure Biases in GEOS-Chem via a Physics-Informed Transformer with Physical Mechanism Diagnosis

Jiajun Xiong[1], Yi Wang[1], Jun Wang[2,3], Yanyu Wang[4], Meng Zhou[5,6], Minghui Tao[1], Wenhui Dong[1], Jhoon Kim[7], Lunche Wang[1]

[1]Hubei Key Laboratory of Regional Ecology and Environmental Change, School of Geography and Information Engineering, China University of Geosciences, Wuhan, 430074, China

[2]Department of Chemical and Biochemical Engineering, The University of Iowa, Iowa City, IA 52242, USA

[3]Center for Global and Regional Environmental Research, The University of Iowa, Iowa City, IA 52242, USA

[4]State Environmental Protection Key Laboratory of Formation and Prevention of Urban Air Pollution Complex, Shanghai Academy of Environmental Sciences, Shanghai 200233, China

[5]Goddard Earth Sciences Technology and Research, University of Maryland, Baltimore County, MA 21250, USA

[6]NASA/Goddard Space Flight Center, Global Modeling and Assimilation Office, Greenbelt, MD 20771, USA

[7]Department of Atmospheric Sciences, Yonsei University, Seoul, 03722, South Korea

Corresponding author: Yi Wang (wangyi34@cug.edu.cn)

S1. CALIOP Quality Control

To ensure the reliability of the observational target, we implement a rigorous, tiered quality control strategy for the CALIOP Level 2 aerosol profile data. First, to minimize cloud contamination, profiles with a Cloud Layer Fraction (CLF) exceeding 2.0 were excluded. We further refined this dataset by applying strict thresholds to the Cloud Aerosol Discrimination (CAD) score, retaining only retrievals with high confidence (CAD score between -100 and -20). The Extinction QC flag was used to filter for algorithmically stable solutions (unconstrained or constrained), rejecting profiles with divergent retrieval errors. Adjustments to lidar ratios or opaque layer identifications were permitted only when necessary for algorithm convergence. A final multi-step refinement was applied to the vertical profiles: (1) profiles were discarded if the extinction uncertainty exceeded 99.9 km^{-1} at any lower-altitude layer; (2) physically unrealistic extinction coefficients greater than 2 km^{-1} were flagged and removed; and (3) to mitigate surface contamination artifacts, data within 180 m of the terrain were excluded. Observations classified as "clear air" were assigned an extinction coefficient of 0 km^{-1}, with the exception of the lowest 180 m AGL, which was masked to avoid surface return interference. Additional safeguards included the removal of high-altitude data (>4 km) near 0°C ice clouds and the exclusion of spatially isolated aerosol signals (horizontal resolution < 80 km).

S2. AERONET AOD Interpolation

Standard AERONET sun photometers do not measure AOD directly at 532 nm, the operating wavelength of the CALIOP lidar and our GEOS-Chem configuration. To enable direct comparison, we interpolated the AOD to 532 nm using the Ångström exponent (α) derived from measurements at adjacent wavelengths (typically 500 nm and 675 nm, or 440 nm/870 nm if necessary). The interpolation follows the power-law relationship:

$$\tau_{532} = \tau_{\lambda_1} \times \left(\frac{532}{\lambda_1}\right)^{-\alpha}$$

$$\alpha = -\frac{\ln\left(\frac{\tau_{\lambda_1}}{\tau_{\lambda_2}}\right)}{\ln\left(\frac{\lambda_1}{\lambda_2}\right)}$$

where τ represents the AOD at a specific wavelength λ. We prioritized the use of the 500 nm and 675 nm pair for calculating α due to their proximity to 532 nm. In cases where data at 675 nm were unavailable, the 870 nm or 440 nm channels were used as secondary references. This processing ensures spectral consistency between the ground-based validation dataset and the model outputs.

S3. Input Variable

Table S1. Summary of input variables from MERRA-2 reanalysis and GEOS-Chem model simulations used in this study, categorized by data source and physical property.

Category	Variable Name	Physical Description
MERRA-2 (3D Fields)	T	Air Temperature (3D)
	U, V	Eastward & Northward Wind Components
	OMEGA	Vertical Pressure Velocity
	QV	Specific Humidity
	RH	Relative Humidity
	CLOUD	Cloud Fraction
	OPTDEPTH	In-cloud Optical Thickness
	QI, QL	Mass Fraction of Cloud Ice / Liquid Water
	TAUCLI, TAUCLW	Optical Thickness (Ice / Liquid Clouds)
	DTRAIN	Detrainment Mass Flux
	CMFMC	Cumulative Mass Flux
	PFICU, PFILSAN	Ice Precipitation Flux (Conv / LS)
	PFLCU, PFLLSAN	Liquid Precipitation Flux (Conv / LS)
	DQRCU, DQRLSAN	Rainwater Source (Conv / LS)
	REEVAPCN, REEVAPLS	Evaporation of Precip (Conv / LS)
	PV	Ertel's Potential Vorticity
MERRA-2 (Surface/2D)	PS, SLP	Surface Pressure / Sea Level Pressure
	TS, T2M, T10M	Skin Temp / 2m Temp / 10m Temp
	U10M, V10M	10-meter Wind Components
	QV2M / Q850	Specific Humidity (2m / 850hPa)

	PBLH	Planetary Boundary Layer Height
	PRECTOT	Total Precipitation
	PRECCON, PRECLSC	Precipitation (Convective / Large Scale)
	PRECANV, PRECSNO	Precipitation (Anvil / Snow)
	SNODP / SNOMAS	Snow Depth / Snow Mass
	ALBEDO	Surface Albedo
	CLDTOT	Total Cloud Area Fraction
	SWGDN	Incident Shortwave Flux
	LWGNT, LWTUP	Net Downward / Upward Longwave Flux
	EFLUX, HFLUX	Latent / Sensible Heat Flux
	EVAP	Surface Evaporation
	GWETROOT, GWETTOP	Soil Wetness (Root / Top)
	LAI, GRN	Leaf Area Index / Greenness
	FRSNO, FRSEAICE	Fraction of Snow / Sea Ice
	SEAICE00-90	Sea Ice Fraction (Binned 00-90)
	TO3	Total Column Ozone
	TROPPT	Tropopause Pressure
	USTAR, Z0M	Friction Velocity / Roughness Length
	LWI	Land Water Indicator
	PARDF, PARDR	PAR (Diffuse / Direct)
GEOS-Chem (Aerosol Mass)	AerMassSO_4	Sulfate Aerosol Mass
	AerMassBC, AerMassPOA	Black Carbon / Primary Organic Aerosol
	AerMassOPOA	Oxidized Primary Organic Aerosol
	AerMassNIT, AerMassNH_4	Nitrate / Ammonium Aerosol Mass

	AerMassSAL	Sea Salt Aerosol Mass
	AerMassSOA*	Secondary Organic Aerosol
	AerMassHMS	Hydroxymethanesulfonate Aerosol
	AerMassLVOCOA	Low Volatility Oxygenated OA
	TotalOA	Total Organic Aerosol
	PM_{25}, PM_{10}	$PM_{2.5}$ / PM_{10} Mass
	EC_gc	Elemental Carbon Tracer
GEOS-Chem (Optics/Micro)	AODHyg532nm_*	Hygroscopic AOD at 532nm
	AODDust	Dust Optical Depth
	AerHygroscopicGrowth_*	Hygroscopic Growth Factors
	AerSurfAreaHyg_*	Hygroscopic Aerosol Surface Area
	Chem_WetAeroRadi*	Wet Aerosol Radius
	Chem_AeroRadi*	Dry Aerosol Radius
	Chem_WetAeroArea*	Wet Aerosol Surface Area
	Chem_AeroArea*	Dry Aerosol Surface Area
GEOS-Chem (Gas Species)	SpeciesConc_SO_2	Sulfur Dioxide
	SpeciesConc_NO, NO_2	Nitrogen Oxides
	SpeciesConc_O_3	Ozone
	SpeciesConc_NH_3	Ammonia
	SpeciesConc_HNO_3	Nitric Acid
	SpeciesConc_CO	Carbon Monoxide
	SpeciesConc_OH	Hydroxyl Radical
	SpeciesConc_HO_2, H2O2	Hydroperoxyl / Hydrogen Peroxide
	SpeciesConc_CH_2O	Formaldehyde

SpeciesConc_VOCs	VOCs (Isoprene, MVK, MACR, Aromatics...)
SpeciesConc_S-Map	Sulfur Species (DMS, MSA, HMS)

58

S4. Detailed Architecture of the Transformer Components

a. Heterogeneous Input Embedding Strategies

Unlike the standard Transformer which uses a uniform positional encoding, we adopt distinct embedding strategies tailored to the physical nature of each input variable:

① **Hybrid Vertical Height Encoding**: To capture the stratification of the atmosphere, we combine a learnable discrete embedding with a continuous linear projection. For a vertical layer with index l and geopotential height value h_l:

$$e_{height}^{(l)} = Linear\left(Concat\left(E_{idx}[l], Linear(h_l)\right)\right) \quad (S1)$$

where E_{idx} is a learnable lookup table for layer indices.

② **Cyclic Spatiotemporal Encoding**: For variables with intrinsic periodicity (i.e., Month, Latitude, Longitude), we utilize trigonometric cyclic encoding to preserve their continuity (e.g., ensuring December is numerically close to January). For a variable v with a period T (e.g., T=12 for months, T=360 for longitude), the encoding is defined as:

$$e_{cyclic} = Linear\left(\left[\sin\left(\frac{2\pi v}{T}\right), \cos\left(\frac{2\pi v}{T}\right)\right]\right) \quad (S2)$$

③ **Categorical Embedding**: Binary variables (e.g., Day/Night flag $d \in \{0,1\}$) are mapped to dense vectors using standard learnable embeddings:

$$e_{dn} = E_{dn}[d] \quad (S3)$$

b. ~~Global~~ Variable Identity Embedding

For the global context inputs $X_{global} \in \mathbb{R}^{N_{var}}$, where each scalar x_j represents a distinct physical variable (e.g., PBLH, Surface Pressure), we use a specialized projection:

$$e_{global}^{(j)} = LayerNorm\left(x_j \cdot \omega_j + b_j + id_j\right) \quad (S4)$$

where $\omega_j \in \mathbb{R}^{d_{model}}$ is a variable-specific projection vector (broadcasted multiplication), b_j is a bias term, and id_j is a learnable identity embedding unique to the j-th variable type. This ensures the model distinguishes between variables even if their scalar values are similar.

c. Standard Multi-Head Self-Attention (MSA)

The Transformer encoder utilizes MSA to capture dependencies between different vertical layers. For a given input sequence X, the attention output is calculated as:

$$Attention(Q,K,V) = Softmax\left(\frac{QK^T}{\sqrt{d_k}}\right)V \quad (S5)$$

where $Q = XW^Q$, $K = XW^K$, and $V = XW^V$ are the query, key, and value matrices obtained through linear transformations. In our multi-head setting, the outputs are concatenated and linearly projected:

$$MSA(Q,K,V) = Concat(head_1, \dots, head_h)\, W^O \quad (S6)$$

d. Position-wise Feed-Forward Network (FFN)

Each encoder layer includes a fully connected FFN with a GELU activation function:

$$FFN(x) = Linear_2\left(GELU\left(Linear_1(x)\right)\right) \quad (S7)$$

e. Gated Feature Fusion

$$E_{local}^{(z)} = \sum_{k=1}^{4} \alpha_k^{(z)} \cdot Norm\left(h_k^{(z)}\right) \; s.t. \; \sum \alpha_k = 1 \quad (S8)$$

where $h_k^{(z)}$ represents the embedding of the k-th feature group. The attention weights $\alpha_k^{(z)}$ are generated by a learnable gating network, allowing the model to autonomously identify and prioritize the most physically relevant information source for each specific altitude layer.

f. Output Layer

$$\Delta_{AEC}^{pred} = MLP\left(H_{cross} + H_{phyche}\right) \cdot s + b \quad (S9)$$

Where Δ_{AEC}^{pred} denotes the predicted systematic bias of the AEC. The parameters s and b are learnable scaling and bias terms, respectively, introduced to adaptively map the normalized network outputs to the physical magnitude of extinction biases.

g. Magnitude-Weighted Loss

Aerosol extinction exhibits a high dynamic range and severe spatial heterogeneity, statistically dominated by near-zero background values (e.g., in the clean free

设置了格式：字体：加粗
设置了格式：字体：加粗
设置了格式：字体：加粗
设置了格式：字体：加粗
设置了格式：字体：非加粗

troposphere). Standard Mean Squared Error (MSE) treats all data points equally, which often causes the model to over-fit these overwhelming background signals while under-correcting the large systematic biases associated with severe pollution episodes. To resolve this imbalance, we propose a Magnitude-Weighted Loss (L_{MW}).

$$L_{MW} = \frac{1}{N}\sum_{i=1}^{N}\left(\Delta_{AEC}^{pred} - \Delta_{AEC}^{target}\right)^2 \cdot \omega\left(\Delta_{AEC}^{target}\right) \quad (S10)$$

$$\omega\left(\Delta_{AEC}^{target}\right) = \left|\Delta_{AEC}^{target}\right|^p + \lambda \cdot \mathrm{e}^{-\beta\left|\Delta_{AEC}^{target}\right|} + \epsilon \quad (S11)$$

Here, the weight function ω dynamically rescales the optimization penalty based on the magnitude of the true bias (Δ_{AEC}^{target}), utilizing three empirically derived components. (1) Large-Error Prioritization ($\left|\Delta_{AEC}^{target}\right|^p$): Governed by the exponent p, this term sharply amplifies the gradient for samples with massive simulation biases. It forces the network to target critical GEOS-Chem failures, such as significantly underestimated dust storms or heavy anthropogenic haze, rather than safely fitting the background average. (2) False Alarm Penalty ($\lambda \cdot \mathrm{e}^{-\beta\left|\Delta_{AEC}^{target}\right|}$): Regulated by constants λ and β, this exponential decay applies a strict penalty when the true GEOS-Chem bias is negligible but the model attempts a non-zero correction. Physically, this prevents the generation of spurious aerosol artifacts in regions where the GEOS-Chem is already accurate, such as the clean free troposphere. (3) Base Stability Term (ϵ): A minor constant added to maintain numerical stability during gradient descent.

设置了格式：字体：非加粗

S5. 5-fold Cross-Validation

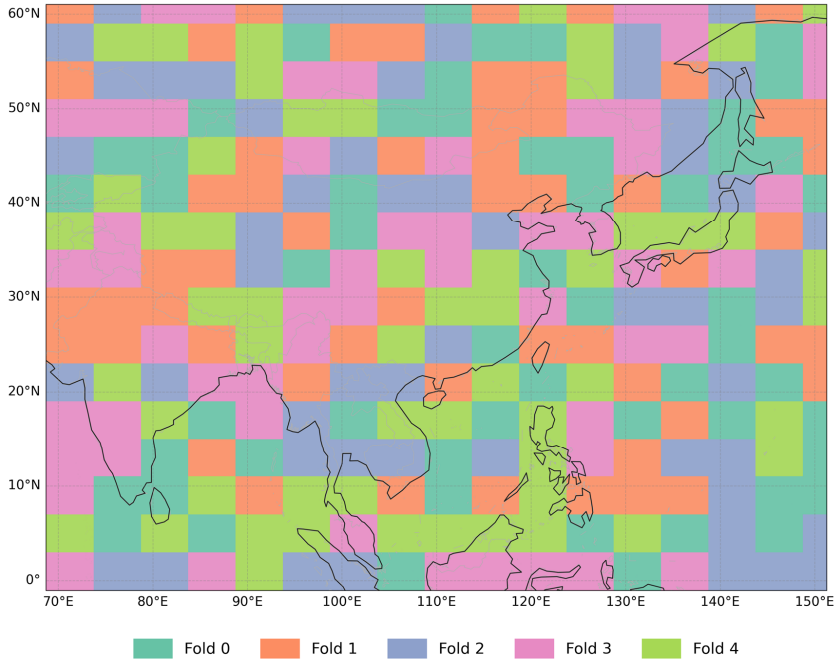

Figure S1. The illustration of the data splitting for the cross-validation. The color-coded checkerboard pattern represents the spatial partitioning of data into five folds used for model evaluation. Specifically, the geographical domain is divided into grid blocks, which are then randomly assigned to one of the five folds.

S6. Statistical Evaluation Metrics

To quantify the model performance in reconstructing AEPs, the following statistical metrics are employed. Let $\Delta_{AEC}^{target}{}_{i}$ and $\Delta_{AEC}^{pred}{}_{i}$ denote the observed (CALIOP) and predicted (Model) AEC for the i-th sample, respectively, and N be the total number of samples.

a. Pearson Correlation Coefficient (R)

Reflects the linear consistency between predictions and observations:

$$R = \frac{\sum_{i=1}^{N}\left(\Delta_{AEC}^{target}{}_{i} - \overline{\Delta_{AEC}^{target}}\right)\left(\Delta_{AEC}^{pred}{}_{i} - \overline{\Delta_{AEC}^{pred}}\right)}{\sqrt{\sum_{i=1}^{N}\left(\Delta_{AEC}^{target}{}_{i} - \overline{\Delta_{AEC}^{target}}\right)^{2}}\sqrt{\sum_{i=1}^{N}\left(\Delta_{AEC}^{pred}{}_{i} - \overline{\Delta_{AEC}^{pred}}\right)^{2}}} \quad (S12\text{~~8~~})$$

where $\overline{\Delta_{AEC}^{target}}$ and $\overline{\Delta_{AEC}^{pred}}$ are the means of observed and predicted values.

b. Error Magnitude Metrics

① Mean Absolute Error (MAE): Represents the average magnitude of errors.

$$MAE = \frac{1}{N}\sum_{i=1}^{N}\left|\Delta_{AEC}^{target}{}_{i} - \Delta_{AEC}^{pred}{}_{i}\right| \quad (S13\text{~~9~~})$$

② Root Mean Square Error (RMSE): Sensitive to large errors and outliers.

$$RMSE = \sqrt{\frac{1}{N}\sum_{i=1}^{N}(\Delta_{AEC}^{target}{}_{i} - \Delta_{AEC}^{pred}{}_{i})^{2}} \quad (S14\text{~~0~~})$$

c. Normalized Root Mean Square Error (NRMSE)

To compare performance across vertical layers with varying orders of magnitude in extinction coefficients, we normalize the RMSE by the range of the observed data:

$$NRMSE = \frac{RMSE}{\Delta_{AEC}^{target}{}_{max} - \Delta_{AEC}^{target}{}_{min}} \quad (S15\text{~~1~~})$$

where $\Delta_{AEC}^{target}{}_{max}$ and $\Delta_{AEC}^{target}{}_{min}$ are the maximum and minimum observed extinction coefficients in the target dataset, respectively.

d. Mean Bias (Bias)

Used to diagnose systematic overestimation ($Bias > 0$) or underestimation ($Bias < 0$):

$$Bias = \frac{1}{N}\sum_{i=1}^{N}\left(\Delta_{AEC\ i}^{pred} - \Delta_{AEC\ i}^{target}\right) \quad (S162)$$

S7. Mathematical Formulation of Interpretability Methods

To quantify the contribution of different input features to the bias correction, we employ ensemble-based interpretability methods. The mathematical definitions for the Gradient-based Attribution, Attention Mechanism, and Permutation Feature Importance are detailed below.

a. Gradient-based Feature Attribution (Input × Gradient)

For the vertical profile inputs, we utilize the Input × Gradient method to quantify the sensitivity of the model output to local feature variations. The importance score (I_{feet}) for a specific feature at a specific vertical layer is calculated as the ensemble average of the absolute gradients weighted by the input magnitude:

$$I_{feet} = \frac{1}{M}\sum_{m=1}^{M}\left(\frac{1}{N}\sum_{n=1}^{N}\left|x_{feat}^{(n)} \odot \frac{\partial \mathcal{F}_m\left(x^{(n)}\right)}{\partial x_{feat}^{(n)}}\right|\right) \quad (S173)$$

where: N is the total number of samples in the validation set. M is the number of cross-validation folds (here $M = 5$). $x_{feat}^{(n)}$ denotes the input value of a specific feature for the n-th sample. $\partial\mathcal{F}_m(\cdot)$ represents the model prediction function for the m-th fold. $\odot$ denotes element-wise multiplication.

b. Global Attention Mechanism

Global Attention Mechanism For global meteorological covariates (i.e., 2D single-layer variables from MERRA-2), we analyze the Cross-Attention weights extracted from the Transformer decoder. The global average attention score ($\bar{A}_{ij}$) represents the interaction strength between the i-th vertical layer of the profile and the j-th global variable (e.g., PBLH, Surface Pressure). It is computed by averaging across all attention heads and all samples:

$$\bar{A}_{ij} = \frac{1}{N}\sum_{n=1}^{N}\frac{1}{H}\sum_{h=1}^{H}A_{ij}^{(n,h)} \quad (S184)$$

where: H is the number of attention heads. N is the total number of samples in the dataset. $A_{ij}^{(n,h)}$ is the attention weight matrix from the h-th head for the n-th sample. The inner summation averages the contributions from multi-head attention mechanisms,

while the outer summation computes the dataset-wide average contribution of each global variable, filtering out sample-specific noise.

c. Gated Fusion Weights

The model dynamically fuses information from different sources using learnable scalar weights. The effective contribution weight (W_c) for a specific component c at altitude z is formalized as:

$$W_c(z) = \sigma\left(\frac{1}{N}\sum_{n=1}^{N}\omega_c^{(n)}(z)\right) \quad (S195)$$

where $\omega_c^{(n)}(z)$ is the raw gate value predicted by the model for sample n at altitude z, and $\sigma(\cdot)$ represents the normalization function (e.g., Softmax) ensuring the weights sum to 1.

d. Permutation Feature Importance

To assess the model's reliance on specific feature groups (e.g., Profile Features vs. Global Variables), we calculate the percentage increase in ~~Mean Squared Error (~~MSE~~)~~ when a feature group is randomly permuted. The importance score (S_k) for feature group k is defined as:

$$S_k = \frac{\mathcal{L}_{perm,k} - \mathcal{L}_{base}}{\mathcal{L}_{base}} \times 100\% \quad (S2016)$$

$$\mathcal{L}_{base} = \frac{1}{N}\sum_{n=1}^{N}\left(y^{(n)} - \hat{y}^{(n)}\right)^2 \quad (S2117)$$

where: $\mathcal{L}_{base}$ is the baseline MSE on the original validation set. $\mathcal{L}_{perm,k}$ is the MSE calculated after randomly shuffling the feature group k along the batch dimension while keeping other features fixed.

S8. Implementation of SHAP Analysis

To efficiently compute SHAP values for the deep neural network while maintaining statistical representativeness, we adopt a clustering-based sampling strategy for the background dataset:

a. Representative Background Selection

Instead of using a random subset or the zero-mean baseline (which is physically unrealistic for atmospheric variables), we apply K-means clustering on the normalized training dataset. We set the number of clusters k=100 and selected the medoids (samples closest to the cluster centers) to form a background dataset. This ensures that the reference baseline covers the full manifold of atmospheric states, from clean background days to severe pollution episodes.

b. Target Sample Selection

For regional analysis, we select top-50 samples with the highest model corrections (i.e., large initial GEOS-Chem biases that were successfully corrected by the model) within each region of interest. This "Case Study Strategy" ensures that the SHAP explanation focuses on the most significant bias correction events rather than trivial noise.

S9. Supplementary Evaluation of the Overall Model

Table S2. Summary of model performance for AEC simulation biases (Δ_{AEC}) on the validation subsets derived from the 5-fold spatial cross-validation strategy during the training phase.

Experiment ID	R (Val)	MAE (Val)	RMSE (Val)
Exp-2017	0.629	0.015	0.042
Exp-2018	0.652	0.015	0.041
Exp-2019	0.609	0.015	0.042
Average	0.630	0.015	0.042

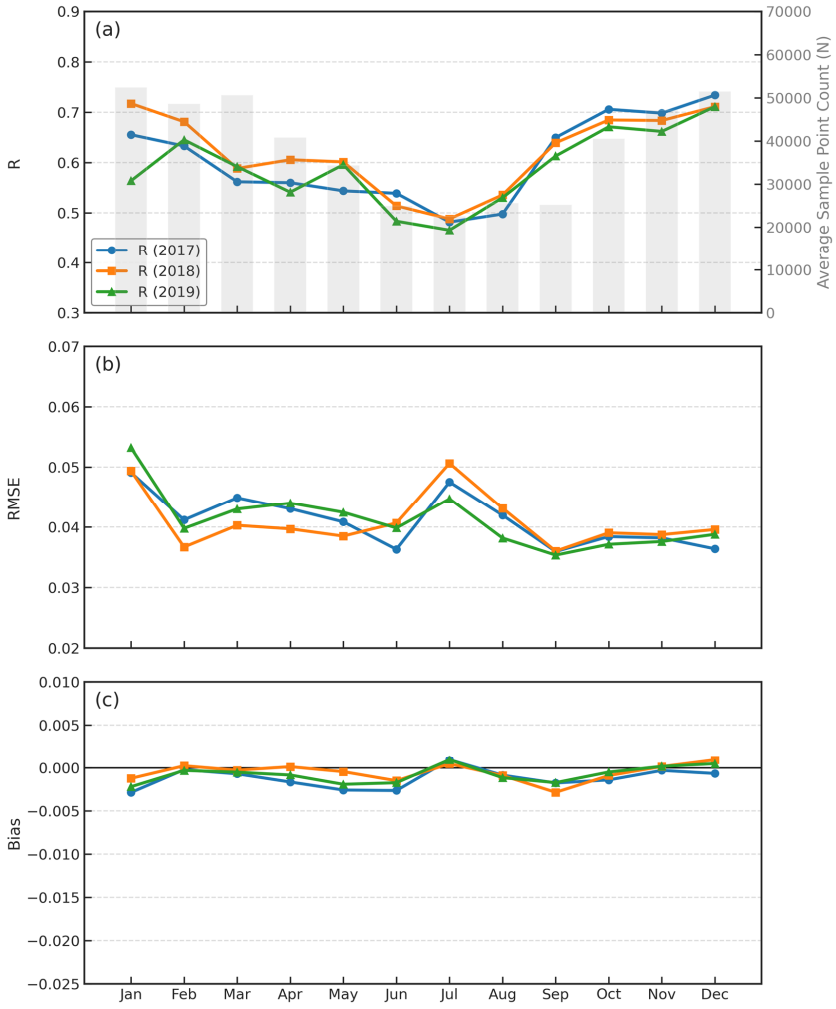

Figure S2. Monthly variations of the statistical evaluation metrics (derived from the 5-fold cross-validation validation subsets) for assessing the physics-informed Transformer model's performance in predicting the AEC simulation bias (Δ_{AEC}). The panels display the time series of R (a) with the multi-year average monthly sample size (N, gray bars), RMSE (b), and mean bias (c).

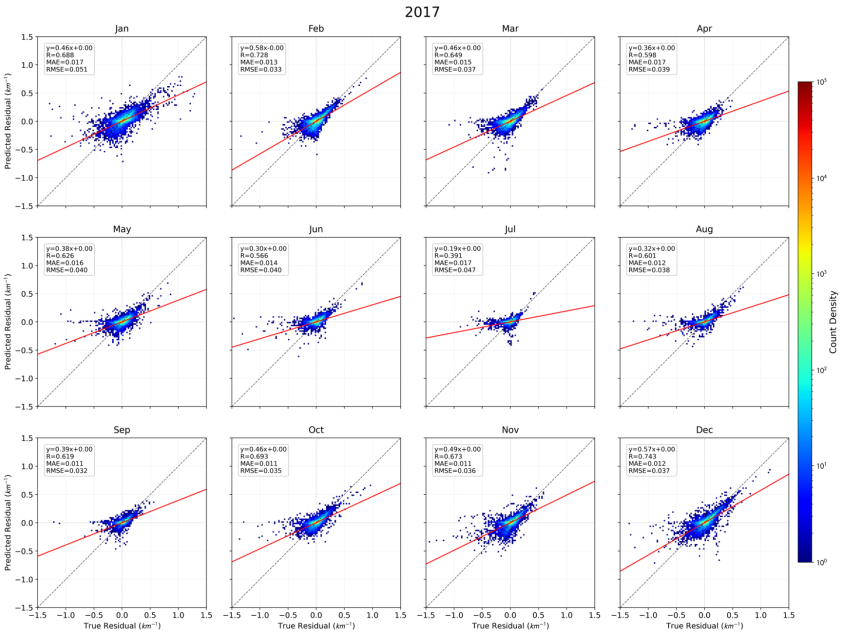

Figure S3. Monthly density scatter plots comparing the predicted AEC simulation bias (y-axis) generated by the physics-informed Transformer against the true residuals (x-axis) for the year 2017. The true residual is defined as the difference between the original GEOS-Chem simulation AEC and CALIOP observation AEC (GEOS-Chem – CALIOP).

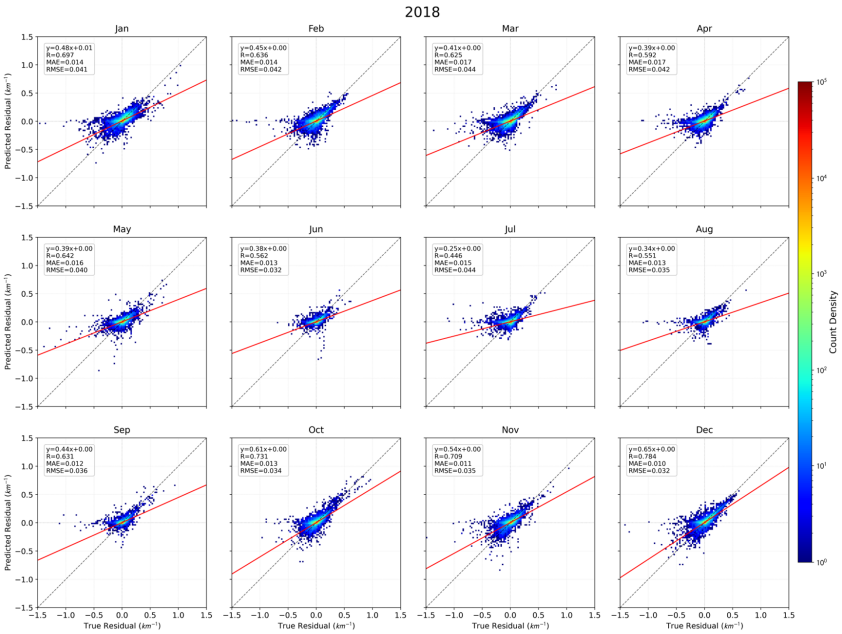

Figure S4. Monthly density scatter plots comparing the predicted AEC simulation bias (y-axis) generated by the physics-informed Transformer against the true residuals (x-axis) for the year 2018.

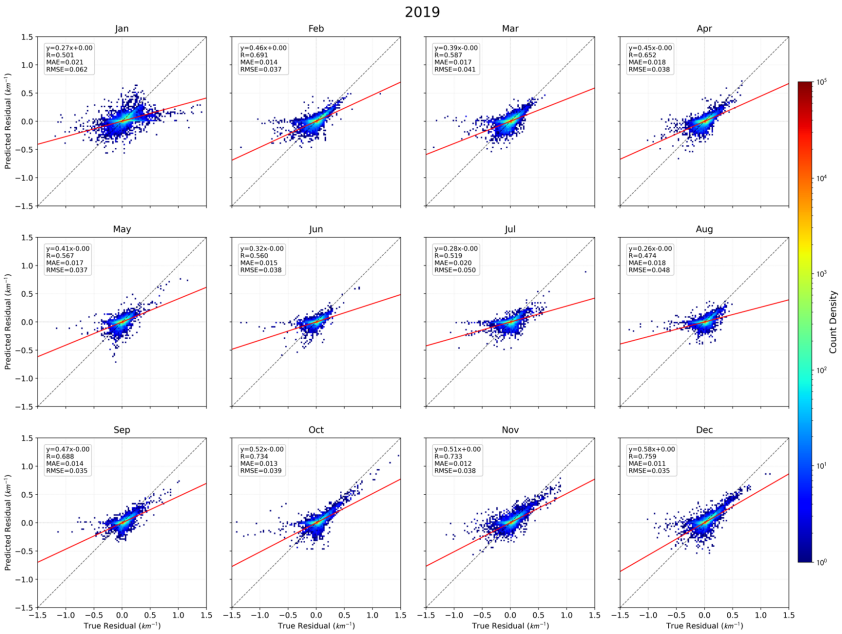

Figure S5. Monthly density scatter plots comparing the predicted AEC simulation bias (y-axis) generated by the physics-informed Transformer against the true residuals (x-axis) for the year 2019.

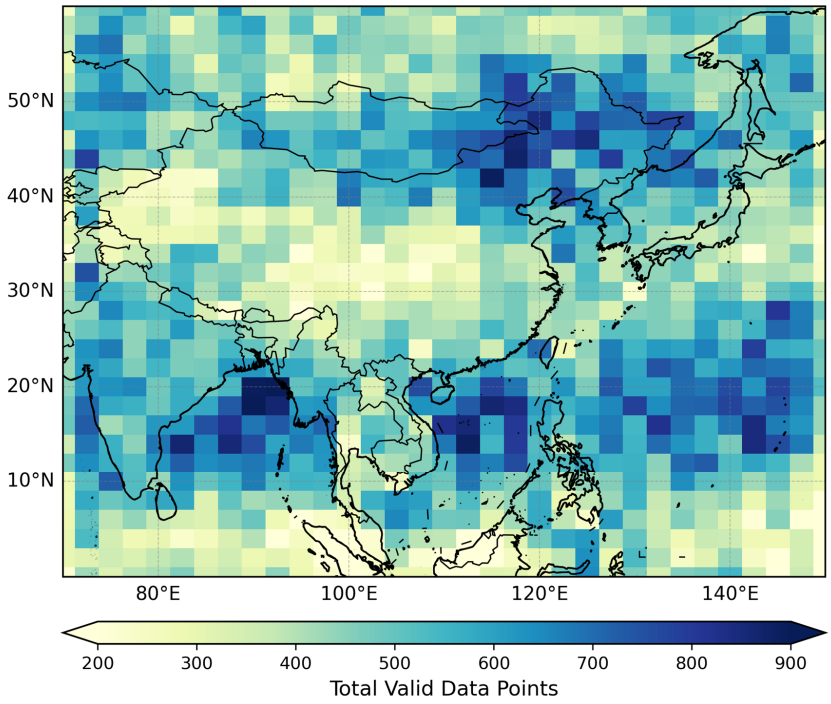

Figure S6. Spatial distribution of valid CALIOP data points aggregated for the test year 2019.

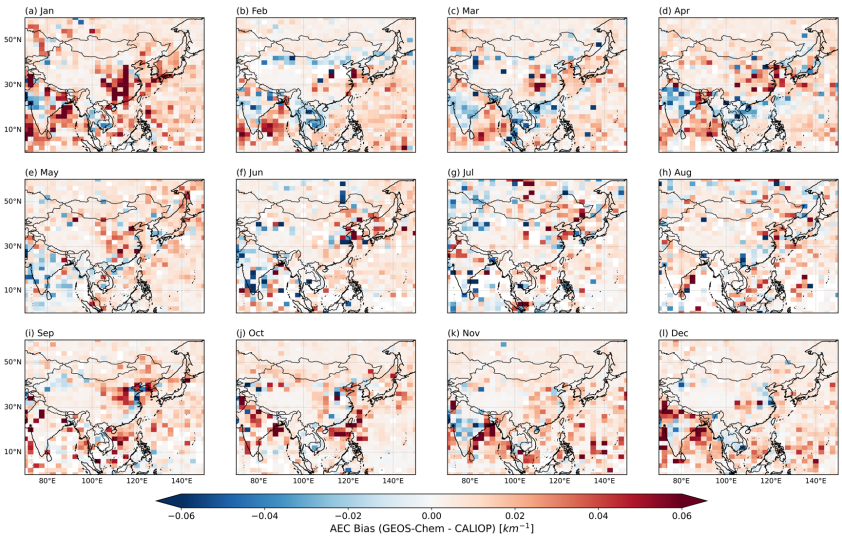

250

251 Figure S7. Monthly spatial evolution of the Target AEC simulation bias (Δ_{AEC}) for the

252 test year 2019.

S10. Analysis of Residual Outliers

This section analyzes the samples where the absolute residuals between the model-corrected AEC and CALIOP observations exceed 0.15 km^{-1} (i.e., points falling outside the error envelope in Fig. 6). The diagnostic results presented in Figure S8 demonstrate that these outliers are not randomly distributed but exhibit specific spatial and vertical characteristics.

Spatially (Fig. S8a), regions with elevated outlier occurrence are predominantly anchored over major emission source regions, including the IGP, the NCP, and the Indochina Peninsula. Vertically (Fig. S8b), over 80% of these extreme deviations are confined within the PBL (below 1.5 km AGL), an altitude range characterized by the heaviest local aerosol loading and the most intense turbulent mixing.

These distribution patterns confirm that the dispersion observed in the scatter plots fundamentally originates from representativeness errors. In complex source regions, the high-resolution footprint of CALIOP resolves transient, highly concentrated sub-grid plumes. The fine-scale physical structures of these plumes are inherently smoothed out during the spatial averaging onto the coarse 2°×2.5° grid of the GEOS-Chem model. We attribute the remaining 1.20% of outlier samples primarily to the spatial heterogeneity of aerosols that lies below the resolvable scale of the model grid.

带格式的：缩进：首行缩进： 2 字符

设置了格式：字体：非加粗

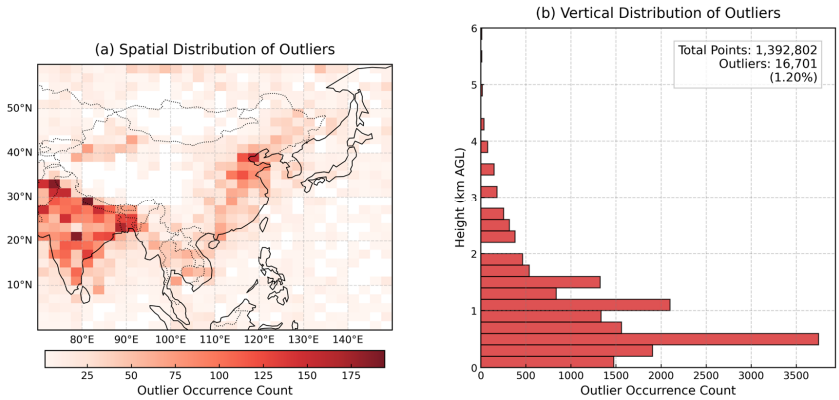

Figure S8. Spatial and vertical distributions of the residual outliers for the combined test years (2017–2019). Outliers are strictly defined as samples where the absolute

residual between the GC-TF prediction and CALIOP observation exceeds ±0.15 km^{-1}. The panels display (a) the spatial occurrence count of these outliers mapped onto the native 2°×2.5° GEOS-Chem grid, and (b) their vertical distribution as a function of height AGL. The statistical box indicates that these extreme deviations account for merely 1.20% of the total valid dataset.

设置了格式：非上标/ 下标

S1~~0~~. Supporting Information for Improvement Evaluation of GEOS-Chem Simulations

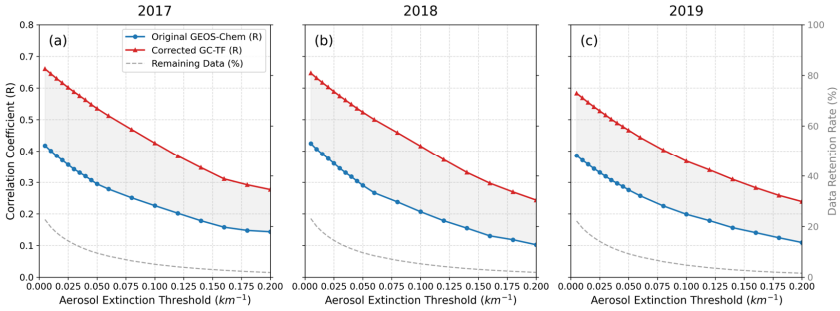

Figure S~~9~~8. Sensitivity of model predictive performance to AEC thresholds across three independent test years (2017–2019). The gray dashed line (corresponding to the right axis) indicates the data retention rate, representing the percentage of valid samples remaining after filtering out clean background signals below the threshold

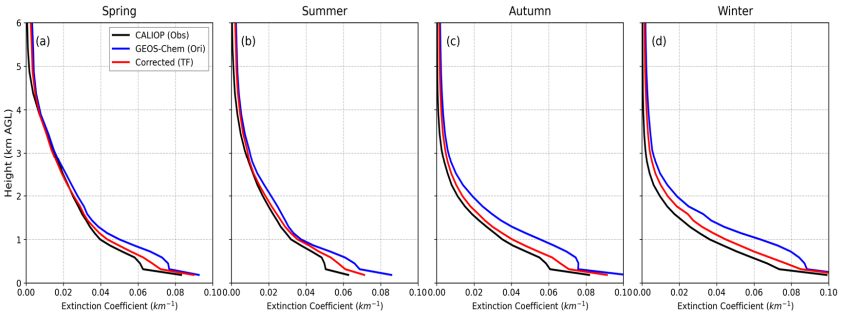

Figure S10~~9~~. Seasonal mean vertical profiles of AEC (km^{-1}) averaged over the three test years (2017–2019). The panels display the profiles for Spring (MAM, a), Summer (JJA, b), Autumn (SON, c), and Winter (DJF, d). The black lines represent the CALIOP observations, the blue dashed lines denote the original GEOS-Chem simulations, and the red lines show the results corrected by the GC-TF model. The profiles are vertically resolved from the surface to 6 km above ground level (AGL).

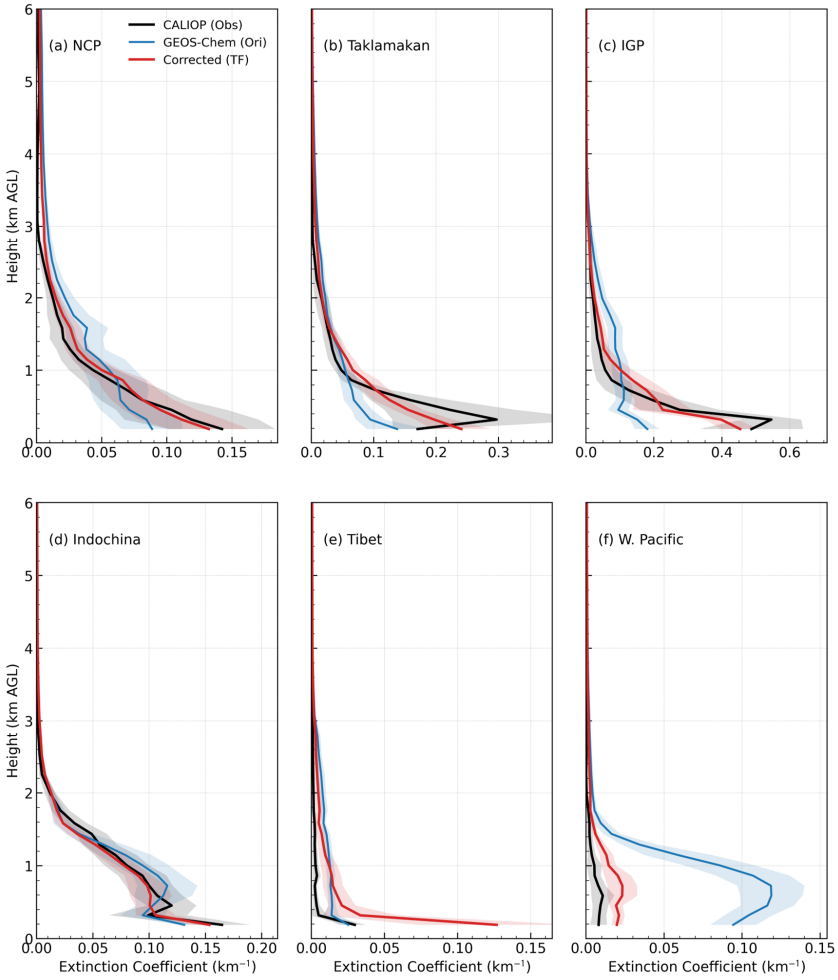

Figure S11~~0~~. Regional annual mean vertical profiles of AEC over six representative sub-regions for the test year 2017. The panels display the profiles for NCP (a), Taklamakan Desert (b), IGP (c), Indochina (d), Tibetan Plateau (e), and Western Pacific (f). The black lines represent CALIOP observations, the blue dashed lines denote the original GEOS-Chem simulations, and the red lines show the results corrected by the GC-TF model. The shaded areas indicate the regional standard deviation ($\pm 0.5\sigma$), representing the spatial variability within each sub-region.

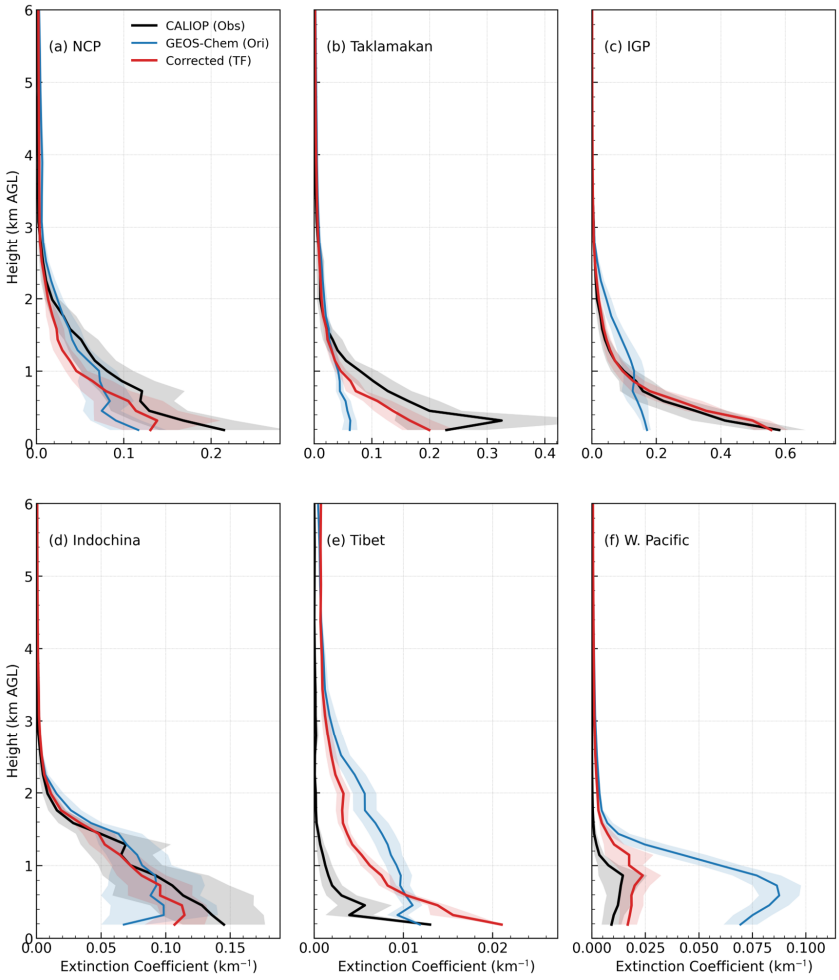

Figure S12~~1~~. Regional annual mean vertical profiles of AEC over six representative sub-regions for the test year 2018.

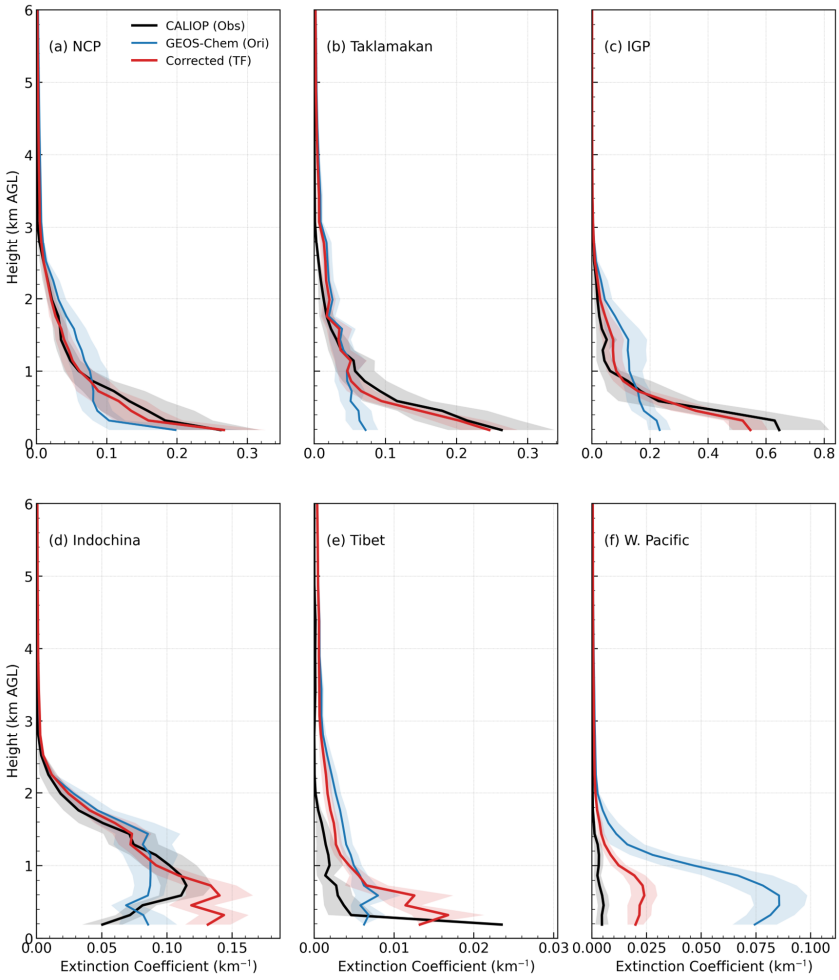

Figure S1~~3~~2. Regional annual mean vertical profiles of AEC over six representative sub-regions for the test year 2019.

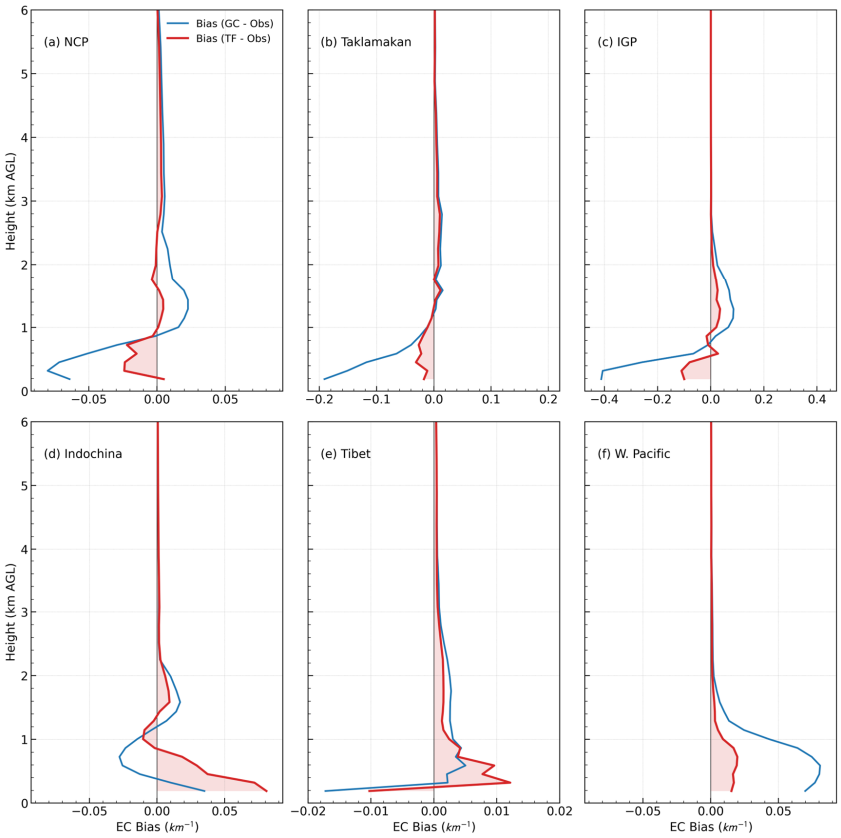

Figure S1~~3~~. Vertical profiles of the annual mean AEC simulation bias over six representative sub-regions for the test year 2019. The panels display the bias profiles for NCP (a), Taklamakan Desert (b), IGP (c), Indochina (d), Tibetan Plateau (e), and Western Pacific (f). The AEC bias is calculated as Model minus Observation. The blue lines represent the original GEOS-Chem bias (GEOS-Chem−CALIOP), while the red lines denote the remaining bias after GC-TF correction (GC-TF − CALIOP). The vertical black line indicates the zero-bias reference, and the shaded red areas highlight the magnitude of the residual bias after correction.

S12~~1~~. Supporting Information for Interpretability Analysis

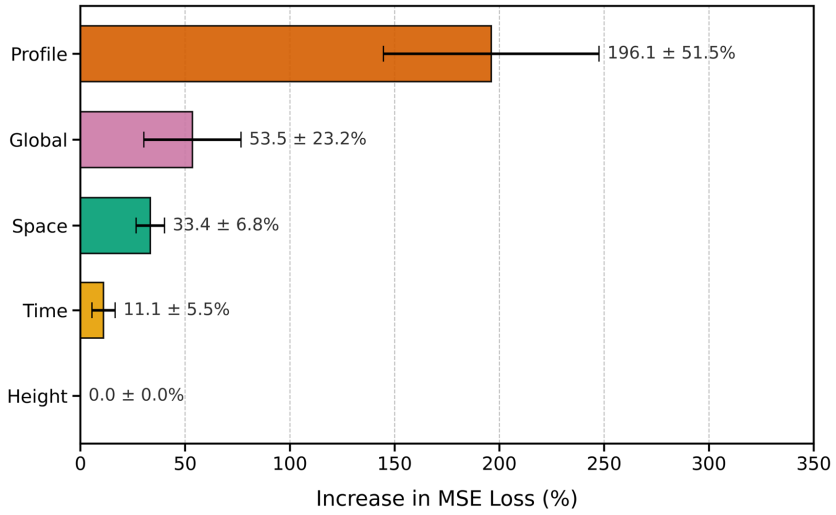

Figure S15~~4~~. Permutation feature importance analysis evaluated on the test dataset. The importance of each feature group is quantified by the relative increase in MSE loss when the values of that feature group are randomly shuffled, while keeping others unchanged. The error bars represent the standard deviation across the 5-fold cross-validation. Note that Profile Features are identified as the most critical input, causing a ~200% surge in error if disrupted, confirming the model's heavy reliance on physical state variables for magnitude prediction.

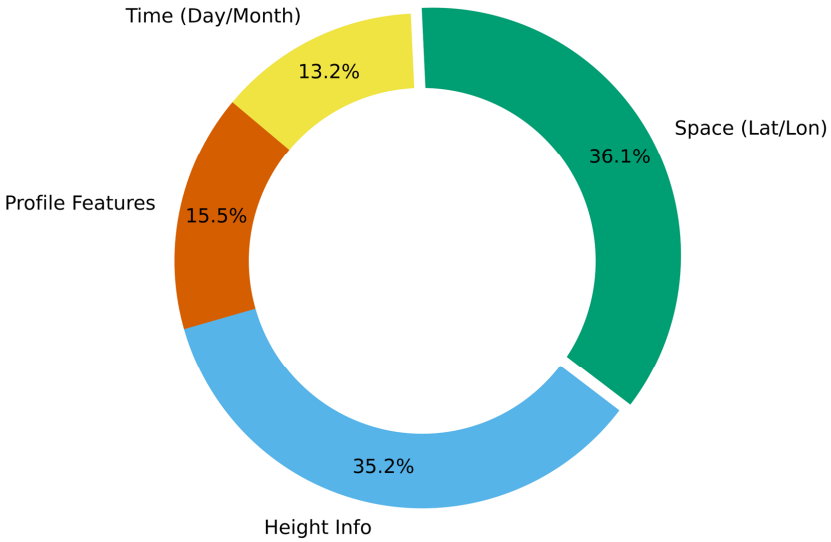

Figure S1~~5~~6. Global average relative importance of the input features learned by the physics-informed model for the test year 2019. The pie chart displays the percentage contribution of four feature groups: Space (36.1%), Height Info (35.2%), Profile Features (15.5%, including GEOS-Chem chemical concentrations and MERRA2 meteorology), and Time (13.2%). The dominance of spatial and height information reflects the strong spatial heterogeneity and vertical stratification of aerosol distributions.

S13. Sensitivity Analysis of CALIOP Observational Uncertainties

To quantitatively evaluate the model's sensitivity to the inherent systematic uncertainties of CALIOP observations, we design a perturbation experiment based on the 2017 independent test set. Considering the reported mean relative bias of CALIOP AOD against AERONET is approximately -5.1%±8.5%, we artificially apply a constant ±5% multiplier to the CALIOP AEC targets during the training phase. This creates two extreme scenarios: one simulating a severe systematic underestimation (-5% bias) and another simulating a systematic overestimation (+5% bias). The physics-informed Transformer is then retrained from scratch for both scenarios, and the newly predicted residual profiles are added back to the original GEOS-Chem simulations to obtain the final perturbed corrected AEC profiles.

As presented in Table S3, the GC-TF model exhibits strong resistance to target perturbations. Even with a 5% systematic error injected into the learning target, the model's RMSE and Mean Bias remain highly stable and significantly superior to the original GEOS-Chem baseline. Visually, Figure S17 illustrates that the perturbed predictions (dashed and dotted lines) tightly hug the unperturbed baseline correction (solid red line), forming a narrow perturbation range (red shaded area) that aligns well with the CALIOP observations. This demonstrates that the data-driven correction framework captures robust physical mappings rather than merely overfitting to observational noise.

带格式的：缩进：首行缩进： 0 字符

带格式的：缩进：首行缩进： 0 字符

Table S3. Quantitative evaluation of the GC-TF model's sensitivity to CALIOP observational uncertainties on the 2017 independent test set. The metrics are derived by validating both the original GEOS-Chem simulations and the corrected GC-TF results against the unperturbed CALIOP AEC profiles.

Model/Scenario	RMSE	MAE	Mean Bias	R
Original GEOS-Chem	0.052	0.020	0.006	0.522
Baseline GC-TF (Unperturbed)	0.039	0.014	0.002	0.732
GC-TF (-5% CALIOP Bias)	0.040	0.014	0.001	0.716
GC-TF (+5% CALIOP Bias)	0.040	0.015	0.004	0.718

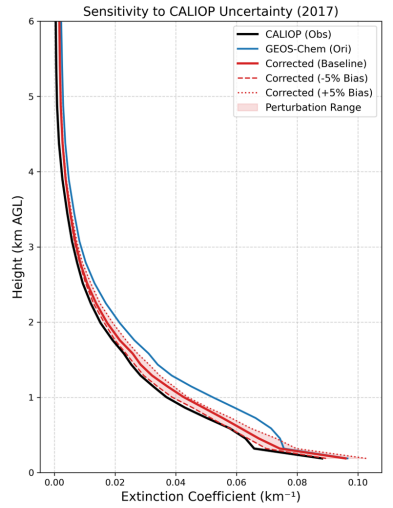

Figure S17. Vertical profiles illustrating the sensitivity of the corrected AEC to target perturbations for the test year 2017. The black solid line represents the CALIOP observations, and the blue solid line represents the original GEOS-Chem simulation. The red solid line indicates the baseline correction of the GC-TF model trained on unperturbed data. The dashed and dotted red lines represent the corrected profiles generated by models trained with -5% and +5% perturbed CALIOP targets, respectively. The light red shaded area denotes the envelope of variation (Perturbation Range) induced by these observational uncertainties.

带格式的：居中
格式化表格
带格式的：居中
带格式的：居中
带格式的：居中
带格式的：居中
带格式的：居中

S14. Stratified Evaluation by Aerosol Subtypes

To evaluate the model performance under distinct aerosol composition regimes, we utilize the Feature Classification Flags embedded in the CALIOP Level 2 Atmospheric Volume Description. The NA evaluation dataset (2018) is partitioned into two representative subsets: a dust-dominated regime (combining 'Dust' and 'Polluted Dust' subtypes) and an SOA-dominated continental regime (combining 'Clean Continental' and 'Polluted Continental/Smoke' subtypes).

Table S4. Statistical evaluation of GC-TF model performance over NA, stratified by dominant CALIOP aerosol subtypes (2018). For each subset, we calculate statistical metrics for both the original GEOS-Chem simulation and the GC-TF corrected predictions against CALIOP AOD observations.

Aerosol Regime	Model	R	RMSE	MAE	Slope
Dust-dominated (Dust and Polluted Dust)	Original	0.41	0.032	0.027	0.21
	Corrected	0.50	0.032	0.027	0.32
SOA-dominated (Clean and Polluted Continental)	Original	0.51	0.034	0.031	0.27
	Corrected	0.50	0.035	0.031	0.30

带格式的：缩进：首行缩进： 0 字符

带格式的：居中

格式化表格

带格式的：居中

带格式的：居中

S15. Methodological Benchmarking and Structural Necessity

To justify the architectural complexity of the proposed framework and isolate the sources of its performance gains, we conduct comprehensive benchmarking and ablation studies using the independent 2017 test dataset. To ensure a strictly fair comparison, all baseline models and ablation variants are trained using the identical set of input predictors—encompassing GEOS-Chem physicochemical states and MERRA-2 meteorological forcings—along with identical hyperparameter configurations and loss functions.

To establish a comprehensive baseline, two representative conventional deep learning architectures were evaluated. The first is a Multilayer Perceptron (MLP), representing point-wise neural networks. By treating vertical layers as independent vectors, the MLP tests whether a simple numerical mapping, devoid of sequential awareness, can resolve AEC biases. The second baseline is a 1-Dimensional Convolutional Neural Network (1D-CNN). This architecture utilizes localized receptive fields to capture vertical gradients between adjacent layers, serving as a benchmark for local structural extraction, contrasting with the global dependency modeling enabled by the Transformer.

Table S5. Performance benchmarking and ablation study of the proposed model against conventional machine learning architectures. Evaluation is conducted on the independent 2017 test dataset. All models are trained utilizing the identical meteorological and chemical state predictors to ensure a rigorous comparison.

Model Configuration	R	MAE (km^{-1})	RMSE (km^{-1})
MLP	0.083	0.019	0.052
1D-CNN	0.540	0.016	0.044
Without Gated Fusion	0.637	0.015	0.040
Without Cross-Attention	0.654	0.014	0.039
Physics-Informed Transformer (Full)	0.666	0.014	0.039

带格式的：缩进：首行缩进： 0 字符

设置了格式：字体颜色：自动设置